Acoustic Array Design

The design of a reconfigurable phased microphone array for aeroacoustic wind tunnel measurements

MSc Thesis

C.H.C. Vlemmix

Faculty of Aerospace Engineering
Department of Control and Operations
Section Aircraft Noise and Climate Effects

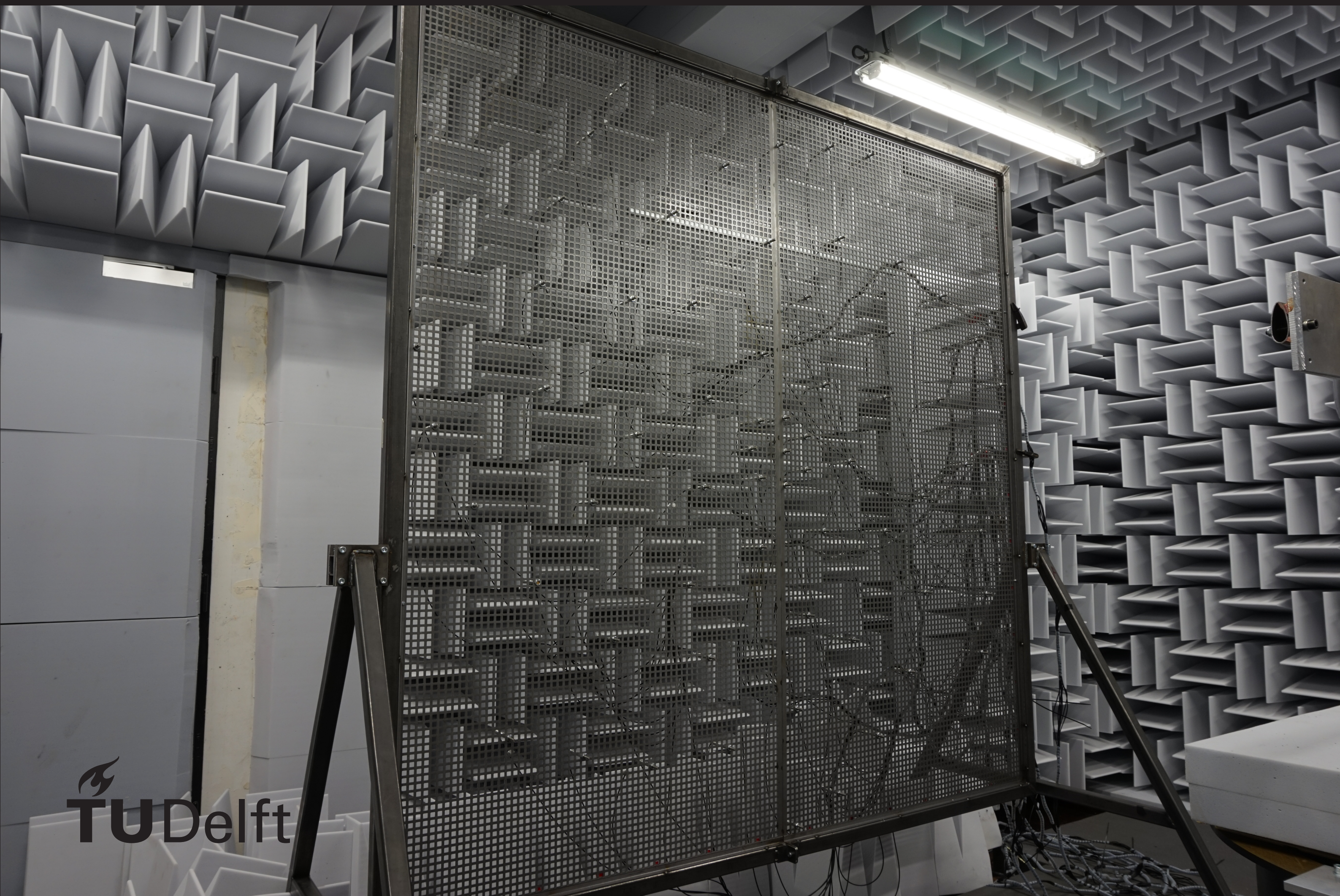

TUDelft

Acoustic Array Design

The design of a reconfigurable phased microphone array for aeroacoustic wind tunnel measurements

by

C.H.C. Vlemmix

to obtain the degree of Master of Science

at the Delft University of Technology,

to be defended publicly on December 5th, 2017 at 15:00.

Student number:	4157095	
Project duration:	November 28th, 2016 – December 5th, 2017	
Thesis committee:	Prof. dr. D. G. Simons,	TU Delft, department chairholder
	Dr. ir. M. Snellen,	TU Delft, thesis supervisor
	Ir. J. A. Melkert	TU Delft, FPP lecturer

TU Delft

Preface

As the keystone to obtaining my MSc degree at the Delft University of Technology, this thesis project has been an immensely valuable experience, contributing to my development as an engineer both professionally and personally.

First of all, I would like to thank the ANCE department chairholder, prof. dr. D. G. Simons, and my thesis supervisor, dr. ir. M. Snellen, for guiding me through this project with continuous feedback and suggestions for further analysis, motivating me to attain a deeper understanding of the subject matter. Daily supervisor ir. R. Merino-Martinez proved to be an immense help in answering my numerous questions, checking my work and progress, and a invaluable source of ideas and suggestions for alternative approaches.

This project would have been impossible without the anechoic facilities provided under the supervision of the AWEP department. As the main source of information on the tunnel, dr. ir. D. Ragni contributed immensely during the design phase, aiding in the procurement and construction of prototypes and making sure that I had all available information with which to design the initial concepts and final array structure. A big thanks to R. Van der List of DEMO, for analyzing the feasibility of the design and the subsequent manufacturing of the modular array. Practical arrangements for improving the array and implementing a functional network infrastructure were provided by on-site technical staff members ir. S. Bernardy and L. Molenwijk, greatly increasing the productivity in developing, testing and improving the array.

During this thesis project, the available facility and equipment was shared between multiple research projects. The thesis work by S. Luesutthiviboon, the research by ir. A. Rubio Carpio and the research by ir. A.M.N. Malgoezar and ir. A.E. Alves Vieira all made use of the acoustic array system at different stages of development. This provided me with direct user feedback on many different facets of the system, and for very different applications, allowing for the implementation of a multitude of improvements during development and resulting in a much more complete, higher-quality result.

It is impossible to list everybody involved with the project, and so I would like to express my gratitude to everyone who aided me in achieving this result. Finally, I want to thank my family for their love and support[1], motivating me to make the best of my student life, and my friends for their support and motivation throughout the past years, making my time here in Delft unforgettable.

C.H.C. Vlemmix
Delft, November 2017

[1]And, in specific cases (dad...), the promise to try not to interfere with the project too much

Abstract

The research objective for this thesis assignment is defined as follows:

To obtain a practical method of performing accurate acoustic measurements in the anechoic vertical wind tunnel at the Delft University of Technology by designing, creating, testing and evaluating a reconfigurable phased microphone array using state-of-the-art techniques and equipment.

The research objective clearly marks four distinct phases; design, creation, testing, and evaluation. These four phases were executed in that order. On this basis, an iterative array design process was initiated, where the requirements and restrictions to the array were identified and each new concept was an attempt to improve on the negative aspects of the previous.

The final result was a complete array system, capable of accurately recording acoustic data and transforming this to the required Matlab data format for post processing.

The anechoic test chamber was characterized according to the applicable ISO standards (ISO 3745[17] and ISO 3382[16]), followed by the calibration of the array. Due to the limitations of the calibrated sound source used for this purpose, the accuracy of the calibration can only be guaranteed within certain limits. Based on assumptions made pertaining to the directivity of the source, the final array was able to provide an estimation of the sound power level of the source within 1.5 dB of the calibrated value, which falls within the given ISO standard limits.

Furthermore, the performance of conventional beamforming as well as deconvolution methods CLEAN-PSF and CLEAN-SC was tested for a multitude of sound source distributions. Both deconvolution methods showed a large increase of accuracy in estimating both position and sound pressure level of the sound sources compared to conventional beamforming. Good performance of both deconvolution methods is an indicator of quality of the array in terms of ability to obtain accurate data as well as accurate knowledge of the microphone positions. For low signal-to-noise ratios, CLEAN-SC exhibited better performance than CLEAN-PSF, making it the preferred data post-processing method for individual sound source analysis.

The flexibility and practicality of the array were confirmed during this thesis project by the fact that it allowed multiple other experiments to take place, for which it provided satisfactory results. Most notably, this thesis project was undertaken in conjunction with another, which was aimed at optimizing microphone distributions for phased microphone arrays. This project required practical reconfigurability of the array as well as accurate data acquisition, both of which were provided.

The final outcome of the project is a modular, calibrated, multi-configurable phased microphone array. Applicability of the array for a multitude of cases has been tested and evaluated, and suggestions for additional research and improvements are provided for future projects.

Contents

Nomenclature

Greek Symbols

Symbol	Description	Dimensions	Units
α	Absorption coefficient	-	-
α	Sound attenuation coefficient	L^{-1}	$\mathrm{dB\,m^{-1}}$
β	Plate porosity	-	-
δ	Dirac delta function	-	-
$\delta_{(...)}$	Angle, features subscripts i, t and r	-	rad
ϵ	Correction factor	-	-
η	d'Alembert variable	L	m
γ	Specific heat ratio of air	-	-
λ	Wavelength	L	m
ω	Angular frequency	t^{-1}	Hz
Φ	Clean beam function	-	-
ϕ	Azimuthal angle (Spherical coordinate system)	-	rad
$\psi(\beta)$	Fok's function	-	-
ρ'	Infinitesimal density perturbation	$\mathrm{mL^{-3}}$	$\mathrm{kg\,m^{-3}}$
ρ	Density	$\mathrm{mL^{-3}}$	$\mathrm{kg\,m^{-3}}$
$\rho_{(...)}$	Density of medium identified by subscript, features subscripts $0,1,2,3...$	$\mathrm{mL^{-3}}$	$\mathrm{kg\,m^{-3}}$
ρ_∞	Static density	$\mathrm{mL^{-3}}$	$\mathrm{kg\,m^{-3}}$
θ	Polar angle (Spherical coordinate system)	-	rad
θ_O	Angular resolution offset angle	-	rad
θ_R	Angular resolution	-	rad
$\vec{\xi}$	Specific point of the source map (x, y, z)	L	m
$\vec{\xi}_{(...)}$	Point of the source map $(x_{(...)}, y_{(...)}, z_{(...)})$, features subscripts j and k	L	m
$\vec{\xi}_{max}$	Location of maximum power in the source map (x, y, z)	L	m
ξ	d'Alembert variable	L	m

Roman Symbols

Symbol	Description	Dimensions	Units
$\mathbf{A}_{band}$	Autopower matrix of given frequency band	$F^2\ L^{-2}$	Pa^2m^2
$\mathbf{A}_{dB}$	Autopower matrix in decibels	-	dB
$\mathbf{A}_{PSF}$	Autopower matrix of CLEAN-PSF	-	dB
$\mathbf{A}_{SC}$	Autopower matrix of CLEAN-SC	-	dB
$A_{(...)}$	Area of location indicated by subscript, features 1,2,3...	L^2	m^2
$\mathbf{A}$	Autopower matrix	$F^2\ L^{-2}$	Pa^2m^2
$A(\xi)$	Autopower at point ξ	F^2L^{-2}	Pa^2m^2
A	Amplitude constant	-	-
a	Complex amplitude	-	-
a_e	Effective complex amplitude	-	-
A_{jk}	Point Spread Function of the j^{th} point in the source map by k^{th} weight vector	$F^2\ L^{-2}$	Pa^2m^2
B	Amplitude of pressure wave inside contraction (Phong and Papamoschou model)	$F\ L^{-2}$	Pa
B_{jk}	Cross-power between sources at source map location j and k		
B	Plane wave equation amplitude	-	-
$\overline{\mathbf{C}}$	Trimmed CSM	$F^2\ L^{-4}$	Pa^2
$\mathbf{C}_{avg}$	Time-averaged CSM	$F^2\ L^{-4}$	Pa^2
C	Amplitude of pressure wave inside contraction (Phong and Papamoschou model)	$F\ L^{-2}$	Pa
$\mathbf{C}$	Cross-spectral matrix	$F^2\ L^{-4}$	Pa^2
$\mathbf{C}_j$	Cross-spectral matrix of j^{th} source map point	$F^2\ L^{-4}$	Pa^2
$C(f)_{mn}$	Cross-power function of microphones m and n	$F^2\ L^{-4}$	Pa^2
C	Plane wave equation amplitude	-	-
c	Constant	-	-
c	Speed of sound	$L\ t^{-1}$	$m\,s^{-1}$
$c_{(..)}$	Speed of sound in medium indicated by subscript, features 1, 2, 3...	$L\ t^{-1}$	$m\,s^{-1}$
$\mathbf{D}^{(i)}$	Degraded CSM of i^{th} iteration	$F^2\ L^{-4}$	Pa^2
D	Outer perforation diameter (Phong and Papamoschou's model)	L	m
d	Inner perforation diameter (Phong and Papamoschou's model)	L	m
d	Circular aperture	L	m
e	Euler's number	-	-
Δf	Frequency resolution	t^{-1}	Hz
F	Center frequency integer	-	-
$f_{Rayleigh}$	Rayleigh limit frequency	t^{-1}	Hz

f	Frequency	t^{-1}	Hz
f_s	Sampling frequency	t^{-1}	Hz
$\mathbf{G}^{(i)}$	CSM corresponding to maximum of source map of i^{th} iteration	F^2L^{-4}	Pa^2
$\hat{G}_{mn}(f)$	Cross-spectral density function	-	-
$\mathbf{g_j}$	Steering vector to j^{th} point in the source map	L^{-1}	m^{-1}
$\mathbf{g}$	Steering vector	L^{-1}	m^{-1}
$\mathbf{g}_{max}$	Steering vector corresponding to maximum in source map	L^{-1}	m^{-1}
$g_{(...)}$	Steering function of microphone indicates by subscript, features m and n	L^{-1}	m^{-1}
$G_{mn}(f)$	Single-sided cross-correlation function	-	-
$\mathbf{H}^{(i)}$	Diagonal CLEAN-SC matrix of i^{th} iteration	L^{-2}	m^{-2}
$\mathbf{h}^{(i)}$	Steering vector of single coherent source component	L^{-1}	m^{-1}
h	Humidity	$m\,m^{-1}$	$kg\,kg^{-1}$
$h_{\%}$	Relative humidity	$m\,m^{-1}$	$kg\,kg^{-1}$
I	Amplitude of incident wave (Phong and Papamoschou model)	$F\,L^{-2}$	Pa
I	Acoustic intensity	PL^{-2}	$W\,m^{-2}$
i	Imaginary unit	-	-
I_0	Reference sound intensity	$J\,s^{-1}\,m^{-2}$	Wm^{-2}
j	Frequency index	-	-
k	Number of discrete source map points	-	-
$K_{(...)}$	Bulk modulus of medium indicated by subscript, features 1,2,3...	$F\,L^{-2}$	Pa
k	Wavenumber	L^{-1}	m^{-1}
$k_{(...)}$	Wavenumber in direction identified by subscript, features x, y and z	L^{-1}	m^{-1}
K_s	Number of samples in dataset	-	-
k_s	Specific sample in dataset	-	-
ΔL_A	A-weighting factor	-	dB
L	Length	L	m
l	Plate thickness	L	m
l_{eff}	Effective plate thickness	L	m
L_t	Transmission loss	-	dB
Δl	Resolvable separation distance	L	m
Δo	Offset distance	L	m
L_p	Sound pressure level	-	dB
L_w	Sound power level	-	dB
m	Microphone index	-	-

N	Number of microphones in the array	-	-
n	Microphone index	-	-
P	Power	m L^2t^{-2}	W
p_e	Effective pressure	F L^{-2}	Pa
$P_j^{(i)}$	Source power of j^{th} source map point for i^{th} iteration	F^2L^{-2}	Pa^2m^2
$P_{max}^{(i)}$	Maximum value of all values for $P_j^{(i)}$	F^2L^{-2}	Pa^2m^2
$P_n(t)$	Fluctuating pressure field measured by n^{th} microphone at time t	FL^{-2}	Pa
$\hat{p}_n(f)$	Complex pressure amplitude function at n^{th} microphone	FL^{-2}	Pa
$\mathbf{p}$	Pressure vector	FL^{-2}	Pa
p'	Infinitesimal pressure perturbation	FL^{-2}	Pa
p	Pressure	FL^{-2}	Pa
$p'_{(...)}$	Infinitesimal pressure perturbation of wave in direction indicated by subscript, features i, t and r	FL^{-2}	Pa
p_∞	Static pressure	FL^{-2}	Pa
p_a	Ambient pressure	FL^{-2}	Pa
$p_n(f)$	Fluctuating pressure field measured by n^{th} microphone at frequency f	F L^{-2}	Pa
p_r	Reference pressure	FL^{-2}	Pa
Q	Directivity factor	-	-
$Q_j^{(i)}$	Source powers with clean beam normalization j^{th} point in the source map in i^{th} iteration	F^2L^{-2}	Pa^2m^2
R	Amplitude of reflected wave (Phong and Papamoschou model)	F L^{-2}	Pa
R_π	Phong and Papamoschou model reflection coefficient	-	-
R	Gas constant of air	$L^2(t^{-2}T^{-1})$	J K^{-1} kg^{-1}
R	Reflection coefficient/factor	-	-
r	Radius	L	m
r_h	Distance between a given microphone location $\vec{x}_n$ and $\vec{\xi}_h$ on the source map	L	m
$R_{m,n}(t)$	Cross correlation function	-	-
r_{ref}	Reference radius	L	m
S	Sound Power	P	W
T	Amplitude of transmitted wave (Phong and Papamoschou model)	F L^{-2}	Pa
T_{60}	Reverberation time	t	s
Δt_e	Travel time	t	s
T	Time period	t	s
T	Transmission coefficient/factor	-	-

t	Time	t	s
T_0	Start of time period T	t	s
T_r	Reference temperature	T	K
T_s	Duration of sampling period	t	s
$u_{(...)}$	Particle velocity in direction indicated by subscript, features 1,2,3...	$\mathrm{L\,t^{-1}}$	$\mathrm{ms^{-1}}$
u	Displacement at given time instant	L	m
v	Particle velocity	$\mathrm{L\,t^{-1}}$	$\mathrm{ms^{-1}}$
$(v_x)_{(...)}$	Particle velocity of wave in direction indicated by subscript, features i, r and t	$\mathrm{Lt^{-1}}$	$\mathrm{m\,s^{-1}}$
$\vec{v}$	Particle velocity vector	$\mathrm{Lt^{-1}}$	$\mathrm{m\,s^{-1}}$
V	Empirical constant	-	-
v	Velocity	$\mathrm{Lt^{-1}}$	$\mathrm{m\,s^{-1}}$
$v_{(...)}$	Velocity in direction indicated by subscript, features 1,2,3	$\mathrm{Lt^{-1}}$	$\mathrm{m\,s^{-1}}$
v_x	Particle velocity	$\mathrm{Lt^{-1}}$	$\mathrm{m\,s^{-1}}$
$\mathbf{w}$	Weight vector	$\mathrm{L^{-1}}$	$\mathrm{m^{-1}}$
$\mathbf{w}_{(...)}$	Weight vector of source map point indicated by subscript, features j and k	$\mathrm{L^{-1}}$	$\mathrm{m^{-1}}$
$\mathbf{w}_{max}$	Weight vector corresponding to maximum point in source map	$\mathrm{L^{-1}}$	$\mathrm{m^{-1}}$
W	Power	W	w
Δx	Displacement	L	m
$\vec{x}_n$	Location of n^{th} microphone (x,y,z)	L	m
x	Function variable	-	-
x	Location	L	m
x	X-Coordinate (Cartesian coordinate system)	L	m
$x_{(...)}$	Axis or direction as indicated by context (Cartesian coordinate system), features subscripts 1, 2, 3	-	-
$x_{(...)}$	X-Location of subject indicated by subscript, features j, k, m and n	L	m
y	Y-Coordinate (Cartesian coordinate system)	L	m
$y_{(...)}$	Y-Location of subject indicated by subscript, features j, k, m and n	L	m
Z	Number of time-domain signal segments	-	-
z	Z-Coordinate (Cartesian coordinate system)	L	m
$z_{(...)}$	Z-Location of subject indicated by subscript, features j, k, m and n	L	m
Z_1	Generalised impedance	$\mathrm{mL^{-2}t^{-1}}$	$\mathrm{kg\,m^{-2}\,s^{-1}}$
Z_2	Generalised impedance	$\mathrm{mL^{-2}t^{-1}}$	$\mathrm{kg\,m^{-2}\,s^{-1}}$

Sub- and superscript symbols

Symbol	Description	Subscript	Superscript
$*$	Complex conjugate	×	✓
$-$	Trimmed (diagonal removed) matrix	×	✓
$0,1,2,3...$	Specific index for given range of possible values	✓	×
$1,2,3$	Cartesian coordinate axis indicator, where 1 = X, 2 = Y, 3 = Z	✓	×
∞	Static condition	✓	×
$center$	Center frequency of frequency band	✓	×
i,r,t	Indicator for incidence, reflection and transmission respectively	✓	×
i	Indicator for iteration	✓	×
j,k	Indicator for specific source map point index	✓	×
$lower$	Lower limit of frequency band	✓	×
n,m	Microphone index	✓	×
ref	Reference value	✓	×
$upper$	Upper limit of frequency band	✓	×
x,y,z	Direction indicator	✓	×

List of Figures

List of Tables

1 Introduction

The air transport sector is one of the fastest growing transportation sectors around the globe, for both cargo and passengers[26]. When demand increases, eagerness to supply is soon to follow, and airports everywhere are looking for ways to expand. However, restrictions on pollution, safety and noise hamper expansion near densely populated areas. This is quite a difficult issue to solve, and the scientific community as well as aircraft manufacturers are constantly trying to improve aircraft in these fields.

When it comes to noise pollution, the aircraft sector is not the only source. The wind energy sector is expanding and growing at a rapid pace, and more and more nations are slowly making a (partial) transition to this cleaner, more sustainable form of energy production. To develop quieter wind turbine blades is an important step in the process of making wind energy a more viable replacement of fossil fuels, since the noise restrictions imposed by local or national governments are preventing energy generation in certain areas or at certain times of day[51].

To aid in the decrease of noise pollution by aircraft and wind turbines, experiments with small scale models can provide valuable information on noise source location and strength. These experiments are usually performed in wind tunnels, where the noise analysis is done using an acoustic array (a structure containing a set of microphones, distributed in a predefined pattern). The design of such an array is a complex process, but its final shape and layout have an understandably large influence on the quality and therefore usability of the resulting data.

The realization of an anechoic, vertical wind tunnel at the Delft University of Technology is aimed at serving as a reliable, accurate platform for (amongst other subjects) acoustic analysis. To perform this acoustic analysis, the design of a new acoustic array is of paramount importance to make full use of the new options this tunnel has to offer. The Aircraft Noise and Climate Effects (ANCE) section has recently purchased a set of new array microphones for more accurate measurements to be performed in this tunnel, and a data-acquisition system for these microphones has also already been chosen and purchased by the Aerodynamics, Wind Energy, Flight Performance and Propulsion (AWEP) department. What remains is to determine how to employ this new equipment as efficiently and usefully as possible, which is the subject of this thesis project.

The design of an acoustic array depends on the intended application. In the field of Noise Source Identification (NSI), techniques can be grouped into two main categories; beamforming and near-field acoustic holography (NAH). Since the objective for this thesis is the design of a beamforming array, the other category is not discussed further[1]. Within the beamforming discipline, the main technique used is conventional beamforming, also referred to as delay-and-sum beamforming. Other techniques, such as adaptive beamforming [23][61] and functional beamforming[12][13], provide slight variations to the conventional approach. To improve the accuracy and clarity of results obtained with beamforming, a deconvolution algorithm can be applied. Examples of commonly used deconvolution methods are DAMAS[6] and CLEAN[58], as well as variants and improvements on these methods. CLEAN-SC stands out in particular, due to its ability to provide highly accurate results whilst requiring comparably short additional computation time[55][36].

[1] If required for further orientation, additional information can be found in reference [19] and [30]

The effectiveness of the application of deconvolution algorithms depends on the accuracy of the initially obtained data, which is fully dependent on the test setup (i.e. the acoustic array and the testing environment) and the microphone distribution. The main two components dictating the quality of obtained results are the main lobe beam width, and the presence of side lobes. Whereas the former depends mainly on the size of the array, the latter is dictated by the microphone distribution. A high number of microphones generally leads to better results[1], and placing them conform the Underbrink spiral[54][47] is currently regarded as the optimal configuration in terms of all-round performance.

Common suppliers of acoustic arrays are Brüel & Kjaer[7] and Gfai Tech[18], which offer arrays ranging in shape, size and microphone distribution depending on the intended application and therefore often based on customer requirements. However, these arrays do not support changes in microphone distribution, as this usually requires recalibration to identify the new microphone locations[31]. Enabling reconfiguration of the microphone distribution whilst maintaining accurate knowledge of the microphone positions would result in a more flexible array.

Based on research into the aforementioned subjects, the research objective for this thesis project was formulated as:

...To obtain a practical method of performing accurate acoustic measurements in the anechoic vertical wind tunnel at the Delft University of Technology by designing, creating, testing and evaluating a reconfigurable phased microphone array using state-of-the-art techniques and equipment.

The leading research question to aid in achieving this objective was formulated as:

What design of an acoustic array for the anechoic vertical wind tunnel at the Delft University of Technology should be used to obtain optimal acoustic analysis results in terms of accuracy in level and location estimation of sound sources, spatial resolution and side- and grating lobe presence?

A number of research sub-questions was formulated to aid in the achievement of this objective, which are shown in Appendix F. The steps taken to answer these questions and thereby achieve the research objective are treated in this report, preceded by a short explanation of the relevant fundamentals in acoustic analysis. Since the research objective clearly states four distinct steps to be taken in achieving that objective, each phase of the project (design, creation, testing and evaluation) is treated separately, finally resulting in a flexible, practical and accurate array system, capable of supporting a multitude of acoustic analysis objectives.

2

Fundamentals of acoustic analysis with beamforming

This chapter introduces the basics of acoustic analysis. The first section discusses the physics behind the origin and propagation of sound waves, which is used in beamforming for the formulation of the steering vectors. The second section explains the approach to and workings of conventional beamforming, and the subsequent section covers the deconvolution methods CLEAN-PSF and CLEAN-SC, based in part on the concepts discussed in the first section. These methods are used throughout the testing and evaluation phases of this project. The fourth section covers a small subset of signal analysis subjects applicable to this project. The fifth section elaborates on the reflection and refraction of sound waves when a transition between mediums occurs (depending on the choice of array structure, reflections can cause constructive and/or destructive interference with the measured signal). Finally, the influence of the microphone distribution over an array is discussed.

2.1. Monopole sound emission

As formulated by Bai, Ih and Benetsy[3]: *"Sound is a mechanical wave that propagates through a compressible medium. Sound is transmitted in the form of longitudinal waves described by the wave equation. Acoustics is rooted in fluid dynamics and can also be regarded as a simplified version of fluid dynamics that deals primarily with small perturbation quantities in a non-viscous medium."*

The simplest sound source is a single monopole source, i.e. a source that emits equally in all directions. The wave equation for a monopole source in three dimensions is given as

$$\nabla^2 p' - \frac{1}{c^2}\frac{\partial^2 p'}{\partial t^2} = 0. \tag{2.1}$$

In this equation, $p'(x, y, z, t)$ is an acoustic pressure perturbation in Cartesian coordinates as a function of time, defined as $p - p_\infty$, and c is the speed of sound. Here, p' is freely interchangeable with ρ', defined as $\rho - \rho_\infty$. The full derivation of this equation can be found in Appendix A. The acoustic pressure for harmonic waves can be expressed at a function of time as follows:

$$p'(x, y, z, t) = p'(x, y, z)e^{i\omega t}, \tag{2.2}$$

where ω (the radial frequency) is expressed as a function of frequency by $\omega = 2\pi f$. The second time derivative of this expression can be found as

$$\frac{\partial^2}{\partial t^2}\left(p' e^{i\omega t}\right) = -\omega^2 p' e^{i\omega t} \tag{2.3}$$

By substituting Equation 2.3 back into Equation 2.1, the wave equation becomes

$$\nabla^2 p' e^{i\omega t} + k^2 p' e^{i\omega t} = \left(\nabla^2 p' + k^2 p'\right) e^{i\omega t} = 0. \tag{2.4}$$

In Equation 2.4, k represents the wave number, defined as $k = \omega/c$. Since $e^{i\omega t} \neq 0$ for all values of t, the following must be true:

$$\nabla^2 p' + k^2 p' = 0. \tag{2.5}$$

Equation 2.5 is known as the Helmholtz equation, which describes the acoustic pressure field. Since a monopole source is considered, this equation can be expressed in radial coordinates rather than Cartesian, as

$$\frac{\partial^2 p'}{\partial r^2} + \frac{2}{r}\frac{\partial p'}{\partial r} + k^2 p' = 0. \tag{2.6}$$

The solution to Equation 2.6 is given as

$$p'(r) = \frac{A}{r} e^{-ikr}, \tag{2.7}$$

where A is the reference amplitude of the pressure wave (taken at 1 meter from the source), and r is the radial distance from the source. Combining this solution with the harmonic wave time dependence $e^{i\omega t}$ component identified earlier yields the full wave equation for acoustic pressure, as

$$p'(r,t) = \frac{A}{r} e^{-ikr} e^{i\omega t} = \frac{A}{r} e^{i(\omega t - kr)}. \tag{2.8}$$

For the calculation of sound pressure levels, the obtained pressure is converted to effective pressure, by using

$$p_e = \frac{|p'|}{\sqrt{2}} \tag{2.9}$$

2.2. The basic principles of conventional beamforming

To correctly identify the position and strength of a sound source from acoustic measurements, conventional (delay-and-sum) beamforming can be applied to the obtained data. This data is usually obtained with a set of microphones, distributed along an acoustic array. When a pressure perturbation p' occurs near a microphone, the microphone membrane vibrates. This vibration induces a voltage difference, which is recorded by a data-acquisition system and transformed to the corresponding pressure fluctuation.

Consider a set of N microphones, located in a Cartesian coordinate system, with their positions expressed as $\vec{x}_n$, which is defined as follows.

$$\vec{x}_n = (x_n, y_n, z_n) \tag{2.10}$$

In this representation, n is a value between 1 and N, indicating a specific microphone. The pressure differences measured by the microphones at a given sampling frequency f_s and during a given time period T_s are denoted by P_n. This measured data can be transformed from the time domain to the frequency domain by means of a discrete Fourier transform.

$$p_n(f) = \frac{2}{K_s} \sum_{k_s=1}^{K_s} P_n(k_s) e^{-2\pi i f k_s \Delta t} \tag{2.11}$$

In Equation 2.11, K_s equals the amount of samples in P_n, and k_s signifies a specific sample from P_n. The resulting $p_n(f)$ contains the complex pressure amplitudes of microphone n for frequency f.

In conventional beamforming, this is done for all N microphones for a frequency f. This results in the pressure vector $\mathbf{p}$, defined as shown in Equation 2.12.

$$\mathbf{p} = \begin{bmatrix} p_1(f) \\ \vdots \\ p_N(f) \end{bmatrix} \tag{2.12}$$

In beamforming, a source map containing J discrete points is used, mapping the region in which one or multiple sources are expected. A single discrete point $\vec{\xi}$ in this map is considered,

$$\vec{\xi} = (x, y, z). \tag{2.13}$$

This is further clarified in Figure 2.1. The distance between microphone n and source map point $\vec{\xi}$ is defined as:

$$r_n = |\vec{x}_n - \vec{\xi}| \tag{2.14}$$

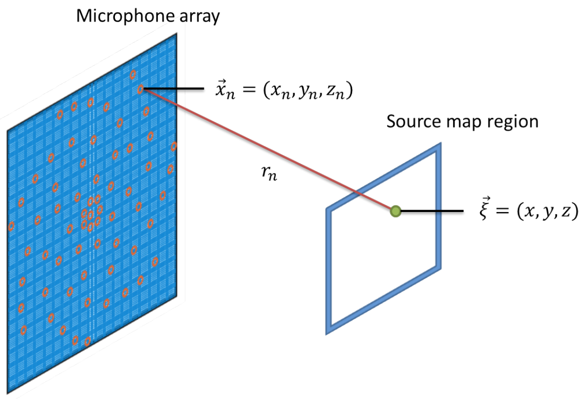

Figure 2.1: Acoustic array and beamforming source map

The results obtained in Equation 2.12 can be projected onto the source map with the use of steering vector $\mathbf{g}$. This steering vector consists of N components, one for each microphone n, for a specific source map point $\vec{\xi}$. These N components are determined with Equation 2.15 (for stationary sources)

$$g_n = \frac{e^{-2\pi i f \Delta t_e(\vec{x}_n, \vec{\xi})}}{4\pi r_n} \tag{2.15}$$

The steering vector can be defined in multiple ways[53], and describes the assumed propagation of sound at the given velocity c for the given distance r_n, accounting for the energy loss due to geometrical spreading as well as the phase difference between the point of reception and the source map. The formulation given in Equation 2.15 is used throughout this thesis work. In this equation, $\Delta t_e(\vec{x}_n, \vec{\xi})$ is defined as the time delay between $\vec{\xi}$ and $\vec{x}_n$:

$$\Delta t_e(\vec{x}_n, \vec{\xi}) = \frac{r_n}{c} \tag{2.16}$$

This definition of the steering vector is the most commonly used definition, and is based on the wave equation derived earlier (Equation 2.8). The goal of beamforming is to find the complex pressure amplitude a at the source map point $\vec{\xi}$. The steering vector $\mathbf{g}$ corrects for the change in signal amplitude and phase over the distance from each point $\vec{x}_n$ to point $\vec{\xi}$. To find a, the received pressures in vector $\mathbf{p}$ must be used to solve the minimization problem between the measured pressure vector $\mathbf{p}$ and modeled pressure vector $a\mathbf{g}$:

$$J = ||\mathbf{p} - a\mathbf{g}||. \tag{2.17}$$

The solution of which is the following,

$$a = \frac{\mathbf{g}^*\mathbf{p}}{||\mathbf{g}||^2}. \tag{2.18}$$

Since acoustic analysis is performed on effective pressure rather than actual pressure, the following correction needs to be applied (see Equation 2.9):

$$a_e = \frac{|a|}{\sqrt{2}}. \tag{2.19}$$

For conventional beamforming, the source autopowers are considered. These are defined as

$$A(\vec{\xi}) = a_e^2 = \frac{1}{2}|a|^2 = \frac{1}{2}aa^* = \frac{1}{2}\frac{\mathbf{g}^*\mathbf{p}}{||\mathbf{g}||^2}\left(\frac{\mathbf{g}^*\mathbf{p}}{||\mathbf{g}||^2}\right)^* = \frac{1}{2}\frac{\mathbf{g}^*\mathbf{p}\mathbf{p}^*\mathbf{g}}{||\mathbf{g}||^4} = \frac{\mathbf{g}^*\mathbf{C}\mathbf{g}}{||\mathbf{g}||^4} \tag{2.20}$$

The factor $\mathbf{C}$ in Equation 2.20 is the cross-spectral matrix. The cross power of microphones m and n is noted as $C(f)_{mn}$, and is obtained with Equation 2.21,

$$C(f)_{mn} = \frac{1}{2}p_m(f)p_n^*(f). \tag{2.21}$$

This function expresses the cross-correlation between microphones m and n for a given frequency f. Equation 2.21 also holds for vector $\mathbf{p}$, and for a given frequency f results in the $N \times N$ cross spectral matrix $\mathbf{C}$, as shown in Equation 2.22,

$$\mathbf{C} = \frac{1}{2}\mathbf{p}\mathbf{p}^*. \tag{2.22}$$

This matrix therefore also contains the cross power of all microphones with themselves, located on the diagonal. Since this information merely contains the noise without coherence between microphones, it does not provide information with any significance for the further process of beamforming. Hence, the CSM can be trimmed by removing the diagonal, as demonstrated in Equation 2.23,

$$\overline{\mathbf{C}}(m,n) = 0 \text{ for m == n, where m = 1...N, n = 1...N,} \tag{2.23}$$

grating the trimmed CSM $\overline{\mathbf{C}}$.

Equation 2.20 results in the source autopower at point $\vec{\xi}$. Now, consider the source map consisting of J discrete points, defined as:

$$\vec{\xi}_j = (x_j, y_j, z_j),\ j = 1...J \tag{2.24}$$

The resulting matrix **A** contains the source autopowers of every discrete point $\vec{\xi}_j$ in the source map, and therefore contains J elements. This is the result of conventional beamforming, and can be represented as shown in Figure 2.2.

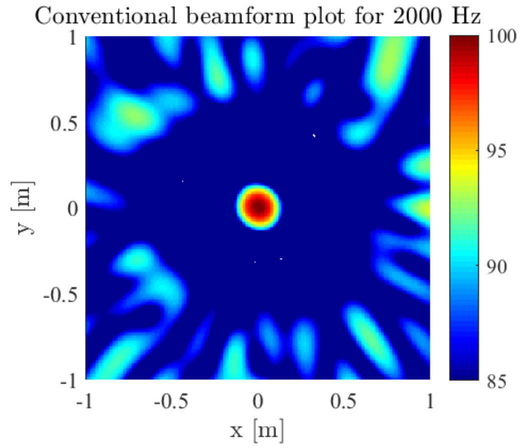

Figure 2.2: Conventional beamforming result example (PSF obtained through simulation)

The autopower matrix **A** contains values of Pascal meter squared (Pa^2m^2), which is not a useful unit. Instead, the logarithmic result is shown, referenced to a pressure of 20 μPa[1] and at a reference distance of r_{ref} from the source. This is the result as shown in Figure 2.2, and is done using Equation 2.25,

$$\mathbf{A}_{dB} = 20\log_{10}\left(\frac{\sqrt{\mathbf{A}}}{4\pi r_{ref}}\frac{1}{p_{ref}}\right). \tag{2.25}$$

$\mathbf{A}_{dB}$ contains the Sound Pressure Levels of each grid point $\vec{\xi}_j$. The sound pressure level is commonly expressed with symbol L_p. To calculate the sound power L_w of a source rather than the sound pressure at a reference distance, a correction must be applied, by means of the following equation:

$$L_w = L_p - 10\log_{10}\left(\frac{Q(\theta,\phi)}{4\pi r_{ref}^2}\right) - 10\log_{10}\left(\frac{I_0\rho_\infty c}{p_{ref}^2}\right) \approx L_p + 10.8 + 20\log_{10}\left(r_{ref}\right) - DI(\theta,\phi). \tag{2.26}$$

Here, $Q(\theta,\phi)$ is the directivity factor of the sound source, describing its emission pattern[28][38], and I_0 is the reference sound intensity. The factor Q without any annotations is taken along its principal axis ($\theta = 0, \phi = 0$). Directionality of a sound source can also be expressed using directivity index DI, calculated as:

$$DI\left(\theta,\phi\right) = 10\log_{10}\left(Q\left(\theta,\phi\right)\right). \tag{2.27}$$

For a perfect monopole sound source, $Q\left(\theta,\phi\right)$ is equal to 1 and $DI\left(\theta,\phi\right)$ is 0 for all values of θ and ϕ.

[1]This pressure corresponds to the threshold of human hearing

2.3. CLEAN methods to improve conventional beamforming

The quality of the results obtained with conventional beamforming for a given frequency depend significantly on the microphone distribution used. Whereas the maximum obtainable resolution is restricted by the Rayleigh limit[5], the presence, position and strength of side lobes are directly related to the microphone distribution (discussed in Section 2.6). For a given array aperture, the Rayleigh limit is fixed, and cannot be altered except by increasing the aperture. The side lobe presence however can be analyzed and reduced by using a deconvolution approach, such as CLEAN-PSF or CLEAN-SC.

The original CLEAN approach to deconvolution, as described by Sijtsma[58], is now commonly referred to as CLEAN-PSF, as discussed in Section 2.3.1. This is to avoid confusion with the later developed CLEAN-SC, which is discussed in Section 2.3.2. However, both methods are based on the same initial input and are therefore similar up to a certain degree. This common ground is explained before delving into the difference in approach between the two methods.

The way to obtain the CSM $\mathbf{C}$ was established in Equation 2.22. This matrix consists of the cross powers of all N microphones, as explained in Equation 2.21, and is therefore of size $N \times N$. The trimmed CSM $\overline{\mathbf{C}}$ (Equation 2.23) is used in the remainder of this section. Along with the trimmed CSM, a weight vector can be defined as follows:

$$\mathbf{w} = \mathbf{g}\left(\sum_{(m,n)} |g_m|^2 |g_n|^2\right)^{-1/2} \tag{2.28}$$

And with this, Equation 2.20 can be rewritten as

$$A = \mathbf{w}^* \overline{\mathbf{C}} \mathbf{w} \tag{2.29}$$

Now, consider a scan grid consisting of J points, with a point source located in the j^{th} point. The CSM obtained from this source can be represented as:

$$\mathbf{C}_j = \mathbf{g}_j \mathbf{g}_j^* \tag{2.30}$$

This results in the source autopower A_{jk}, using equation 2.29 as shown in Equation 2.31

$$A_{jk} = \mathbf{w}_k^* \overline{\mathbf{C}}_j \mathbf{w}_k = \mathbf{w}_k^* \overline{[\mathbf{g}_j \mathbf{g}_j^*]} \mathbf{w}_k \tag{2.31}$$

This specific autopower equation, called the Point Spread Function (PSF) signifies the response of the array to a point source located in $\vec{\xi}_j$. $A_{jk} = 1$ for $j = k$, but due to the nature of beamforming it is not zero in all other locations for a finite number of microphones. Microphone distributions are usually optimized to reduce this error for a given (range of) frequency/-ies, and further options to improve the resulting autopower matrix can be found in deconvolution methods, for example CLEAN-PSF or CLEAN-SC.

2.3.1. Deconvolution with CLEAN-PSF

Improving the autopower matrix by using CLEAN-PSF is an iterative process, where i is the iteration indicator. The first step toward using CLEAN-PSF is obtaining the source autopower matrix by means of conventional beamforming. This is defined as the 0^{th} iteration, resulting in a CSM $\mathbf{C}$. This CSM is defined as the first degraded CSM:

$$\mathbf{D}^{(i)} = \mathbf{D}^{(0)} = \mathbf{C} \tag{2.32}$$

The aforementioned CSM can be used to calculate the source powers for all points $\vec{\xi}_j$:

$$P_j^{(0)} = \mathbf{w}_j^* \overline{\mathbf{D}}^{(0)} \mathbf{w}_j \tag{2.33}$$

The maximum value and its corresponding source map index j are taken from $P^{(0)}$. This is used to establish the CSM corresponding to this maximum, based on the steering vector corresponding to $\vec{\xi}_{max}$:

$$\mathbf{G}^{(i)} = P_{max}^{(i-1)} \mathbf{g}_{max}^{(i)} \mathbf{g}_{max}^{*(i)} \tag{2.34}$$

The contribution of the source in $\vec{\xi}_{max}$ is then subtracted from the dirty map as follows:

$$P_j^{(i)} = P_j^{(i-1)} - \mathbf{w}_j^* \overline{\mathbf{G}}^{(i)} \mathbf{w}_j \tag{2.35}$$

This equation indicates the iterative component to CLEAN-PSF, which is to update the previously obtained map by subtracting the PSF corresponding to the maximum value in said map.

The PSF corresponding to the maximum value at $\vec{\xi}_{max}$ is not saved as such, but rather reduced to a normalized clean beam as follows:

$$Q_j^{(i)} = P_{max}^{(i-1)} \Phi(\vec{\xi}_j - \vec{\xi}_{max}^{(i)}) \tag{2.36}$$

The width of Φ is to be specified by the user.

The next iteration is started by declaring a new degraded CSM:

$$\mathbf{D}^{(i)} = \mathbf{D}^{(i-1)} - P_{max}^{(i-1)} \mathbf{g}_{max}^{(i)} \mathbf{g}_{max}^{*(i)} \tag{2.37}$$

The suggested stop criterion for convergence is given as:

$$||\overline{\mathbf{D}}^{i+1}|| \geq ||\overline{\mathbf{D}}^{(i)}|| \tag{2.38}$$

In other words, when the current degraded CSM contains more information than the previous degraded CSM, further application of the deconvolution method does not result in a cleaner source map. At this point, the final iteration value is denoted as I, and the collected clean beams in Q are summed and added to the remaining map, as follows:

$$A_j = \sum_{i=1}^{I} Q_j^{(i)} + P_j^{(I)} \tag{2.39}$$

When executed for all points $\vec{\xi}_j$, this results in a CLEAN-PSF autopower matrix $\mathbf{A}_{PSF}$. The reason this method is named CLEAN-PSF lies in its core assumption, which is that the initially obtained map ($\mathbf{D}^{(0)}$) is built up out of PSF's corresponding to the maxima in the autopower matrix. By looking at these maxima in each iteration, a new location and value for a source and its power are found and added to the clean-beam matrix Q. However, the assumption that a source autopower map is solely built up of 'perfect' point sources at the location of the maxima is very restrictive, and the obtainable result using this method is therefore limited in applicability in actual acoustic measurements. An alternative was developed to solve issues encountered with CLEAN-PSF, which was aptly named CLEAN-SC and is explained in the following section.

2.3.2. Deconvolution with CLEAN-SC

CLEAN-SC uses a slightly different approach than PSF, making use of the fact that side lobes are by definition coherent with the main lobe, which can be used to identify main- and side lobes, thereby cleaning up the source map. The cross-power between two sources is defined as follows:

$$B_{jk} = \mathbf{w}_j^* \overline{\mathbf{C}} \mathbf{w}_k \tag{2.40}$$

Equation 2.35 is applicable for CLEAN-SC as well, but with a different formulation of $\mathbf{G}$. Whereas CLEAN-PSF formulates $\mathbf{G}$ based on the maximum in the source map, CLEAN-SC requires that all scan points ξ_j in the source map are determined by $\mathbf{G}$, expressed as:

$$\mathbf{w}_j^* \overline{\mathbf{D}}^{(i-1)} \mathbf{w}_{max}^{(i)} = \mathbf{w}_j^* \overline{\mathbf{G}}^{(i)} \mathbf{w}_{max}^{(i)} \text{ for all } \mathbf{w}_j \tag{2.41}$$

However, there is no unique solution for $\mathbf{G}^{(i)}$ in this formulation. Therefore, a constraint has to be formulated with regard to the definition of $\mathbf{G}^{(i)}$, which is done by assuming that there is a single coherent source component $\mathbf{h}^{(i)}$ such that:

$$\mathbf{G}^{(i)} = P_{max}^{(i-1)} \mathbf{h}^{(i)} \mathbf{h}^{*(i)} \tag{2.42}$$

Herein lies the main difference between CLEAN-PSF and CLEAN-SC; where both methods assume the source map to be built up out of point sources, CLEAN-PSF cleans the source map by subtracting the PSF of this maximum calculated with the known steering vector **g**, whereas CLEAN-SC uses vector **h** based on coherence between main- and side lobes. The trimmed variant to Equation 2.42 is as follows:

$$\overline{\mathbf{G}}^{(i)} = P_{max}^{(i-1)}\overline{\mathbf{h}^{(i)}\mathbf{h}^{*(i)}} = P_{max}^{(i-1)}(\mathbf{h}^{(i)}\mathbf{h}^{*(i)} - \mathbf{H}^{(i)}) \tag{2.43}$$

In this equation, $\mathbf{H}^{(i)}$ is a diagonal matrix defined as:

$$\overline{\mathbf{H}}(m,n) = 0 \text{ for m} \neq \text{n}, \tag{2.44}$$

$$= h_m^{(i)} h_n^{*(i)} \text{ for m = n, where m = 1...N, n = 1...N} \tag{2.45}$$

The determination of $\mathbf{h}^{(i)}$ is performed iteratively, starting by defining $\mathbf{h}^{(i)}$ as $\mathbf{g}_{max}^{(i)}$, and then employing Equation 2.46.

$$\mathbf{h}^{(i)} = \frac{1}{\left(1 + \mathbf{w}_j^* \mathbf{H}^{(i)} \mathbf{w}_{max}^{(i)}\right)^{1/2}} \left(\frac{\overline{\mathbf{D}}^{(i-1)} \mathbf{w}_{max}^{(i)}}{P_{max}^{(i-1)}} + \mathbf{H}^{(i)} \mathbf{w}_{max}^{(i)} \right) \tag{2.46}$$

This provides all the necessary components for a new definition of $\mathbf{G}^{(i)}$, which enables the rewriting of Equation 2.37 into:

$$\mathbf{D}^{(i)} = \mathbf{D}^{(i-1)} - P_{max}^{(i-1)} \mathbf{h}_{max}^{(i)} \mathbf{h}_{max}^{*(i)} \tag{2.47}$$

The same suggested stop criterion can be used for the CLEAN-SC iterative process. After I iterations, the result is obtained by using Equation 2.48

$$\mathbf{C} = \sum_{i=1}^{I} P_{max}^{(i-1)} \mathbf{h}^{(i)} \mathbf{h}^{*(i)} + \mathbf{D}^I \tag{2.48}$$

Since the first term on the right hand side contains all dominating sources (and the second term contains mostly noise), the first term is sufficient to describe the source map. This can be obtained by using

$$\sum_{n=1}^{N} C_{nn} = \sum_{i=1}^{I} P_{max}^{(i-1)} ||\mathbf{h}^{(i)}||^2 \tag{2.49}$$

This is known as the trace of the CSM, and is commonly taken as the final result of deconvolution by means of CLEAN-SC (i.e. without the contribution of $\mathbf{D}^{(I)}$).

2.3.3. Applying CLEAN deconvolution to measure array performance

As explained in the previous two sections, the crucial difference between CLEAN-SC and CLEAN-PSF lies in the way they determine the strength and location of potential sound sources; CLEAN-PSF calculates the PSF corresponding to the maximum in the source map based on known steering vectors **g**, whereas CLEAN-SC searches for a set of steering vectors **h** providing the best fit in terms of main- and side lobe coherence.

Both deconvolution methods are based on the initially obtained PSF and steering vector by means of conventional beamforming. The better the match between the simulated (theoretical) PSF and the experimental data, the better the result obtained with either method. Especially CLEAN-PSF, which is based purely on the accuracy within which the theoretical and measured PSF match, is highly dependent on the clarity and accuracy of the initially obtained PSF. This means that the quality of the output data is a direct measure for the array performance in terms of being able to provide accurate measurement data and accurate knowledge on the microphone positions, the first of which is particularly interesting at low signal-to-noise ratio's, where measurement errors and/or offsets have a more pronounced effect. This subject is discussed further and tested in Sections 5.4 and 5.5.

Whereas both methods are expected to work well for point sources in general, an improved result for low signal-to-noise ratios is expected with CLEAN-SC when compared to CLEAN-PSF, due to the inclusion of coherence in cleaning up the autopower matrix. The sound source maxima in the source map will be relatively low compared to the surrounding noise, whilst the coherence between main- and side lobes is largely unaffected. Since the main assumption in either CLEAN method is based around subtracting PSF's from the initially obtained map to provide a cleaner result, these methods are best used when individual incoherent (point) sources are concerned. Distributed sources or multiple closely-spaced sources are significantly more difficult to detect, and may not be correctly identified with either approach.

2.4. Signal analysis

When collecting acoustic pressure data, this is done over a certain sampling period of duration T_s at a sampling frequency f_s. The maximum frequency that can be analyzed from the Fourier transform equals half the sampling frequency. This is the Nyquist frequency[62], and any attempt to obtain results for higher frequencies without increasing the sampling frequency will result in aliasing. The effect of aliasing is shown in Figure 2.3.

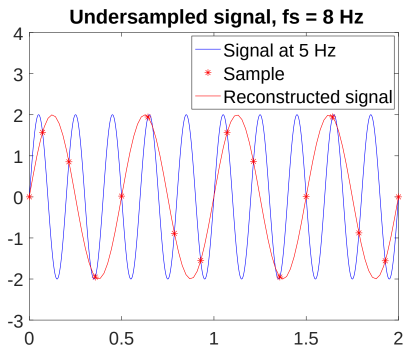

(a) Aliasing

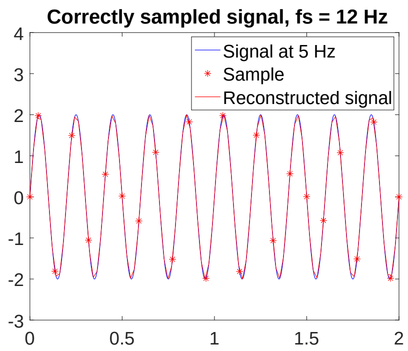

(b) Correct sampling

Figure 2.3: Minimum sampling frequency to avoid aliasing

As demonstrated in Figure 2.3a, the reconstructed signal obtained from an under-sampled sinusoid at a frequency of 5 Hz results in a sinusoid at a frequency of 2 Hz. A sufficiently high sampling frequency (Figure 2.3b) prevents this, and allows for correct reconstruction of the original signal. The obtainable frequency resolution obtainable from the Fourier transform is determined by the sampling period length, as

$$\Delta f = \frac{1}{T_s}. \tag{2.50}$$

Frequency spectrum analysis is commonly done in frequency bands rather than for individual frequencies. A commonly used distribution of frequency bands are the third octave bands, which are defined as follows,

$$f_{center} = \left(2^{[F]/3}\right) 10^3 \tag{2.51}$$

$$f_{upper} = 2^{1/6} f_{center} \tag{2.52}$$

$$f_{lower} = 2^{-1/6} f_{center}. \tag{2.53}$$

Here, F is an integer between -18 and 13.

Aside from splitting frequencies into bands for analysis, a weighting factor is often applied to make the recorded SPL more representative for a given type of analysis. A-weighting is a common weighting method, which is applied to represent the obtained frequency domain data relative to the sensitivity of the human ear. Since the human ear is less sensitive to frequencies lower than 20 Hz and higher than 20.000 Hz, these are reduced by the application of A-weighting. The A-weighting is applied as shown in Figure 2.4. Calculation of the A-weighting is done with Equation 2.54 as

$$\Delta L_A = -145.528 + 98.262 * \log_{10}(f) - 19.509 * \log_{10}^2(f) + 0.975 * \log_{10}^3(f). \tag{2.54}$$

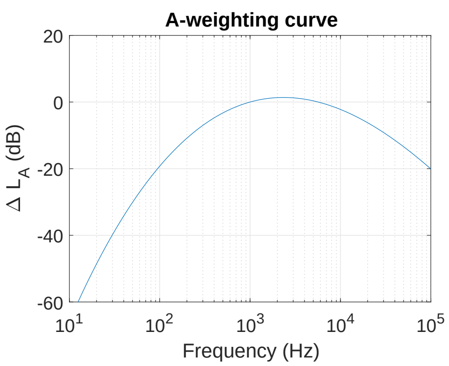

Figure 2.4: A-Weighting curve

The total power in a frequency spectrum can be integrated, which is referred to as the OSPL, or Overall Sound Pressure Level, of that spectrum. This is used for assessing the total noise emitted by a specific source, and the OSPL or A-weighted OSPL (OASPL) are commonly used to quantify noise pollution.

2.5. Sound reflection and refraction

Sound generated from a monopole point source will propagate equally in every direction (unless inhibited). This results in a spherical wavefront, as exemplified by Figure 2.5. In this image, the initial input energy W is spread out over an increasingly larger wavefront area, effectively decreasing the intensity. Sound intensity I at a distance r is therefore defined as:

$$I = \frac{W}{4\pi r^2}. \tag{2.55}$$

This is the definition of geometrical spreading.

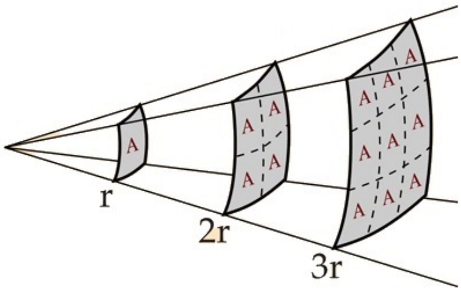

Figure 2.5: Spherical wavefront[49]

At some distance r from the source, the incident wavefront will be much larger than the size of the analysis device. At this point, the wavefront can be modeled as a plane wave rather than a spherical wavefront, because the curvature of the wavefront experienced at the analysis device is negligible, and can therefore be modeled as a plane. This is known as the plane wave assumption. Unless specifically indicated, this assumption is not made throughout this project. In free space, sound propagation is described as shown in the previous sections. However, any objects consisting of a different medium obstructing the wavefront will alter the propagation direction and amplitude of the incoming sound wave, by means of reflection and/or refraction.

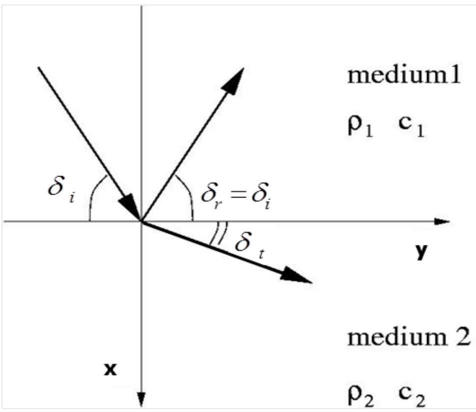

Figure 2.6: Snell's Law[60]

Figure 2.6 shows the concept of Snell's Law. This law, which is also used for analyzing the behavior of light, is expressed as shown in Equation 2.56,

$$\frac{\cos(\delta_r)}{c_1} = \frac{\cos(\delta_i)}{c_1} = \frac{\cos(\delta_t)}{c_2}. \tag{2.56}$$

For a sufficiently small incidence plane compared to the wavefront, the plane wave assumption holds. With this assumption, the incident, reflected and refractured (transmitted) plane waves p'_i, p'_r and p'_t can be written as follows:

$$p'_i = Ae^{i(\omega t - \vec{k}\vec{r})} \tag{2.57}$$

$$\vec{k}\vec{r} = k_x x + k_y y + k_z z \tag{2.58}$$

$$p'_i = Ae^{i(\omega t - x\sin(\delta_i)\omega/c_1 - y\cos(\delta_i)\omega/c_1)} \tag{2.59}$$

$$p'_r = Ce^{i(\omega t + x\sin(\delta_r)\omega/c_1 - y\cos(\delta_r)\omega/c_1)} \tag{2.60}$$

$$p'_t = Be^{i(\omega t - x\sin(\delta_t)\omega/c_2 - y\cos(\delta_t)\omega/c_2)}. \tag{2.61}$$

The full derivation of coefficients A, B and C is given in Appendix B, and amounts to the following:

$$A + C = B \tag{2.62}$$

$$Z_1 = \frac{\rho_1 c_1}{\sin(\delta_i)} \tag{2.63}$$

$$R = \frac{C}{A} = \frac{Z_2 - Z_1}{Z_2 + Z_1} \tag{2.64}$$

$$A - C = B\frac{\rho_1 c_1 \sin(\delta_t)}{\rho_2 c_2 \sin(\delta_i)} \tag{2.65}$$

$$Z_2 = \frac{\rho_2 c_2}{\sin(\delta_t)} \tag{2.66}$$

$$T = \frac{B}{A} = \frac{2Z_2}{Z_2 + Z_1}. \tag{2.67}$$

Z_1 and Z_2 are the generalized acoustic impedances of the two media, whereas R and T are the acoustic reflection and transmission coefficient, respectively.

These latter coefficients are direct indicators for the amount of energy of the incoming wave which is reflected on the incidence plane, or transmitted through the new medium.

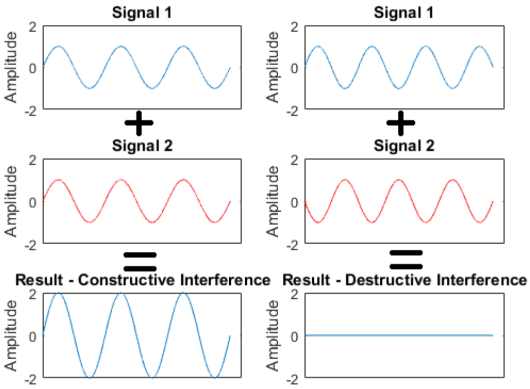

Figure 2.7: Constructive and destructive interference

The significance of the potential effects of constructive and destructive interference are exemplified in Figure 2.7. Assuming complete reflection ($R = 1$), the phase difference between the incident and the reflected wave is the main factor to determine the resulting signal. As shown in Figure 2.7 , fully constructive interference results in a doubling of pressure amplitude, whereas fully destructive interference effectively cancels out the signal altogether. The phase at which both signals are recorded (for a given wavelength) depends on the position of the microphone with respect to the reflection surface as well as the original source.

Apart from being reflected or transmitted, incident sound waves can also be absorbed by the incidence medium, indicated by the acoustic absorption coefficient α. This coefficient depends mainly on the material of the incidence medium and the frequency of the incident sound wave. The books by Hall[22] and Vorländer[65] each provide an overview of the absorption coefficients of commonly used materials.

Since reflection of the sound wave incident to the array can lead to interference, either a high transmission or a high absorption coefficient (or a combination of both) is preferential for optimal array performance. Seeing as the absorption coefficient is mainly dictated by material properties, the benefits of this advantage must be traded of against the structural requirements on the material (i.e. providing sufficient structural support and stiffness to practically employ the array).

2.6. Influence of microphone placement

In the previous sections, the steps to obtain a source autopower map using conventional beamforming, CLEAN-PSF and CLEAN-SC have been explained, along with the dependence of both deconvolution methods on a good initial PSF. The main variables that are free to choose are the source map grid $\vec{\xi}_k$ and the microphone positions $\vec{x}_n$, the influence of which has not been clarified yet.

The number of points J distributed over the source map can have an influence on the results, especially in terms of computation time required and resolution obtained. Resolution is defined by the Merriam-Webster dictionary as

1. *'the process or capability of making distinguishable the individual parts of an object, closely adjacent optical images, or sources of light'*, or
2. *'a measure of the sharpness of an image or of the fineness with which a device (such as a video display, printer, or scanner) can produce or record such an image usually expressed as the total number or density of pixels in the image'*

The amount J of points $\vec{\xi}_j$ in the source map fits the second definition of resolution, and is entirely up to the researcher in question to determine. Usually, the number of points J is the result of a trade-off between clarity of post-processed results and computation time required.

However, some conditions apply, which are explained later in this section. Whereas the second definition of resolution is almost entirely dependent on the priorities of the researcher during post-processing of data, the first definition is related to the microphone distribution with which this data is initially obtained. The ability to distinguish between two or more sources positioned closely together is of paramount importance in acoustic analysis, since a group of sources misrepresented as one can lead to false conclusions on the location and strength of those sources. The relation between microphone placement and the ability to distinguish between closely positioned sources is described by the Rayleigh Criterion[5], as shown in Equation 2.68.

$$\sin(\theta_r) = 1.22\frac{\lambda}{d} \text{ (For circular apertures)} \tag{2.68}$$

Here, d is the circular aperture of the array, whereas θ_r indicates the angular resolution. The smaller the value of θ_r, the smaller the distance between two sources for which they can still be separated, and therefore a higher resolution for a given frequency can be achieved as the circular aperture goes up.

Figure 2.8 shows the practical implications of the spatial resolution obtained from Equation 2.68. The value of Δl directly represents the theoretical minimal distance between two closely spaced sources where they can still be identified separately. The distance r from the array to the source and the circular aperture of the array are therefore the two main factors of influence on the spatial resolution for beamforming at a given frequency.

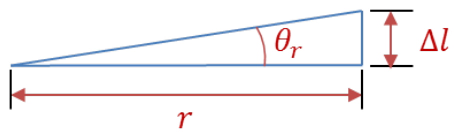

Figure 2.8: Angular resolution

The value of Δl in Figure 2.8 can be calculated as:

$$\Delta l = r \tan(\theta_r) \tag{2.69}$$

The highest resolution can be obtained by defining a source map oriented perpendicular to the center of the acoustic array, with the expected source location is in its center. This yields both the smallest distance r between the array and the source map, and the largest effective circular aperture d. For experiment setups, this means that the highest resolution can be obtained when the point or region of interest is aligned with and perpendicular to the center of the array.

The images in Figures 2.9 through 2.14 demonstrate the challenge of resolving sound sources accurately. These images are obtained using a simulation for two tonal sound sources placed at a distance d from one another. The coherent sound sources emit a 2000 Hz tone at 100 dB SPL, and are modeled at separation distances of 0.56 (Figures 2.9, 2.10, 2.13 and 2.14) and 0.28 (Figures 2.11 and 2.12) meters. A source map of 2 by 2 meters is obtained with a generic random microphone distribution across an array of 2 by 2 meters, positioned at 2.5 meters away from the sources, oriented perpendicular to the source map. The source map is obtained for reference distance $r_{ref} = 1$. In Figures 2.9 and 2.10, the amount of points J in the source map is set to 225, granting a distribution of 15 in x-direction and 15 in y-direction. For Figures 2.11 through 2.14, the resolution is set to 10000 points, again with equal distribution over x and y, resulting in a grid of 100 by 100 points.

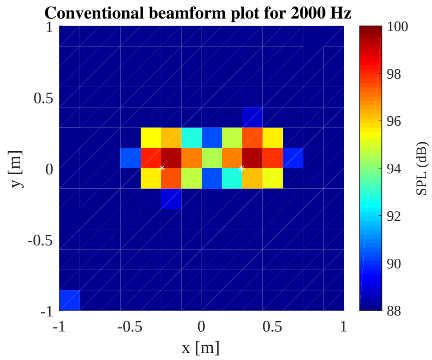

Figure 2.9: Insufficient grid points - source map

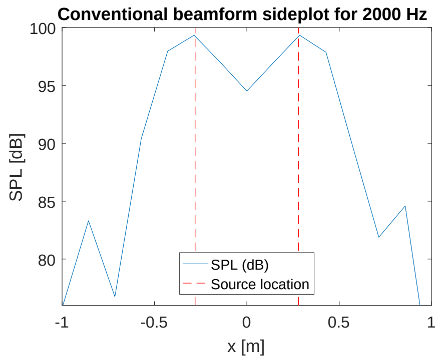

Figure 2.10: Insufficient grid points - sideplot

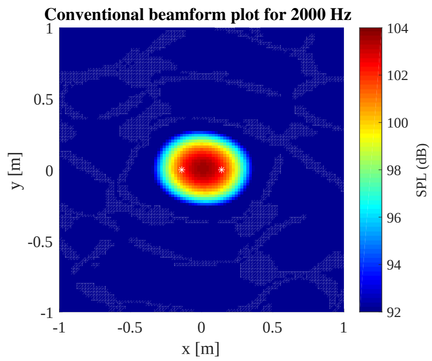

Figure 2.11: Insufficient separation distance - source map

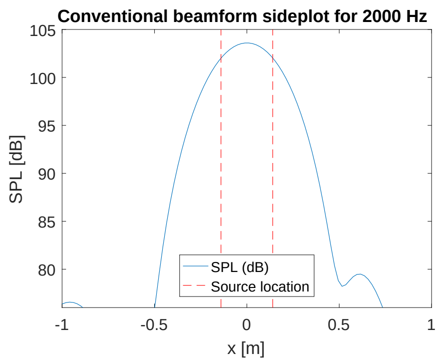

Figure 2.12: Insufficient separation distance - sideplot

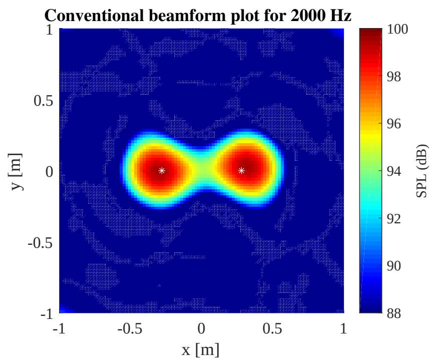

Figure 2.13: Resolved sources - source map

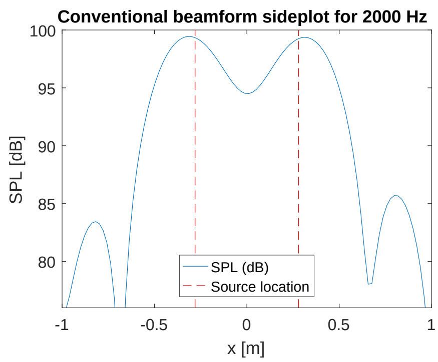

Figure 2.14: Resolved sources - sideplot

As the first two images demonstrate, a low amount J of source map points results in unclear results, and is only beneficial if computation time plays a large role. The simulation parameters are exactly the same as the ones used to generate Figures 2.13 and 2.14, but due to the low amount of source map points the clarity of the results is much lower. The ability to resolve sources separated by a distance Δl only holds if the separation distance of points in the source map is equal to or lower than Δl. This indicates a suggested lower bound for the amount of points J for a source map of a given region at a given distance r away from the array.

Figures 2.11 through 2.14 show the effect of the Rayleigh limit on the ability to resolve two closely spaced sources. As stated before, the separation distance at which two sources are resolvable is dictated mainly by the aperture of the array. Therefore, to obtain the maximum spatial resolution, a circular array with the highest attainable aperture diameter should be used, as shown by Equation 2.68, to enable resolvance of closely spaced sources over a large range of frequencies.

The microphone distribution not only influences the Rayleigh limit, but also influences the presence, positions and strength of side lobes. Side lobes can originate from the core concept of beamforming, which is to combine the acquired data from multiple microphones to obtain a source map of the region of interest by means of a minimization problem. This minimization problem will (for a finite number of microphones) inevitably result in a remainder and therefore an error in the estimation of complex amplitude a, which is represented in the autopower matrix as a side lobe. Another cause of side lobes can be found in interference caused by the presence of reflective and/or refractive surfaces, or noise sources outside the object and region of interest. Whereas the latter can be minimized by improving the test setup and environment in wind tunnel test conditions, the former follows from the basics of beamforming, and must be dealt with using a different approach. One option is the optimization of microphone distribution to minimize this remainder.

According to the Random Array Theory by Steinberg, the best microphone distribution in terms of side lobe levels and presence is an irregular one, using as many microphones as possible. He states [1] that:

- *The number of array elements is the dominant quantity influencing the level of the peak side lobe*
- *The theoretical average side lobe power level of a random planar array relative to the main lobe is approximately 10 log($\frac{1}{N}$) + 3 dB, where N is the number of sensors in the array*
- *A rule of thumb regarding the peak side lobe level is that it is unlikely to exceed the average by 10 dB*

For a circular array with a uniform microphone distribution, the lowest attainable side lobe level can be determined with a first order Bessel function of the first kind. This function describes an Airy disk point spread function for circular arrays[2][34]. The maximum side lobe level obtained with this function is the minimum obtainable side lobe level using a circular array with uniform microphone distribution, which is 17.57 dB lower than the main lobe. Since the number of array elements (microphones) is limited in practice, this minimum is never attained even under perfect measurement conditions, hence the issue of side lobe presence must be tackled by optimizing the microphone distribution[54][33]. However, using a non-circular microphone distribution decreases the maximum obtainable resolution, since the effective aperture d is lower.

3

Array Design

As the first phase of the project, the design process was initiated by identifying the design objective of the array, taking into account its purpose and usability. This is followed by an introduction to the anechoic room for which the device is destined, elaborating upon its layout and components. Thirdly, identification of requirements and restrictions is performed based on the design objective and the available space and tools. Based on the design objective, requirements and restrictions, an iterative process of array design is initiated revolving around theoretical analysis of design concepts, resulting in the chosen array design. Finally, the Data Acquisition System (DAS) is introduced and discussed, but since this system was predetermined ahead of the start of this project, no iterative process in optimizing its configuration is required.

3.1. Structural design considerations

This section introduces and explains the main design objectives that were taken into account throughout the design process, as well as their significance and potential influence on the final design choice.

The main objectives of the array structure were determined to be as follows:

- Practicality
- Acoustic Performance
- Flexibility

The first point is quite self-explanatory; the array must not be overly complex in use. This objective is twofold, applicable for both the practical (tangible) use of the array as well as controlling the system through software. The actual structural setup (i.e. placing the microphones) should be a straightforward, simple and short process, ideally without the requirement of additional tools. Controlling the system should be straightforward and simple, whilst also enabling the user to specify and alter all necessary parameters (e.g. sampling frequency and sampling duration).

The second objective is equally clear. If the chosen structure influences the recorded data in such a way that the source map representation becomes altered (e.g. by means of excessive reflections, resonance or noise), a different design must be considered. The perfect structure would allow the microphones to pick up a clear and unobstructed signal from the source, and does not alter or influence the signal in any way. This may conflict with the practicality objective, in which case a trade-off must be performed. As indicated in Section 2.6, using the maximum aperture possible is an important factor in attaining a higher maximal resolution. However, a large array may put a strain on its practicality requirement, and potentially on its acoustic performance (depending on the chosen final design). This type of trade-off is a continuous process throughout the design process described in this section.

Flexibility mainly pertains to reconfigurability of the microphone layout. This means that the placement and (re-)moving of microphones should be a simple process, as mentioned under the practicality objective, but there should also be a large amount of possible microphone positions to choose from, granting the user the largest possible freedom in designing the configuration that best fits their experiment.

A fourth objective, minor in comparison to the aforementioned trinity, is coupled to time constraints. The first experiments to be performed in the wind tunnel had already been scheduled ahead of the start of this project, and would ideally make use of this new array. This drives the design of the array in such a way that lengthy production times may cause the design option to be discarded. The focus is therefore shifted slightly to readily available solutions and industrial standard components.

The starting point of the design phase consisted of looking at existing structures, both from the ANCE section as well as acoustic array industry examples. Images 3.1a through 3.1c show a selection of potential array designs that were taken into initial consideration. Not only do the shapes differ between these examples, the possible distribution of the microphones and the total size of the array is different for each as well.

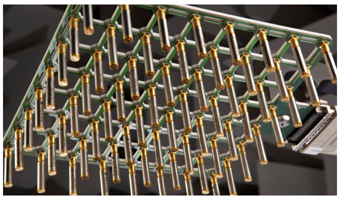

(a) Square distribution array

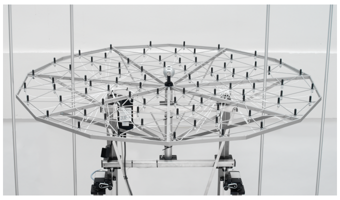

(b) Circular distribution array

(c) Spherical distribution array

Figure 3.1: Array examples from industry[7]

The first and third structural requirements, **Practicality** and **Flexibility**, would make the first array example a very viable candidate, since its grid structure would allow for precise and simple microphone positioning, and the amount of open space within the structure would ensure less reflections than from a solid structure of the same layout. With a sufficiently large structure of this type, the same microphone layout as used in the second example could even be replicated. Therefore, the example shown in Figure 3.1a was used as a basis to come up with the first design.

The microphones in the aforementioned example are mounted straight onto the structure, in which all electronic pathways necessary for data recording are integrated. This would be very convenient, but such a structure is very costly to make, especially on a large scale as stipulated by the maximum aperture request of the flexibility requirement. Therefore, the idea of integrating the data link into the array structure was discarded for the first array prototype. Instead, the focus was put on a design which would offer the maximum amount of microphone positions with the maximum aperture that would still fit inside the wind tunnel, and would allow to connect the microphones to the data acquisition system through a set of cables.

The design featured in Figure 3.1c deviates significantly from the other two. Not only is the array a solid structure, it is also non-planar. The full integration of the microphones into its spherical shape ensure the impact of reflections from the array on the measurements to be very low (if any), and the inclusion of cameras in the array allows for clarification of the measured noise by showing it on a visual representation of the surroundings.

The array setup in Figure 3.2 shows another possibility for mounting microphones in an array. The ability to slide and aim microphones in a multitude of directions theoretically allows for many more different microphone configurations than the fixed positioning systems shown before. However, as shown in Section 2.2, knowledge on the exact position of the microphones with respect to the source map is vital to formulate an accurate set of steering vectors. A fixed position system grants this inherently, whereas determining the exact position of the microphone with respect to the source is much more difficult with a free positioning system, therefore violating the practicality objective. A fixed position system was therefore chosen for the following design phases.

Figure 3.2: Free position array

3.2. Anechoic test chamber

The anechoic chamber housing the open wind tunnel test section was (partially) under construction throughout most of the duration of this project. This was cause for some unclarity and delays, but the main purpose and configuration of the room was known up to a degree, deemed sufficient to begin the design phase.

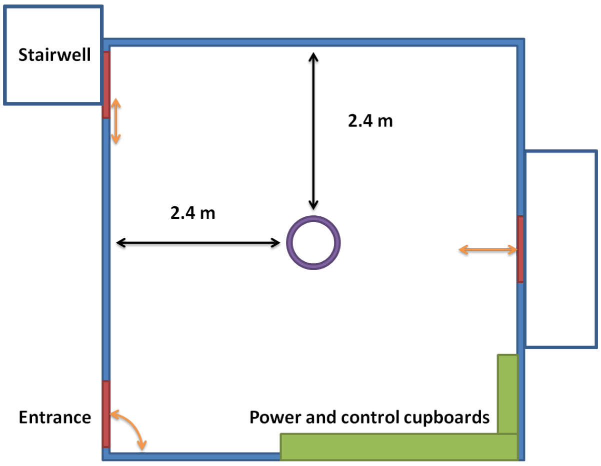

Figure 3.3: Anechoic test chamber layout

The anechoic test chamber is a two-tiered square room, with one point of entry and two adjacent rooms. The test section is situated on the first of these two floors, hence the array will also be placed here. Figure 3.3 shows a floor plan of the room, indicating three doors in red, each opening in a different way as indicated by the orange arrows. The tunnel inflow section is indicated by the purple circle in the center of the room. The purpose of the small room behind the right door was initially the housing of a PIV laser system. However, this was changed due to cooling constraints. It is left empty for now, but might be occupied in the future, which has consequences discussed later (Section 4.1). The distance from each wall to the tunnel inflow opening was measured to be an average of 2.2 meters.

The flow enters the room through a circular opening, at a height of 0.33 meters from the floor. A nozzle must be mounted to this opening for experiments, where the choice of type of nozzle exit is left to the tunnel user. Circular, square and rectangular exit shapes are examples of available nozzles. The height of these nozzles differs per type. The object under investigation must be placed in the flow at some point above the nozzle exit, where the dimensions of the object dictate the spacing between the nozzle exit and the center of the object. For this design process, the average test section height was estimated at 1.5 meters from the ground, to be taken into account when designing the array such that the center of the array is aligned with the test setup (see Section 2.6 for an explanation on the importance of this alignment with respect to resolution).

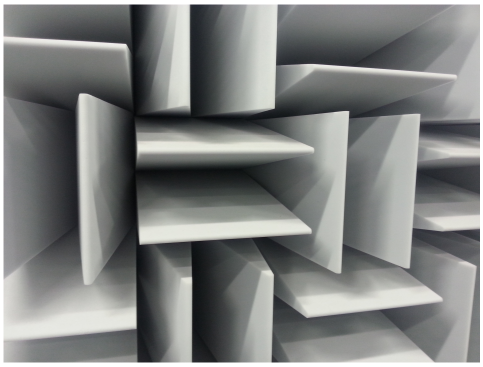

Figure 3.4: Flamex anechoic wall wedge

The walls and ceiling of the test chamber are covered with 50 cm tall Flamex anechoic wedges, rated for damping frequencies of 500 Hz and above. The floor and some ceiling sections are covered with 10 cm thick Flamex panels, providing a reduction in reflected sound energy. However, these panels do not cancel out the incident sound waves as effectively as the wedges, and not all surfaces of the tunnel are covered. The power and control cupboards, for example, are left untouched, as well as a concrete strip of wall next to the test chamber entrance. To allow the airflow to diffuse, the first floor ceiling is not closed, allowing air and noise to propagate to the upper floor. The upper floor has not undergone any form of acoustic treatment, nor have the stairwell and the room opposite the entrance. Additionally, incomplete covering of the entrance allows significant transmission of sound from the adjacent hallway into the test chamber. Since this hallway is the main route to the store room, toilets, and bike shed, noise in the form of speech or doors slamming shut is not uncommon. Since there is no system in place to prohibit this from happening, this must be taken into account when recording and post-processing measurement data.

3.3. Array restrictions and requirements

After initial orientation, the following step in the design phase is identifying the requirements and restrictions of the to-be-designed object, to limit the design space. For this project, the initial restrictions are imposed by physical limits such as microphone size and available space in the chamber for which the array is being designed. Requirements, on the other hand, are inherited from the purpose of the array, i.e. the properties of the array must be such that acoustic beamforming can be performed in an optimal way.

3.3.1. Design restrictions

As established before, the newly reconfigured vertical wind tunnel at the Delft University of Technology features an anechoic test section. The dimensions of the room restrict the maximum amount of space the array can occupy. During the design phase, the final layout of the room was not determined (e.g. the floor would initially be raised to incorporate more adequate sound damping structures, and additional equipment would be placed), which lead to a safety factor being included in both maximum height and width of the array, such that the array would still fit in an altered environment. The final maximal dimensions of the array were set at 2.5 meters in height, 3 meters in width, and 1.5 meters in depth, leaving sufficient space to move and work around the array.

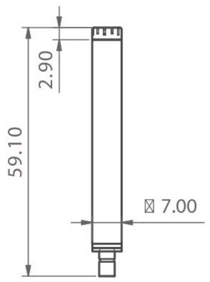

Figure 3.5: GRAS 40PH Array Microphones (in mm)

The microphones to be used with this new array were chosen and purchased before the start of this thesis project, a total of 64 GRAS 40PH array microphones[20]. Therefore, their dimensions impose another set of restrictions on the minimal dimensions of the array. Figure 3.5 shows the dimensions of these microphones. The microphones are connected to a data acquisition system (introduced and discussed in Section 3.5) by means of individual cables, with a length of 10 meters and a maximum diameter of 6 mm at the microphone connector. Since this diameter is less than the microphone diameter, the microphones dictate the minimum space required between two individual microphone mounting points.

The anechoic vertical wind tunnel test chamber, for which this array is designed, is located on the second floor of the Low Speed Windtunnel Laboratory. Since the array is not intended as a permanent fixture in the test chamber[1], it must be transportable and storable within the building. Since this part of the building is still undergoing changes in layout in terms of offices and workspace for students, the final storage location is undetermined at this time. The main storage facility of the building is located on the ground floor.

The maximum dimensions of the array are therefore also restricted by the maximum dimensions of doors, elevators and stairwells between the test section and the storage facility. The elevator is the most practical means of transportation, allowing for objects measuring a maximum 2.20 by 2.0 by 0.2 (Length x Width x Thickness) meters, and is therefore the main restrictive factor size-wise. The alternative means of transporting the array downstairs, using the stairwell, yields similar restrictions to the maximum dimensions due to the width and height of the stairwell at its narrowest location.

[1] Mainly due to the fact that construction projects and improvements were still being performed on the tunnel throughout the duration of this project

3.3.2. Design requirements

As established in Section 2.6, the performance of any microphone distribution for use in beamforming is measured by two main factors; main lobe width and side lobe presence. Optimal performance for the first can be obtained by having a distribution with a large aperture, i.e. an as large as possible array. The latter is more difficult to achieve, since the best microphone distribution is determined mainly by the experiment parameters, such as the frequency range of interest and the expected source location and shape. Because of this, having a reconfigurable array in terms of microphone distribution is an attractive way to allow the fixture of many different microphone configurations, thereby allowing the user to tune the array for a specific objective, as discussed in Section 3.1.

In Section 2.5, the reflection and refraction behavior of sound waves is explained. The main factors determining the reflection index of a material are the speed of sound in that medium, and the density of that medium. This reflected wave can cause interference with the incoming wave in the near field, in both a constructive or destructive manner[50], resulting in an error in measured pressure. The significance of this offset depends on both the reflection coefficient and the incidence angle of the incoming wave. Since the incidence angle per microphone depends on its location with respect to the source map, this is an impractical property to attempt to optimize. The reflection coefficient however is fully dependent on the properties of the material from which this wave is reflected. The choice of material used for the array structure must therefore be made with favorable reflectivity properties in mind, which is indicated by the density ρ_2 of and speed of sound c_2 through the chosen material (see Equations 2.63, 2.64, and 2.66). Favorable performance is obtained when both these properties are low. The speed of sound through a medium is determined with

$$c_2 = \sqrt{\frac{E_2}{\rho_2}}, \tag{3.1}$$

where E_2 is the Young's modulus of the chosen material, indicating stiffness. Combining this equation with Equation 2.64, the optimal material choice for the array would therefore be of low stiffness and low density. However, constructing something sizable that is structurally sound out of a material with low stiffness may require additional stiffening elements. A stiff material with a low density (i.e. a high specific Young's modulus) might be a better option, to attain both structural stiffness and acceptable reflectivity performance.

To determine appropriate limits for array performance assessment, the purpose of the array and the wind tunnel must be clarified. Since this anechoic test section is destined to be used for wind turbine blade analysis, this field was investigated for similar projects in an attempt to identify the frequency range of interest, as well as an indication of expected sound pressure levels during such experiments. A number of articles was analyzed, which included a wealth of information on the given subjects. The main frequency range of interest was identified to be 750-8000 Hz[8][37], where the lower limit is mostly dictated by the anechoic qualities of the room in which the experiment takes place. The total estimated sound pressure level shows to be highly dependent on the wind velocity at which the measurement takes place, reaching a maximum of 120 dB in the measurements discussed by Cho[10], with an average of 80 dB according to Cho and Fischer[14]. Since the upper limit of the microphones in terms of measurable sound pressure lies at 135 dB, the given powers are well within the maximum achievable limits. The frequency range of 750 to 8000 Hz is set as the goal within which to reach optimal performance. Since the tunnel is designed to provide anechoic performance above 500 Hz, this frequency range can even be extended to 500-8000 Hz.

3.4. Design process

The first design concept of a planar, fixed position array is shown in Figure 3.6[2]. This design allows for straightforward microphone placement in circular slots that support the microphones over their entire length, to ensure all microphones are oriented perpendicular to the source map. This concept features a large amount of possible microphone positions, thereby fulfilling the flexibility objective. However, this concept has a number of downsides; depending on the chosen material, the mass of such a large structure can be quite significant, impacting the practicality objective. Additionally, the long slots are essentially open-ended tubes, which can house standing waves when perturbed by airflow. Considering the application of this array in an open wind tunnel test section, this situation is not unthinkable, which means that such a design might interfere with measurements due to the aforementioned resonance phenomenon.

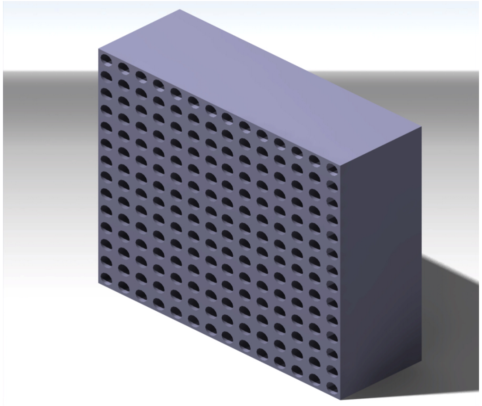

Figure 3.6: First array concept (200 x 200 x 70 mm)

The base frequency of a standing wave in a tube is proportional to the length L of that tube, by

$$f = \frac{c}{2L}. \tag{3.2}$$

For the proposed design, the base resonance frequency can be calculated to be 2450 Hz (based on a value for c of 343 m/s), which is within the frequency range of interest of 500-8000 Hz. This potential issue was solved in the following concept.

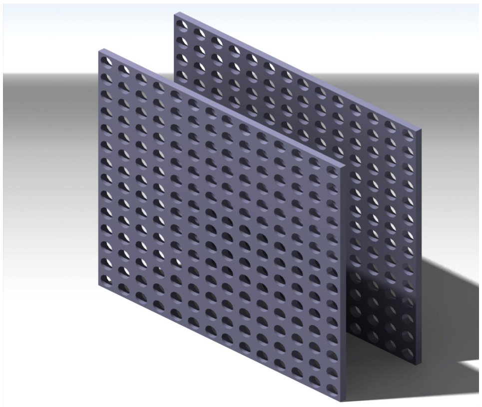

Figure 3.7: Second array concept (200 x 200 x 70 mm)

The same effective microphone support as obtained with the first concept can be achieved by removing the entire midsection, resulting in an array that consists of a front and a back plate. This removes the chance of standing waves inducing resonance, potentially improving array acoustic performance. Additionally, the total mass of the array is lowered significantly compared to the first concept, regardless of the material used. However, such an array will require a frame to keep the front and back plate equidistant and parallel over the full span of the array, adding additional components and mass to the system. Furthermore, microphone positioning is more complicated with this concept; not only must the alignment of the front and back plate be perfect, the array operator has to aim very precisely whilst (re-)configuring the microphone layout. This was not an issue in the first concept, where the microphone was automatically aligned due to the array shape.

Combining the benefits of the first and second concepts led to the third and final concept. This concept consists of a single perforated plate, along with a method to provide sufficient microphone support.

[2]The dimensions of the array concepts are given in the figure caption. The microphone slots in the full-size (2.5 by 3 meters) array would be indiscernible in print, hence only a small part of the array concept is shown

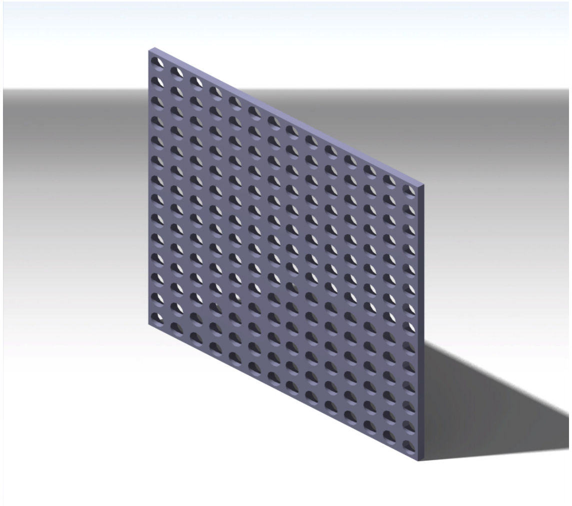

Figure 3.8: Third array concept (200 x 200 x 70 mm)

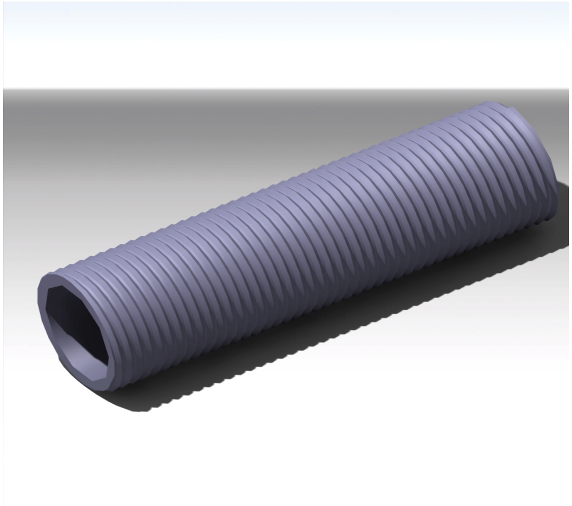

Figure 3.9: Microphone holder

A single thin perforated plate would not provide sufficient directional support to mount microphones. However, this support can be achieved without the added weight nor the risk of standing wave resonance of the first concept, by means of using a microphone holder. A short tube with threading on the outside can be mounted to the array on both sides with regular hex nuts, and provide sufficient stability to the microphone, holding it firmly in place. This concept is shown in Figure 3.10. If the inner diameter of said tube is such that the microphone has a snug fit, there is no space left for a standing wave to develop in. As long as no empty holders are mounted to the array, the potentially harmful resonance effects of the first design are negated.

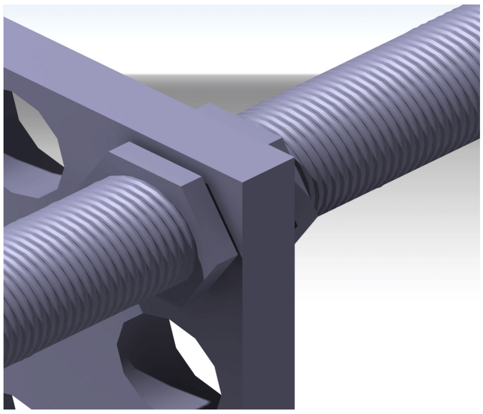

Figure 3.10: Microphone holder mounted

The use of perforated plates is not uncommon in acoustics, albeit for a different purpose. Metal plates with such a perforation pattern are often featured in acoustic dampers because of their high acoustic permeability, in conjunction with some form of sound absorbent material[56]. A study on the acoustic permeability of perforated plates was carried out by Phong and Papamoschou[46][45], leading to the creation of a transmission loss estimation model. This model showed a large improvement on earlier models (e.g. the model suggested by Chen[9]), and estimates the transmission loss through perforated plates by treating each perforation as a duct with a single contraction chamber with diameter d and length l.

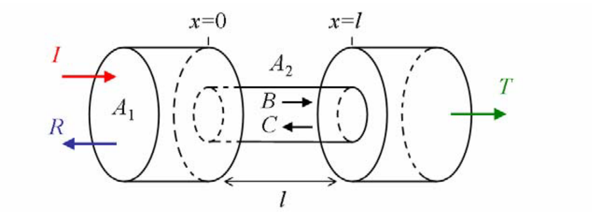

Figure 3.11: Contraction chamber used for one-dimensional modeling of sound transmission in Phong and Papamoschou's model

Starting with the assumption that the wavelength of sound is larger than the contraction diameter, the pressures in the domain can be expressed as

$$\begin{aligned} p' &= Ie^{i\omega(t-x/c)} + Re^{i\omega(t+xc)} && ,x<0 \\ p' &= Be^{i\omega(t-x/c)} + Ce^{i\omega(t+xc)} && ,0 \le x \le l \\ p' &= Te^{i\omega(t-x/c)} && ,x>l. \end{aligned} \tag{3.3}$$

I, R and T are the amplitudes of the incident, reflected and transmitted waves, respectively. B and C indicate the amplitudes of the pressure waves inside the contraction. The continuity condition on mass flux means that

$$\rho_0 A_1 u_1 = \rho_0 A_2 u_2. \tag{3.4}$$

The energy flux continuity condition stipulates that

$$A_1 p_1' u_1 = A_2 p_2' u_2. \tag{3.5}$$

The combination of these two equations shows that $p_1' = p_2'$ at the contraction interface as well as at the expansion ($x = l$). This yields a set of equations for which R and T can be expressed in terms of I. This results in transmission loss L_t being expressed as

$$L_t = 10\log_{10}\left[1 + \frac{1}{4}\left(\frac{A_1}{A_2} - \frac{A_2}{A_1}\right)^2 \sin^2\left(\frac{\omega l}{c}\right)\right]. \tag{3.6}$$

Now, by expressing plate porosity as $\beta = A_2/A_1$, this reduces to

$$L_t = 10\log_{10}\left[1 + \frac{1}{4}\left(\frac{1}{\beta} - \beta\right)^2 \sin^2(kl)\right]. \tag{3.7}$$

A correction must be applied to account for interactions between the individual perforations. The correction factor ϵ can be calculated as

$$\epsilon = \frac{8}{3\pi\psi(\beta)}. \tag{3.8}$$

The $8/(3\pi)$ term represents the end correction for a single orifice in an infinite plate[27], whereas the $\psi(\beta)$ term is Fok's function[15]. This function describes the acoustic conductivity of an orifice with diameter d within a circular tube of diameter D, as is the case for the perforated plate model shown in Figure 3.11. Now, by using Fok's function, defined as

$$\psi(\beta) = \left(1 - 1.40925\beta^{1/2} + 0.33818\beta^{3/2} + 0.06793\beta^{5/2} - 0.02287\beta^3 + 0.03015\beta^{7/2} - 0.01641\beta^4\right)^{-1}, \tag{3.9}$$

the effective thickness of the plate can be calculated with

$$l_{eff} = l + \epsilon d, \tag{3.10}$$

where d is the hole diameter. Now, Equation 3.7 becomes

$$L_t = 10\log_{10}\left(1 + \frac{1}{4}\left(\frac{1}{\beta} - \beta\right)^2 \sin^2\left[k\left(l + \frac{8d}{3\pi\psi(\beta)}\right)\right]\right) \tag{3.11}$$

The reflection coefficient can now be calculated with the following equation (obtained through manipulation of Equations 3.3 and 3.5):

$$R_\pi = \frac{i\left(\frac{1}{\beta} - \beta\right)\sin\left(kl_{eff}\right)}{2\cos\left(kl_{eff}\right) + i\left(\frac{1}{\beta} + \beta\right)\sin\left(kl_{eff}\right)} \tag{3.12}$$

Phong and Papamoschou's model assumes normal incidence, and was tested only with perforations up to a diameter of 2.6 millimeters. The accuracy of the model estimated transmission loss was proved to be within 1.5 dB of the actual value for a dimensionless hole diameter $0 \le d/\lambda \le 0.75$, for plates with a dimensionless thickness of $0.15 \le l/d \le 1.0$ and plate porosity β (the ratio of perforation size to surrounding material) of $0.22 \le \beta \le 0.48$. It should therefore be applicable to larger perforations patterns as well (within the given range of dimensionless values), but this has not been tested. Since this model provides the most accurate and up-to-date estimation of transmission loss in perforated plates, it is used for estimating array acoustic performance in this design process. The current model does not include material properties, but can be expanded to account for material porosity by correcting area A_1 accordingly.

As with the second design concept, a frame will be required for structural support. As explained in Section 2.6, alignment of the center of the array with the test section is important to be able to resolve closely spaced sources. Based on the room dimensions, as discussed in Section 3.3.1, the maximum height of the array is 2.5 meters, and the maximum width 3 meters. Since the nozzle is situated in the center of the room with respect to the horizon, aligning the center in terms of width is no issue. Height-wise alignment however imposes restrictions on the array size. Since the test section height was estimated at 1.5 meters from the floor, this means the array can extend up to 1 meter above the test section. Due to symmetry required for center alignment, this means the array must also extend to 1 meter below the test section, measuring a total of 2 meters height-wise and 3 meters span-wise. The frame must therefore not only support the array structurally, but also lift it 0.5 meters off the floor. Based on these requirements, the frame design as shown in Figure 3.12 was made, measuring a total of 2.5 by 3.0 meters.

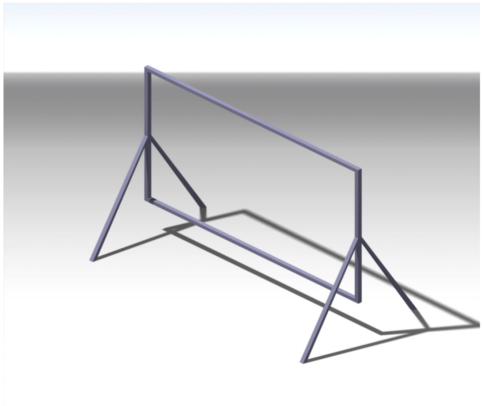

Figure 3.12: Frame concept

Summarizing, the final suggested design concept consists of a perforated plate, measuring 2 by 3 meters, mounted to an array frame for structural support. The microphones are mounted to the plate by means of a microphone holder, which supports the microphone and ensures all microphones are pointing perpendicular to the source map region. The holders are designed as tubes with threading on the outside, with an inner diameter equal to the microphone diameter to ensure a precise fit. The outer diameter shall be no greater than the diameter of the plate perforation.

According to the model suggested by Phong and Papamoschou, better performance can be obtained either by increasing the perforation diameter or decreasing the spacing between perforations, both effectively increasing plate porosity. When choosing the perforation pattern, this ratio must be optimized, whilst also keeping the maximum number of perforations for the flexibility objective in mind. Three different perforation shapes were compared, in two different layouts, as shown in Figures 3.13 and 3.14. A spacing distance of 2 millimeters was chosen for all distributions, for a perforation diameter of 10 millimeters (which is required to allow sufficient space for both the holder housing the microphone), for a surface of 2 by 3 meters.

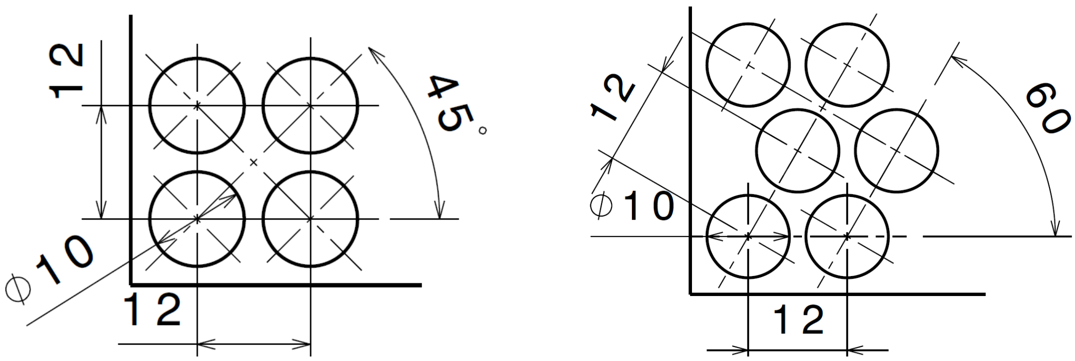

(a) Circular distribution - grid (dimensions in mm)

(b) Circular distribution - stacked (dimensions in mm)

Figure 3.13: Circular distribution options

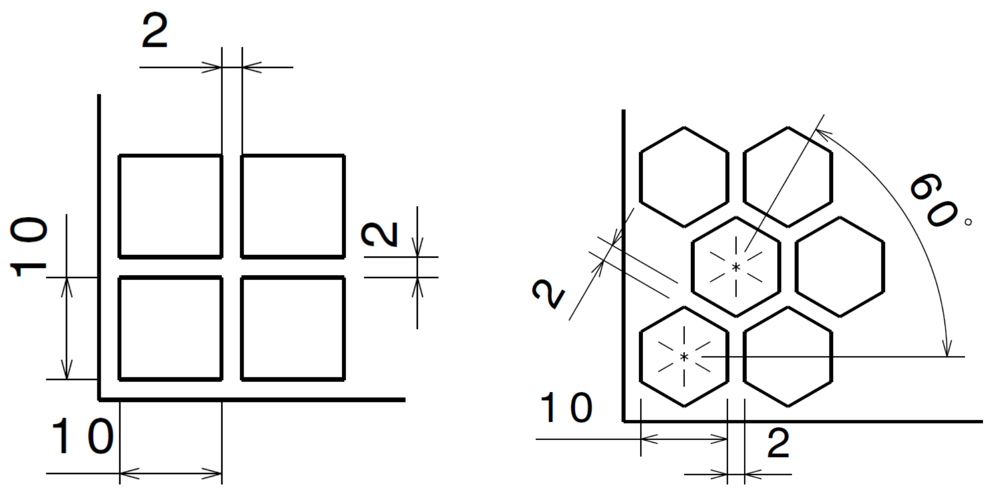

(a) Square distribution - grid (dimensions in mm)

(b) Hexagonal distribution - stacked (dimensions in mm)

Figure 3.14: Square and hexagonal distribution options

Table 3.1: Pattern comparison for a 2 x 3 meter surface

Slot shape	**Distribution pattern**	**Total amount of perforations**	**Total open area** (m^2)
Round	Grid (Figure 3.13a)	41334	3.2464
Round	Stacked (Figure 3.13b)	47808	3.7548
Square	Grid (Figure 3.14a)	41334	4.1334
Hexagonal	Stacked (Figure 3.14b)	47808	4.1403

A hexagonal perforation pattern would be optimal in both open area and amount of perforations. The square distribution is a close second in amount of open area, but features about 14% less perforations than the hexagonal counterpart. Based on this knowledge, the optimal array would consist of a thin perforated plate with a hexagonal perforation pattern, preferably made of a stiff but porous material to ensure maximal permeability. For practical reasons as well as physical limitations in the wind tunnel building, the maximum size of any component was restricted to 2 by 2.2 meters in height and width, and 20 centimeters in depth (see Section 3.3.1). A practical solution to this restriction is to alter the design such that the perforated plate and the frame consist of multiple components, introducing a degree of modularity to the design.

At this point in the project, the AWEP (Aerodynamics, Wind Energy, Flight Performance & Propulsion) department stressed that the time frame within which the array should be finished was only a matter of weeks. Taking into account time and cost required for production, a number of options was evaluated that would allow meeting this deadline. The most common industrial practices for producing perforated plates is by means of punching holes using a press. Laser or water jet cutting would also be possible, but much more expensive, and the production time would be significantly longer than the alternative. 3D-printing was also considered, but this method featured even longer production times and immense cost for an object on this scale. However, standard plate punching techniques do not allow for hexagonal perforations, whereas cutting or printing the system can be done for any perforation pattern. A square grid pattern was possible using punching as the manufacturing method, and considering the significant cost and time benefits, this distribution manufactured by means of punching was chosen.

A number of manufacturers was contacted, and the choice of material and plate size as well as thickness was limited per company. A common factor is that, to guarantee sufficient stiffness, the spacing between two perforations must be at least half the diameter of a perforation, which in this case is 5 millimeters. This is larger than the 2 millimeters initially estimated, but was unavoidable unless a different production method was used, resulting in higher cost and longer production times.

The available materials were aluminum, steel, and stainless steel, and the maximum size per plate was 2000 by 1000 by 3 millimeters. This fit perfectly within the given size parameters, and three of such plates could be used to make up the entire array. The steel variant of these plates was least costly and was available quickest, and therefore three of these plates were purchased. The high density of steel makes it less favorable in terms of reflective behavior, but the high plate porosity would counteract this according to the Phong and Papamoschou model.

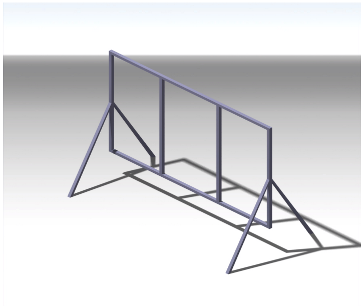

Figure 3.15: Frame concept - additional stiffening elements

The construction of the frame was discussed with DEMO (Electrotechnical and Mechanical Development Support Staff, DUT), since their expertise in the development, design and creation of such test setups was required. For sufficient stiffness, they suggested additional stiffening elements between the top and bottom spars of the array, to provide each plate with sufficient structural integrity as well as smooth the connection between each of the three plates. This adapted design is shown in Figure 3.15.

With the given final plate dimensions, the properties as given in Table 3.1 can be recalculated, resulting in Table 3.2 for the entire array

Table 3.2: Pattern comparison for a 2 x 3 meter surface

Slot shape	**Distribution pattern**	**Total amount of perforations**	**Total open area** (m^2)
Square	Grid (Figure 3.14a)	25740	2.5740

This results in a plate porosity of 43% (2.5740/6), and the according Phong and Papamoschou model estimated reflection coefficient is given in Figure 3.16. Since the given upper limit of the Phong and Papamoschou model is dictated by the dimensionless hole diameter $d/\lambda = 0.75$, the maximum frequency for which the Phong and Papamoschou prediction model can be used with the chosen perforation pattern can be calculated by

$$f_{Phong-limit} = \frac{c}{0.01\sqrt{2}/0.75}, \tag{3.13}$$

which results in an upper frequency limit of 18.1 kHz, indicated in the figure by the red dashed line. For the given frequency range objective of 500-8000 Hz, a very favorable reflection coefficient of less than 0.13 is estimated using the Phong and Papamoschou model, as indicated by the dashed black lines, suggesting good acoustic performance using this type of array.

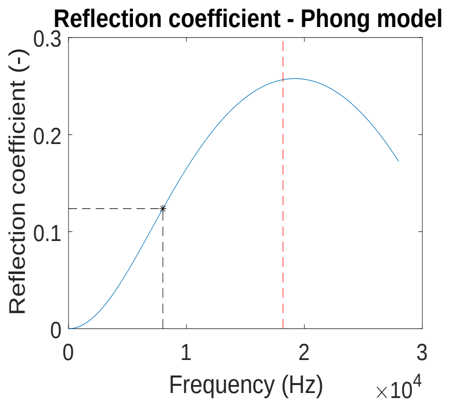

Figure 3.16: Reflection coefficient as estimated by the Phong and Papamoschou model

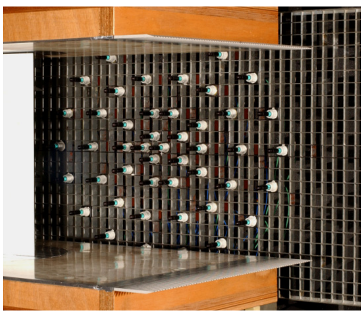

Figure 3.17: NLR acoustic array[37]

The final chosen array design shows some similarity to one used at NLR, as shown in Figure 3.17. The main differences lie in the size of the microphones used and the plate porosity of the array. The NLR-array uses larger microphones, hence increasing the required perforation size and therefor obtaining a more favorable plate porosity, but attaining less microphone positions per area. Since the microphones used for this project are smaller, and objectives established in Section 3.1 dictate a balance between available microphone positions and plate porosity, the current array design features more microphone positions at the cost of a lower plate porosity.

3.5. Data acquisition system (DAS)

The second part required to make up the whole array system is the data acquisition system. Along with the microphones, the data acquisition system was also obtained in advance. The system consists of the components as listed in Table 3.3

Table 3.3: Array data acquisition system system components

#	Component	Type	Quantity
1	NI PXIe-1085	18 slot PXI-chassis[39]	1
2	NI PXIe-4499	Sound and vibration data acquisition modules[40]	5
3	NI PXIe-8370	Remote control module[42]	1
4	NI RMC-8354	Rackmount controller[41]	1
5	GRAS 40PH	Free-field array microphones[20]	64
6	RG 174 AU	50 ohm coaxial cables (MIL-C-17F), each 10 meters in length	64
7	NI SHB4X-8BNC	Infiniband to BNC conversion cables, 8 channels per cable[43]	8

The chassis (#1) contains all measurement modules (#2), as well as the remote control module (#3). This allows the modules to be employed through the rackmount controller (#4), which features a Windows™7 operating system. The microphones (#5) are connected to the sound modules by means of the coaxial cables (#6), which are bundled and connected to each module by means of two conversion cables (#7) per module, resulting in a total of 16 microphones connected per module. This means that one module is left empty, which can be used for future expansion.

Both the rackmount controller and the PXI-chassis are designed to be mounted in a standard 19-inch server rack. A server rack was suggested based on a number of criteria, which are

1. Sufficient headroom, i.e. space between different components, mainly for ventilation and cable routing
2. Sufficient depth, i.e. space behind different components, mainly for ventilation and cable routing
3. Sufficient ventilation capability, i.e. means to (actively or passively) expel hot air and take in cool air
4. Full enclosure, to reduce fan noise

Whereas the first two criteria are simply to ensure that the system is built into an enclosure that is actually capable (sizewise) of housing the system, the fourth criterion was based on initial tests with the system. Before mounting it into a fixed structure, the separate components were laid out and connected to get acquainted with the different system components, as well as to identify potential issues. Three large potential weaknesses were identified (discussed in Section 4.2), one of which was the large amount of fan noise generated by both the controller and the PXI-chassis. When restricted to the lowest configurable fan speed setting for both machines, the amount of noise was still significant. Full enclosure would therefore be a good solution to reduce this system noise, which might otherwise interfere with acoustic measurements.

Since the DAS was already decided upon ahead of this project, no iterative process was required in designing and choosing the optimal configuration.

4

Array Creation

This chapter elaborates on the creation phase of the project. The first section discusses the creation of the array, which was mainly executed by DEMO. The second section introduces the DAS creation process, including the process of constructing and placing the array optimally as well as an explanation of the software required to use it effectively. The resulting acoustic array system is shown and discussed in the third section. A manual on the suggested use of the array is available, to aid in the productive employment of the system.

4.1. Array creation

Since personal knowledge in the field of manufacturing large metal structures was limited, the available knowhow and skill of DEMO was employed for the creation of the array. Since DEMO had been incorporated as advisors during the design phase, familiarity with the design had been previously established. Discussing the purpose and required properties of the array in terms of modularity, size and structure was therefore quickly and efficiently handled. The creation of the array took three weeks, and the final system consisted of a frame and three perforated plates, which can be configured as a two-plate system (2 x 2 meters) or a three-plate system (2 x 3 meters). Figure 4.1 shows the size of the array, as well as the porosity of the plates used. The supporting legs are not included in this figure.

Figure 4.1: Final array - 3 x 2 configuration

The array was taken apart, transported, and reconstructed in the wind tunnel test chamber. Since the chamber was still undergoing construction, the array was configured in the 2 by 2 meter setup rather than the 2 by 3 meter system, to allow more space for maneuvering of construction material and personnel. This complete setup in the wind tunnel is shown in Figure 4.2, including the supporting legs (the A-profiles on either end of the array). This system consists of two supports (A-profile), two frame ends (C-profile), and two perforated plates. The remaining components are a supporting T-profile (see Figure 4.5) and another perforated plate, to be mounted between the two existing plates if the full 2 by 3 meter setup is required.

Figure 4.2: Final array - 2 x 2 configuration

The placement of the array in the wind tunnel anechoic test chamber was restricted by a number of causes. Using the layout provided in Figure 3.3 as a reference, the door opposite the entrance is mounted onto a cart. It can only be opened by moving the cart in a straight line away from the wall (as indicated by the orange arrow), and this room must remain accessible. Placing the array against this wall would prohibit that, and was therefore not practical. In terms of accessibility, the power and control cupboards need to remain accessible as well, so placing the array near these was also not allowed. The wall opposite the power and control cupboards was initially allowed, but due to alignment of test setups in the direction parallel to this wall, sound reception would be impeded at this location. Figure 4.3 serves as a clarification: the large side panels of the test setup allow sound to propagate to the front and to the rear of the setup, but not to the sides[1]. In this picture, the power and control cupboard are to the right, and the array is located to the left. As the picture indicates, the array was placed against the wall next to the entrance and the stairwell, since this was the only available location remaining.

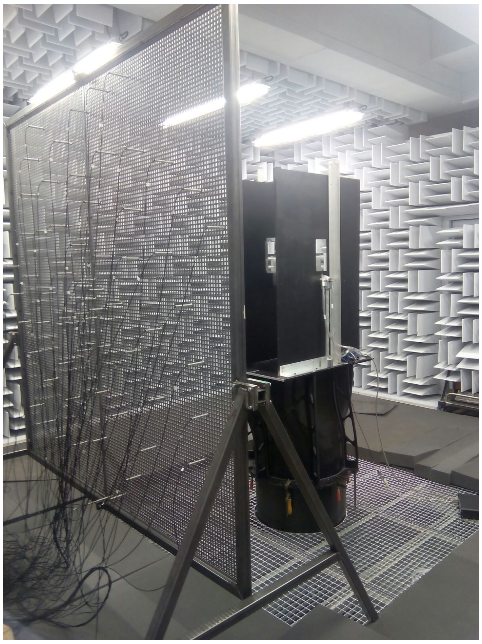

Figure 4.3: Test setup - sound propagation impedance

Microphone holders (i.e. the threaded tubes as shown in Figure 3.9) were manufactured out of hollow threaded rods with an outer diameter of 10 millimeters and an inner diameter of 8 millimeters, with a length of 80 millimeters each. The holders can be mounted to the array with two M10 nuts, as shown in Figure 3.10. 80 of such holders were purchased, along with 160 nuts, to allow for additional microphones to be added to the system, as well as to have spares in case of mis-fabrication or loss. Figure 4.4 shows one such holder containing a microphone. This particular holder was shortened to 40 millimeters, to allow visibility of the microphone within the hollow tube.

To streamline the placement of microphones within the array, grid lines are marked on the array, with a line spacing of 10 grid points.

Figure 4.4: Microphone holder

Figure 4.5: T-profile support for 3x2 configuration

.

[1]The test setups must be oriented in this direction to align the flow with the diffuser mounted above the test chamber

4.2. Data acquisition system creation

The components and requirements of the data acquisition system (DAS) have been discussed in Section 3.5. Since the physical components of the DAS are pre-configured and pre-built, the hardware construction phase of the DAS mainly consisted of the assembly of existing components. The second part required for employing the DAS is the creation of software for data acquisition.

4.2.1. DAS construction, placement and control

As indicated in the DAS requirements analysis, the fan noise originating from the two main system components is substantial, and a full enclosure was suggested to mitigate the potential influence of this fan noise on the recorded data. However, the ordering and purchase of the enclosure was done without further inclusion of said suggestion, and the final choice (the Samson SRK-21 universal wheeled rack) did not provide sufficient depth, nor was it enclosed on all sides. The fact that a rack of this type had been used before to contain a different system might have been the reason, but the exact motivation for this choice is unknown. Nevertheless, this rack was to be used to house the system. The only option to do so (with the components available at the time) was to fasten the controller only at the front, and placing it at the bottom of the rack to provide sufficient support at the back. This does leave a significant portion of the controller sticking out the rear end of the server rack, which is particularly sensitive considering that the link cable between controller and PXI-chassis is connected at this point. Sufficient care must therefore be taken when moving the rack, as not to break the connection by pushing the system into an object or wall. Additionally, this choice of server rack does not inhibit the system fan noise, so a different solution to shield the microphones from the fan noise had to be sought after.

Figure 4.6: DAS controller length vs rack depth

The most straightforward solution was to store the DAS-rack in one of the rooms adjacent to the test chamber. The hallway outside the main tunnel entrance was impractical, and storing anything there would constitute as blocking an emergency exit, and was therefore ruled out. Of the remaining two rooms, only one was a viable candidate considering the accessibility of the DAS and the placement of the array. The room with the cart-mounted entrance was not only located directly opposite the array, requiring the microphone connector cables to span the entire room, but would also hamper the accessibility of the DAS, since the acoustic floor panels would have to be removed every time for the door to be opened.

Routing the cables effectively and in a structured manner proved to be another challenge. A total of 64 cables, each spanning 10 meters, had to be routed from the DAS to a specific location in the array. The cables were numbered 1 through 64, according to the order of connectors in the sound and vibration modules. The largest issue with this was encountered during initial configuration of the array, where the cables tended to get entangled to such an extent that a solution had to be sought after. Considering the fact that the cables are connected to the DAS in groups of 8, bundling them in one bundle per connector would result in 8 bundles, which was much easier to route and connect to the array. This was achieved by using spiral cable binders, placed in sections of 25 centimeters with a spacing of 10 centimeters, to allow for some flexibility. Furthermore, to ensure practical placement of the microphones, a Matlab-script was written to reduce the spread of each cable bundle by splitting the microphone distribution in 8 closely spaced groups of 8, as to ensure that no two cables in one bundle would have to reach opposite ends of the array.

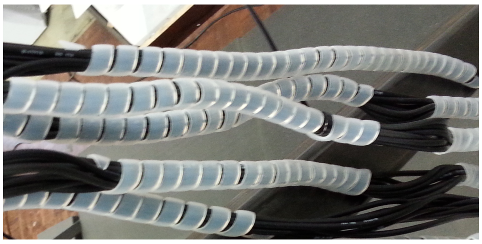

Figure 4.7: Cables clustered in bundles of eight

Having configured the hardware such that it could be used in the most practical and least invasive (noisewise) way, controlling the DAS proved to be complicated. The graphics card built-in to the controller dates back to 1998, which is reflected in the performance of the controller graphic-wise.

The lag between provided input (e.g. by moving the cursor) and the actual event happening on-screen made the device nigh inoperable, and any form of real-time data representation impossible. This was solved by enabling remote control of the controller by another device, such as a laptop or other Windows-based computing system. A remote connection allowed the second system to process all graphics-related in- and outputs, effectively reducing the lag to a much more practical level. Furthermore, remote control of the controller removes the necessity of a person being present in the room during experiment, which eliminates the chance of human interference with the experiment.

Since control of the system was extended to devices outside the DAS, the next logical step was to make the information gathered by the DAS accessible to other devices as well. This was done by creating a network shared folder on the controller, which allows anyone connected to the same network to read from and write to this specific folder on the controller. This folder can therefore be used for fast and straightforward data transfer.

The data storage system of the controller itself however proved to be a third weakness of the system. The four hard drives in the controller are configured in RAID 5, which in essence adds both write speed and data storage redundancy to the system. While this is useful for obvious reasons, this can and has[2] lead to issues. The configuration is managed by the Intel®Rapid Storage Technology software, which checks and maintains the configuration. However, if it detects an error, this is resolved by rebuilding the RAID array. No data is lost during this process, but the write speed is slowed down to a crawl, effectively making it impossible to collect data at high sampling rates. A solution to the issue can be found in connecting an external hard drive and storing the data here, but this is impractical for a longer period of time. Additionally, the maximum transfer speed achievable by USB 2.0 (the fastest available means of data transfer connectors on the controller apart from ethernet) is lower than the write speed in a RAID 5 system, bottlenecking the rate at which data can be gathered with this (temporary) solution. However, as long as the system is used in a responsible manner, this issue should not occur. Since it's not possible to set up the same RAID configuration using a different approach, the benefits of having high-speed storage capabilities with redundancy outweigh the potential downtime if this error occurs again.

4.2.2. DAS software design

The DAS came equipped with an evaluation version of the NI™LabVIEW software, and all extension packages required for hardware based data acquisition. For practicality, the MathWorks®MATLAB software was also installed on the system. Since both software packages require a license to be operated, they were configured using personal[3] account details.

At the start of the software design process, the requirements of said software were established as:

1. Free configuration of sampling frequency
2. Free configuration of sampling period
3. Free configuration of microphones to use for recording

The first requirement allows the user to choose the upper limit of the beamforming frequency range (see Nyquist frequency, Section 2.2). The time period over which the recording is to be performed determines the frequency resolution of the Fourier transformed time-domain data, following Equation 2.50. Additionally, longer sampling periods allow for averaging of cross-spectral matrices, ensuring sufficient frequency resolution whilst decreasing the influence of noise in the signal. The third requirement allows the user to choose which microphones are to be used for the recording, thereby enabling recording with subsets as well as future expansion of the number of microphones. These are the very least of the functions that the software should incorporate.

[2] During the first series of experiments, the system was booted and immediately started rebuilding the RAID array. This was the first encounter with this issue, and what caused it is still unknown. It took the better part of three days (day and night) before the system was ready for use again. In the meantime, external storage was used to allow the experiments to continue according to schedule.

[3] Because the controller was (and still is) not registered to the DUT intranet, it was impossible to reach the required license servers.

After a four-day LabVIEW course, the development process was initiated by investigating existing software, specifically the "Real-time Acoustic Camera" package, which was used for data acquisition and representation for pre-existing acoustic arrays of the ANCE-department, and was developed in-house. This package contained a multitude of functions and a very clear and complete User Interface, able to perform various data handling operations pertaining to beamforming. However, the back-end of this software was entirely uncommented. To understand the back-end of the existing software package better, one of the original developers was invited for a quick explanation session.

This resulted in the conclusion that the old software was designed for a very specific hardware configuration, and that the rewriting of this configuration to incorporate the new DAS would be very convoluted and impractical. Therefore, the old software was discarded for the new DAS. During the aforementioned LabVIEW course, the process of hardware data acquisition was not treated. However, a number of tutorial example VI's (Virtual Instruments, the technical name of LabVIEW software packages) were handed out, one of which showed data acquisition of a simulated source. This example VI[24] already contained all necessary components, and it was subsequently converted to suit the given hardware configuration.

The final software package consists of a single VI with a simple and straightforward user interface, fulfilling the aforementioned three requirements. Since all microphones are calibrated individually, each has its own specific sensitivity settings. These are stored within the microphone as a Transducer Electronic Data Sheet, or TEDS. This TEDS can be read to ensure the correct parameters are used for data recording, which is incorporated in the VI. This allows the user to connect any microphone to any cable, let the system collect the TEDS file, and run the VI with the correct sensitivities configured automatically. During recording, the data is represented on a graph in real-time, to provide the user with some insight into the strength and continuity of the signals received. The recorded data is stored in a user-specified location and file, where each file can contain multiple recordings. This way, a series of experiments can be stored within one file, providing a simple and structured way of saving data.

The file format of the recorded data is the NI™TDMS file format, since this format is the fastest, most reliable and most practical out of all available options[25]. Since the standard programming environment at the ANCE section is Matlab, a means of converting the data between the two must be obtained. An existing NI™script was adapted to perform this conversion, resulting in a file in the .mat-format containing the time-domain pressure data of each microphone per column. This data can be loaded into a Matlab function and used without the need of further adaptation.

4.3. Resulting acoustic array system

The resulting array system consists of three main components:

- Planar array
- Support structure
- Data Acquisition System (DAS)

The planar array is made up of two or three (up to the user) steel perforated plates, where each plate features 8450 perforations to which microphones can be mounted with the use of a holder tube and two hex nuts. The perforation pattern is C10 U15 (industrial standard notation, where C is perforation dimension and U is perforation pitch), with a plate thickness of 3 millimeters.

Each plate has a so-called "blind edge", i.e. an outer rim in which no perforations are made. For these plates, this blind edge measures a total of 15 millimeters from each edge of the plate to the edge of the first perforation. Longitudinal stiffening elements are mounted to the plates, which also serve as connectors between two plates. Since these are placed on this blind edge, no perforations are lost. It does mean, however, that a narrow flat strip of metal is situated at the center of the array in the two-plate configuration, as seen in Figure 4.8. The effect of this is discussed in Section 5.3.

Figure 4.8: Blind edge on center bar

The frame is modular for a number of reasons, one of which is to allow switching between square and rectangular configuration. Another is for practical purposes (i.e. transportation and storage), but a third benefit has not been mentioned yet; if at some point the array plates need replacement, or if a user requires a very precise distribution incompatible with the current plates, the plates can be removed from the frame by undoing a small number of bolts around the inner edge of the frame, allowing for simple and straightforward replacement of said plates. This makes the frame compatible with different array designs, as long as they can be mounted using the same approach as with the current plates (i.e. bolted at the edge). The fact that the array consists of generic components that can be obtained at most hardware shops makes replacement or expansion of components a simple task, if required.

The DAS is connected to the microphones in the array by eight cable bundles, each containing eight cables, numbered according to their respective DAS connector slot number. Control of the system can be done directly at the controller, but is recommended to be performed using a remote connection. The user interface is configured to allow changes to all required settings, including sampling time, sampling frequency and selection of microphones to obtain samples with. The output file is in a TDMS format, which can contain multiple experiments along with an abundance of information on these experiments. A conversion script is available to extract the recorded pressures of all microphones per experiment, and saving this in a MAT-format, to allow for post-processing with Matlab.

To allow for simple and direct employment by users unfamiliar with the system, a manual has been written, containing tips and explanations on how to (re-)configure the microphone distribution, how to extract calibrate microphone and system components, and how to perform the actual data acquisition up to and including the data transformation to Matlab. This highly increases the initial practicality of the system, by taking away much of the learning curve.

Figure 4.9: Complete array (top left), microphone placement (center left), array with configured microphone distribution (top right), array employed during test (bottom)

5 Array Testing

This chapter introduces the purpose of and test setups used for the range of experiments performed to analyze array performance. Every component of the array system has been evaluated, including the entire data acquisition system, the test chamber, the array, and the available post-processing methods. The setup, execution and outcome of each test is discussed per section, on which the final array evaluation and thesis conclusion are based.

5.1. System calibration

Before using the obtained data for further analysis, the system configuration must be checked. A simple and straightforward way to do this is by the use of a reference source with known output levels at known frequencies. Any significant offset in the post-processed data would most likely represent a configuration error, either in hard- or software. If no significant offset is found, the system can be assumed to function correctly.

The system calibration was carried out using 10 randomly picked microphones, to identify within what range the measured pressure levels match a known calibration value. To this end, a GRAS 42AA pistonphone[21] was used as a calibrated sound source. This pistonphone emits sound at 114 dB, at a frequency of 250 Hz. This is the same system that was used to perform the factory default calibration on the GRAS 40PH microphones, and should therefore adequately reflect whether the data acquisition process is performed correctly.

A single peak at 250 Hz is expected, but due to slight differences in atmospheric conditions between the factory calibration (of both the microphones and the pistonphone) and the anechoic chamber, the exact level of this peak may vary slightly from the given 114 dB.

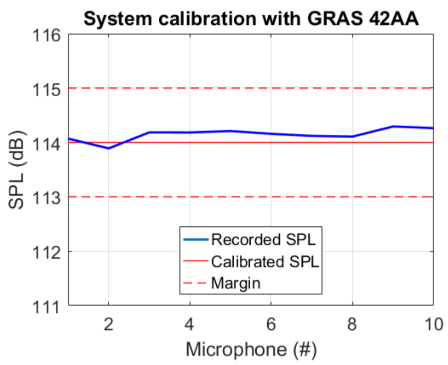

Figure 5.1: System calibration - recorded vs emitted levels

Figure 5.1 shows the pressure obtained by the system at 10 randomly chosen microphones. Since all measured levels are close to the calibrated value, the conclusion can be drawn that the system is set up correctly, from microphones to data storage. Additionally, this proves that the software used to control the system and convert the output data files is also set up correctly. A calibration margin of 1 dB is used in the given figure, and all obtained levels stay well within this given limit.

5.2. Anechoic chamber quantification

The first tests that took place in the new anechoic test chamber were a set of experiments to quantify the performance of the chamber in terms of free field representation of sound propagation. These tests were the first to be performed with the new DAS system (after the system calibration discussed in Section 5.1), and therefore served as a good system test of both the hard- and software. A small number of microphones was used to perform these tests, and since the array was not required, these experiments were performed during the array creation phase. The suggested approach to this series of experiments was based on articles by Kopiev et al[29] and Biesel and Cunefare[4].

5.2.1. Test objective(-s)

The anechoic chamber quantification consists of three main objectives, being

- determining the region of the anechoic room where the free–field propagation conditions hold,
- determining the reverberation time of the room, and
- determining the background noise at different flow speeds

The first objective is necessary since the formulation of the beamforming steering vector (Equation 2.15) is based on the assumption of free-field propagation of sound. The second objective is an indication of the anechoic quality of the room, where a lower reverberation time is preferred. The third objective is required to get an estimate of the expected noise levels during experiments with wind tunnel flow, to be able to incorporate this in test preparation.

5.2.2. Free-field assessment

Figure 5.2: Microphone on guide wire

The test setup used for the free-field assessment is quite simple. Two microphones and a single broadband white noise sound source were used. One of the microphones was mounted near the sound source, to obtain a constant reference measurement. The other microphone was moved in a straight line away from the sound source, in 10 centimeter increments, along a guide wire to maintain the same orientation and height with respect to the source. This was done over a range from 0.5 meters away from the source to 2.2 meters away from the source, in two directions. The sound source was positioned in the center of the room (above the nozzle) and, using Figure 3.3 as a reference, the two measurement directions were from the center to the upper left and the lower right corners of the room, respectively. These directions were chosen because of the difference in acoustic treatment; the upper left portion of the chamber is fully covered with acoustic floor panels and wall wedges, whereas the lower right section is uncovered, since the power and control cupboards are situated there. The OSPL (Overall Sound Pressure Level) obtained at this location was calculated and plotted. Subsequently, the decay of OSPL with radius from the source was calculated, based on the free-space propagation relation,

$$SPL_r = SPL_{ref} - 20\log_{10}\left(\frac{r}{r_{ref}}\right) \tag{5.1}$$

Ideally, the OSPL estimated with this relation is equal to the measured OSPL at a given radial distance r from the source. The reference distance (r_{ref}) and reference OSPL (SPL_{ref}) were taken at a distance of 1 meter from the source. The results are shown in Figures 5.3 to 5.6, for both measured directions.

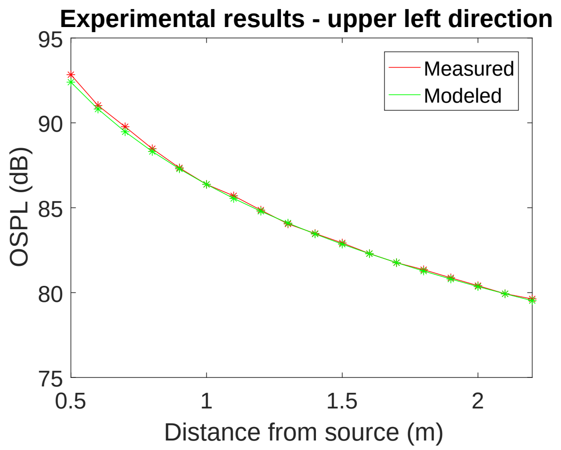

Figure 5.3: Free-field propagation upper left - theory vs measured

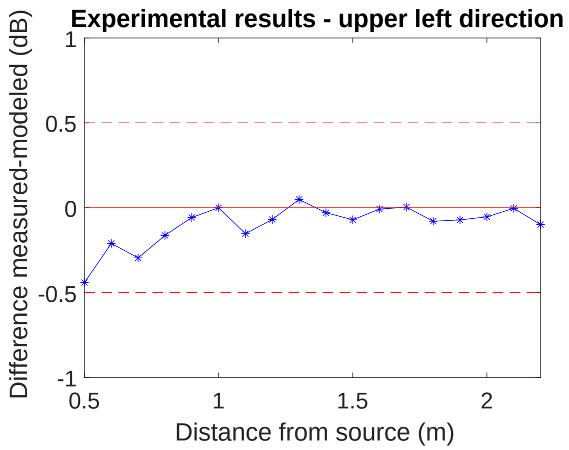

Figure 5.4: Free-field propagation upper left - level difference

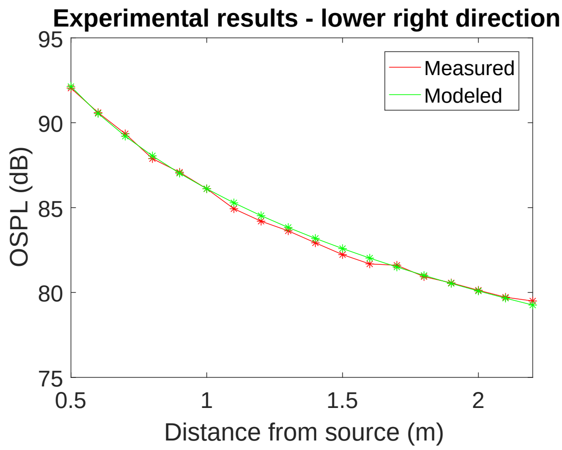

Figure 5.5: Free-field propagation lower right - theory vs measured

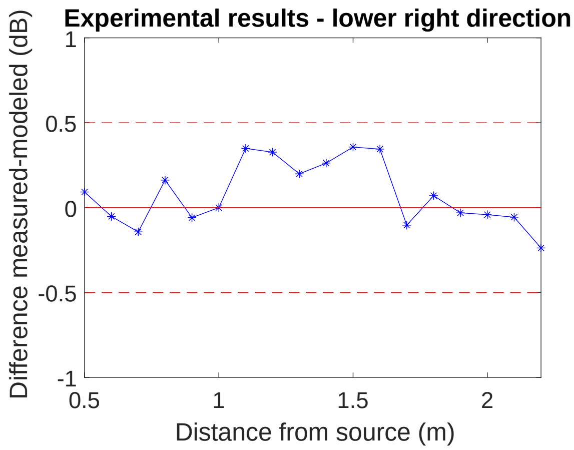

Figure 5.6: Free-field propagation lower right - level difference

As shown in Figures 5.4 and 5.6, the difference between the modeled and measured values never exceeds 0.5 dB in either positive or negative direction (as indicated by the dashed red lines). This means that between 0.5 and 2.2 meters, the free space propagation assumption holds up very well in both measured propagation directions when looking at the overall level. During the measurements, the reference level measured remained constant at 94.5 dB (recorded at 0.3 meters from the sound source), proving continuity between measurements.

The maximum allowable differences per frequency between measured and modeled free-field levels according to ISO 3745[17] are as shown in Table 5.1.

Table 5.1: Maximum allowed difference between measured and modeled free-field levels

Third octave band center frequency (Hz)	**Allowed difference (dB)**
< 630	± 1.5
800 - 5000	± 1.0
> 6300	± 1.5

This requires analysis of the obtained data in third octave bands (see Section 2.4). Since the anechoic chamber is designed for frequencies above 500 Hz, this was taken as the lower limit for this analysis as well. A representative selection of the obtained results is shown in Figures 5.7 through 5.12.

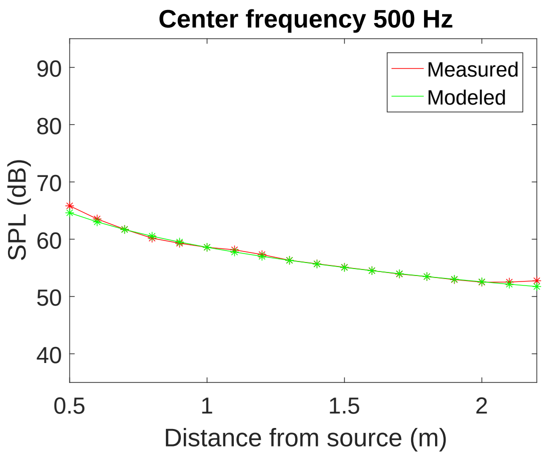

Figure 5.7: Free-field propagation upper left - theory vs measured

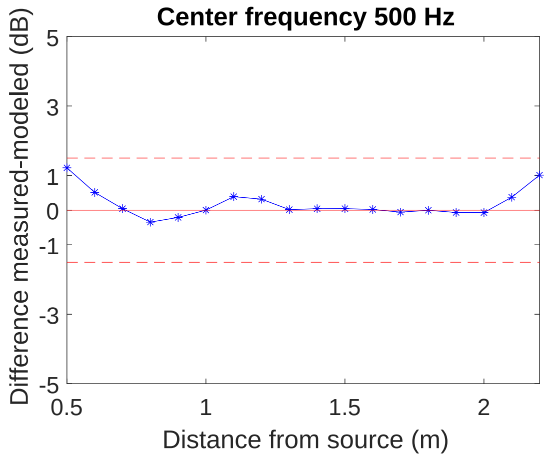

Figure 5.8: Free-field propagation upper left - level difference

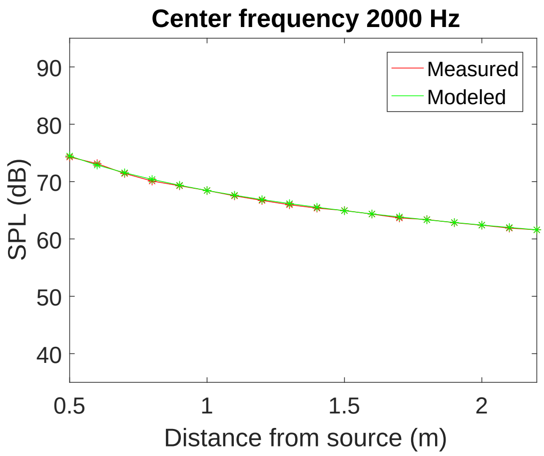

Figure 5.9: Free-field propagation upper left - theory vs measured

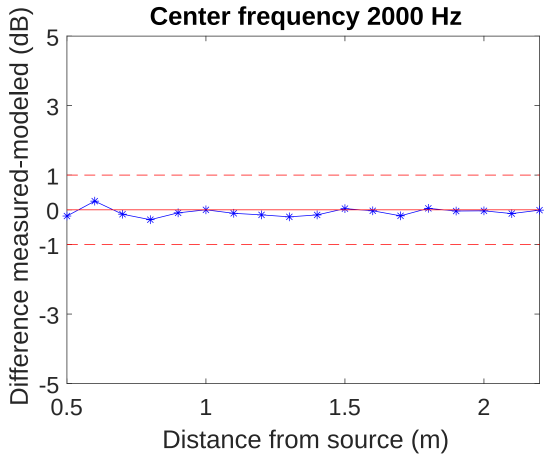

Figure 5.10: Free-field propagation upper left - level difference

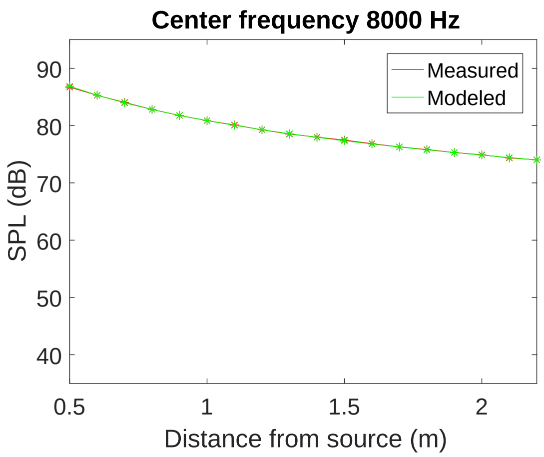

Figure 5.11: Free-field propagation upper left - theory vs measured

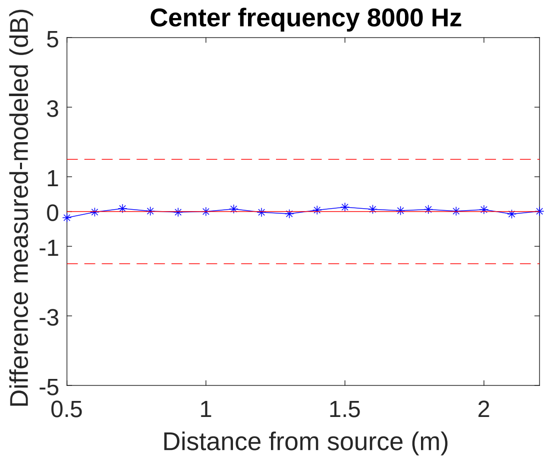

Figure 5.12: Free-field propagation upper left - level difference

Whereas for some higher center frequencies (16000 Hz and 20000 Hz) the offset between measured and modeled levels is beyond the limits indicated in Table 5.1 at short distances, the lower frequencies all exhibit similar results to Figures 5.7 through 5.12. Overall (i.e. including the aforementioned 16000 and 20000 Hz bands), the measurements indicate that the inverse square law holds for distances further than 0.7 meters from the source, for third-octave band center frequencies of 500 Hz and up, according to ISO 3745.

5.2.3. Reverberation time assessment

Assessing reverberation in the test chamber requires only a single microphone and a pulse signal generator (e.g. a clap). The reverberation time assessment aims at finding the reverberation time (T_{60}), by analyzing the pressure received by the microphone and determining the time it takes for the received signal to decrease by 60 dB. A common approach to this assessment is determining the time required for the signal to decay by 20 dB, and extrapolating this by a factor of 3. This is due to the fact that the background noise levels are often such that a decline of 60 dB cannot be achieved. The resulting decay time was found to be between 0.2 and 0.6 seconds (as indicated by the red frame in Figure 5.13) depending on the locations in the room where the noise is generated and recorded. The longest reverberation time was recorded above the nozzle in the center of the chamber, which is situated on top of a cavernous settling chamber. Additionally, the upper floor of the test section has received no acoustic treatment at all, as well as some walls and systems (such as the power and control cupboards), and therefore do not contribute to acoustic damping as much as the treated walls. If these were to be covered, an even lower reverberation time might be achieved.

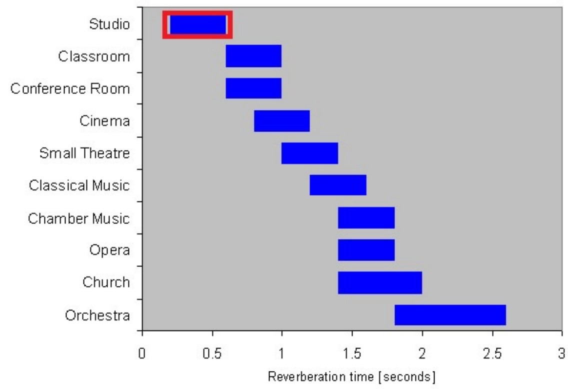

Figure 5.13: T_{60} of different rooms[60]

A T_{60} below 0.3 seconds is required for a room to be classified as anechoic or "acoustically dead", according to ISO norm 3382. Since no sound recording will take place directly above the reverberant settling chamber[1], the T_{60} obtained at this location can be disregarded. At the array location, the range of decay times is found to be between 0.2 and 0.3 seconds, well within the limits imposed by the ISO standard. The effect of the measured reverberation time above the settling chamber is expected to be negligible. During tests with airflow, the effect of flow induced noise is much larger than any reverberant noise. As for testing without flow, the level of the directly received sound wave is expected to be much larger than any reverberance-induced indirect sound wave. For good measure, it's possible to cover the tunnel nozzle for experiments without flow, therefore ensuring absolutely no acoustic reverberation originating from the settling chamber. Several panels of the same acoustic foam used to treat the ceiling are still available, and are sufficiently large to cover the nozzle. Since this foam is quite brittle, placing a wooden board between the nozzle and the foam panel might be required, as to ensure that no pieces of foam come loose and fall into the tunnel.

[1]That would place the microphone directly in the flow, which is not advised, since the velocity-induced pressure at the microphone membrane might be above the rated maximum

5.2.4. Flow noise assessment

The wind tunnel is rated to provide flow speeds of up to 40 m/s. The noise generated by the flow was recorded with a sampling frequency of 50 kHz, in steps of 2.5 m/s for a duration of 20 seconds. This recording was then analyzed, and the results are shown in Figures 5.14 through 5.16. Figure 5.14 shows the OSPL and OASPL (A-weighted OSPL) versus flow speeds, where seems to be a logarithmic relation between flow speed and OSPL upward of 10 m/s. Applying A-weighting to the measured OSPL shows a significant reduction in level. A-weighting is a method to weigh the power of frequencies on a curve, as determined by the IEC 61672:2003 International Standard and explained in Section 2.4. The curve is displayed in Figure 2.4, which shows a significant decrease in power for low frequencies. When analyzing the flow noise spectra (Figures 5.15 and 5.16 show the spectra obtained with a single microphone), the lower frequency range does show to contain most of the sound power, explaining the impact of applying A-weighting to the measured OSPL.

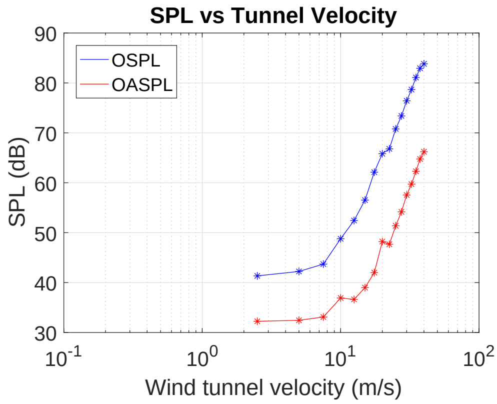

Figure 5.14: OSPL and OASPL per wind tunnel velocity

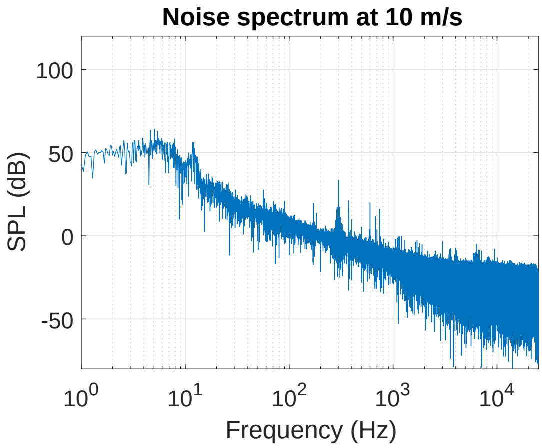

Figure 5.15: Noise spectrum at 10 m/s flow velocity

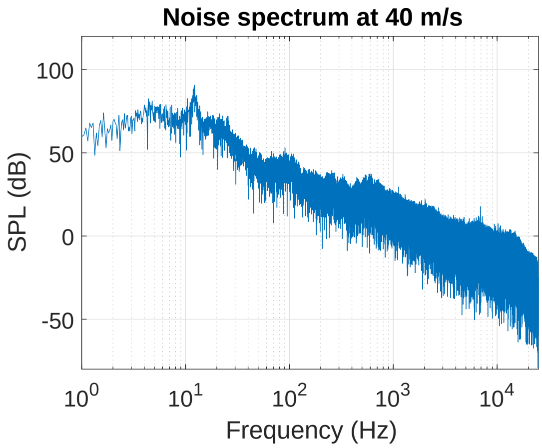

Figure 5.16: Noise spectrum at 40 m/s flow velocity

With knowledge of the noise spectrum generated by the flow, experiments can be designed such that the expected signal-to-noise ratio at a given flow speed for a given (range of) frequency(/-ies) is sufficient for further analysis.

5.2.5. Conclusion

The room exhibits anechoic properties for frequencies of 500 Hz and up, but could use improvement to further decrease the reverberation time. In the current configuration, free-field propagation can be assumed at distances of 0.7 meters and up from the sound source, for frequencies of 500 Hz and up. Both these conclusions are based on analysis of the obtained data within limits imposed by the appropriate ISO standards for anechoic test facilities. The noise induced by the tunnel flow seems to follow a logarithmic relation at velocities upward of 10 m/s, and is mostly concentrated in the low frequency regions. This should be taken into account when designing experiments aimed at low frequency analysis under high wind tunnel velocities.

5.3. Array calibration

The calibration of the array was performed in the anechoic test chamber, using a calibrated sound source. The calibration was performed by means of conventional beamforming as well as spectral analysis of individual microphones. After analysis of the calibration results, potential causes for the measured offsets were identified, for which improvements to the array were made. The experiments were repeated to assess the improvements on the obtained results, and the final calibration result is discussed, along with the most important unknowns and potential causes of offsets in the calibration process.

5.3.1. Test objective(-s), test setup and test conditions

One of the purposes of performing array calibration is to obtain an estimate of the offset in sound power level between the emitted and recorded signals. Whereas this was already performed for single microphones as a system test, it is yet to be performed for the array as a whole. To perform this analysis, a calibrated sound source is required, of which the location and the emitted sound power level per frequency are known. The array must be configured with a microphone distribution of which the locations are known as accurately as possible, to be able to formulate an accurate set of steering vectors.

The noise source, as with the microphones and the DAS, was chosen ahead of the start of this project. The Belgian company Qsources[48] was tasked to develop a calibrated omnidirectional sound source for wind tunnel measurements. Their final product was the QindW miniature sound source[64]. This source is connected to an amplifier that is capable of generating white and pink noise in three frequency bands (designated L, A and E-bands) as well as taking an external input signal.

Figure 5.17: Qsources QindW omnidirectional sound source

The sound source was calibrated at a fixed amplifier setting, for the built-in signals only[63]. Using an external input signal for calibration purposes was therefore impossible. The calibrated sound power level was provided by the manufacturer per third octave band, and can be found in Table D.1 of Appendix D, for each of the three frequency bands and for both noise types[2]. This meant that calibration could only be performed per third octave band, within the frequency ranges as indicated by the L, A and E-bands. The largest range of these was given by the E-band, spanning 315-6300 Hz.

This project was undertaken in conjunction with another thesis project by another master student, S. Luesutthiviboon[32], whose research was aimed at optimizing microphone distributions on planar arrays. This proved to be an excellent test of the flexibility and practicality requirements of the array, since testing optimized microphone distributions meant applying changes to the microphone distribution quite often, which is exactly the purpose of this flexible array. The choice of microphone configuration to be used for calibration was made based on the first optimized distribution resulting from this project. Three configurations were tested to determine the performance of the optimized distribution:

- a reference distribution, which is used as a starting point of the optimization process,
- an Underbrink spiral distribution, which is used to measure performance of the optimized distribution[3], and
- the resulting distribution.

[2]For unknown reasons, calibration data of the white noise L-band was not provided.

[3]The Underbrink spiral is regarded as the best microphone distribution for planar acoustic arrays in terms of all-round performance, measured by both main lobe width and side lobe presence[54][47]

The availability of the anechoic test chamber was shared between the two projects, and since the newly optimized distribution yielded the best results out of the three tested configurations (in terms of side lobe presence and main lobe width), this distribution was used for the calibration of the array[4]. The distribution used is shown in Figure 5.18. Since this distribution is based on a square array, and due to the fact that changes were still being made to the wind tunnel, the 2 by 2 meter square array configuration was used rather than the 3 by 2 configuration (see also Section 4.1). This choice did not impede the progress of either thesis project.

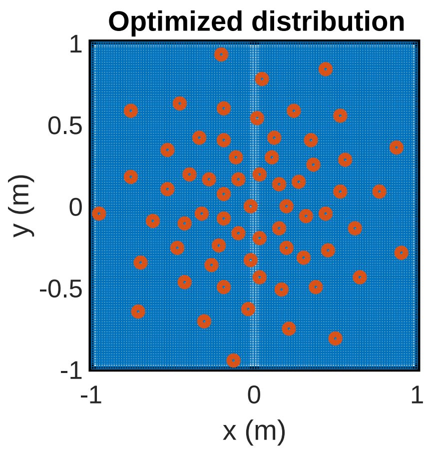

Figure 5.18: Optimized distribution (see Appendix E)

The microphone positions according to the optimized distribution did not overlap exactly with the actual available microphone positions (i.e. the plate perforations). To obtain a fit, a script was written to locate the nearest available perforation to a given set of microphone coordinates, which resulted in a small offset near the center of the array. The calibration source was suspended from the tunnel ceiling, aligned with the center of the array both horizontally and vertically. The perpendicular distance between the array and the sound source was measured at 1.495 meters. Three atmospheric test conditions were recorded and averaged during the testing period: temperature, pressure and relative humidity. All three influence the speed of sound in air, and are therefore required for accurate acoustic measurements. For this experiment, the following conditions were as shown in Table 5.2.

Table 5.2: Atmospheric test conditions - calibration

Temperature (°C)	23.8
Pressure (Pa)	101093
Humidity (%)	55.75
Amplification setting (dB)	40 (unless indicated otherwise)

For this analysis, the source signal used was White E with the amplifier set to the calibration settings. Since the sound power level is given rather than the sound pressure level, the results obtained with beamforming need to be corrected with Equation 2.26. The actual directivity factor $Q(\theta,\phi)$ of the source is unknown, so for now the standard value of 1 is used, assuming perfect spherical propagation. The possible implications of this assumption are discussed later in this section. A reference distance r_{ref} of 1 meter from the source was taken.

CSM time-domain averaging can be used to reduce noise in the obtained signal. The data obtained during this experiment was recorded over a period of 60 seconds, with a sampling frequency of 50 kHz. For the beamforming results, this data was split into 60 segments, each with a duration of 1 second. This yields a frequency resolution of 1 Hz. These segments were then transformed to the frequency domain, the CSM according to each segment was calculated for the given frequency, and the resulting 60 CSM's were averaged to obtain the time-averaged CSM for the given frequency, as shown in Equation 5.2:

$$\mathbf{C}_{avg} = \frac{\sum_{z=1}^{Z} \mathbf{C}_z(f)}{Z}, \tag{5.2}$$

where Z indicates the amount of signal segments (in this case, $Z = 60$).

[4]For more information on the approach to and outcome of the microphone optimization, please consult the final master thesis report by Salil Luesutthiviboon[32].

5.3.2. Test results

As stated at the beginning of this section, the obtained data was analyzed both by means of conventional beamforming and per individual microphone. The beamformed results are discussed first.

A source map of 2 by 2 meters was used for beamforming, with a resolution of 1 centimeter in both x and y-directions. This resolution was chosen based on the accuracy with which the actual location of the sound source with respect to the array could be determined. The autopower matrix **A** was calculated for each frequency within the given third octave band, after which all resulting matrices were added together to obtain the final autopower matrix $\mathbf{A}_{band}$ for the given band. The experiment was carried out twice, to obtain two independent data sets. Both sets were analyzed, and the results are comparable. The resulting beamform maps are very clear; the source is located exactly in the center of the map, indicating that the position is estimated correctly. An example of this is shown in Figures 5.19 and 5.20.

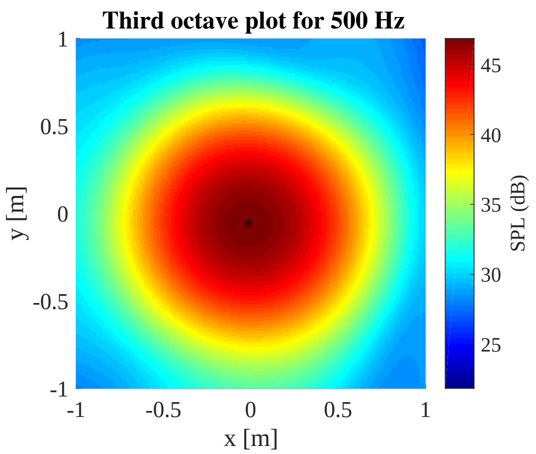

Figure 5.19: Beamform results with calibrated source - 500 Hz

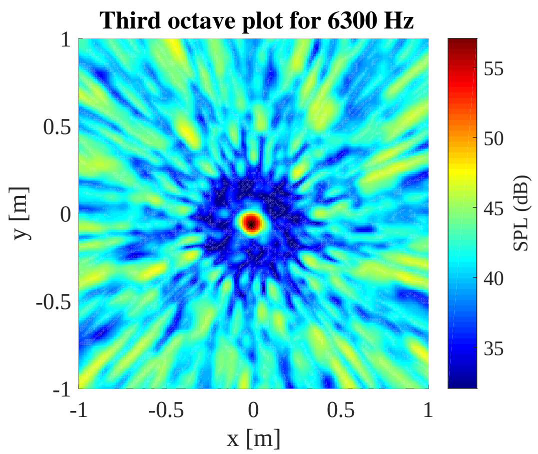

Figure 5.20: Beamform results with calibrated source - 6300 Hz

The peak location, and therefore the estimated source location, corresponds perfectly to the actual source position. This means that the array is capable of estimating positions at least with an accuracy of 1 centimeter. By extracting the maximum sound pressure level from these beamform results, and subsequently converting it to sound power level, it can be compared to the sound source calibration data. This is shown in Figures 5.21 and 5.22. The obtained data is only shown between 500 and 6300 Hz, since the source is designed and therefore rated to operate well within the region between 315 and 6300 Hz, determining the upper limit. The anechoic test chamber is rated to operate well for frequency analysis above 500 Hz. Hence, analyzing spectra outside the resulting combined range does not necessarily yield useful information on array performance, since these other factors become unpredictable as well.

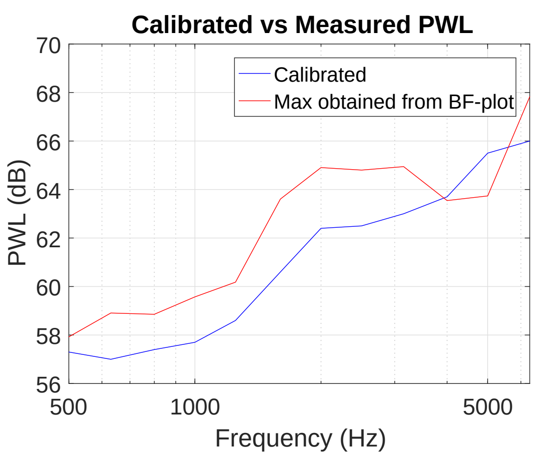

Figure 5.21: Beamform level vs calibration data - test 1

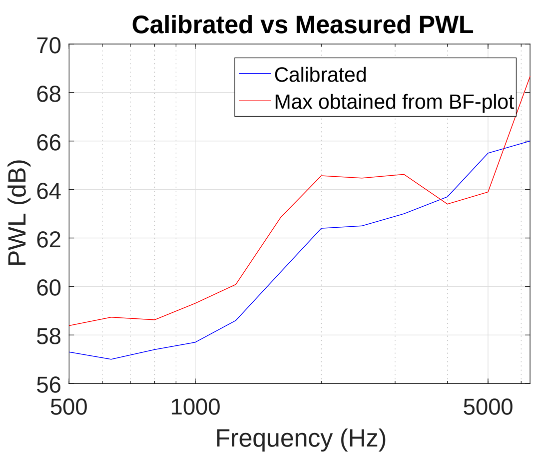

Figure 5.22: Beamform level vs calibration data - test 2

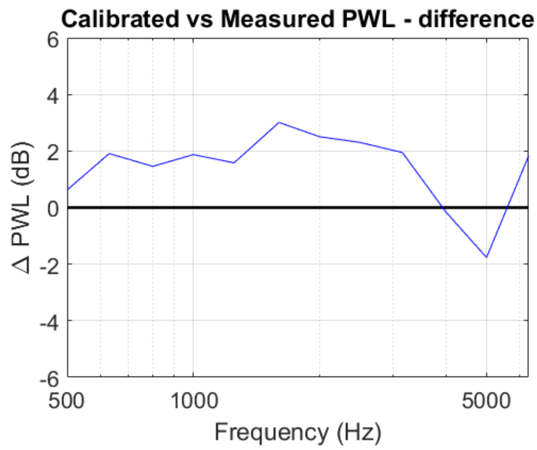

Figure 5.23: Difference measured-calibrated PWL - test 1

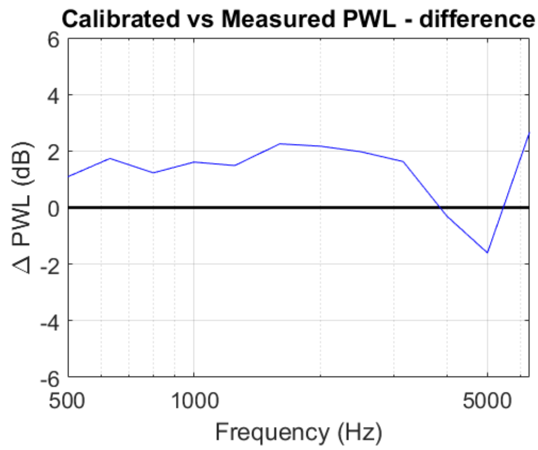

Figure 5.24: Difference measured-calibrated PWL - test 2

Small deviations between the two tests can be attributed to the true randomness in the generated white noise signal, as well as imperfections in the test setup. Interestingly, the difference between the measured and calibrated PWL seems to be somewhat continuous for a large part of the analyzed spectrum, with the measured PWL on average 2 dB higher than the calibrated value. This difference is shown in Figures 5.23 and 5.24. However, both experiments show a dip at the center frequencies of 4000 and 5000 Hz, where the measured power becomes lower than the calibrated power of the source. An analysis of the individual microphone spectra was performed to attempt to identify a potential cause of this.

When analyzing the individual microphone spectra, no beamforming is performed. To calculate the PWL from the measurements of a single microphone, the SPL at the microphone is calculated. Then, Equation 2.26 is applied, where r_{ref} is set to the radial distance between the microphone and the center of the sound source. The result of this for both data sets is shown in Figures 5.25 and 5.26.

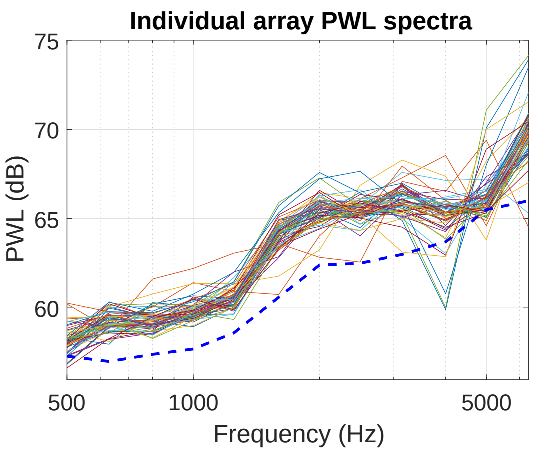

Figure 5.25: Individual microphone spectra - test 1

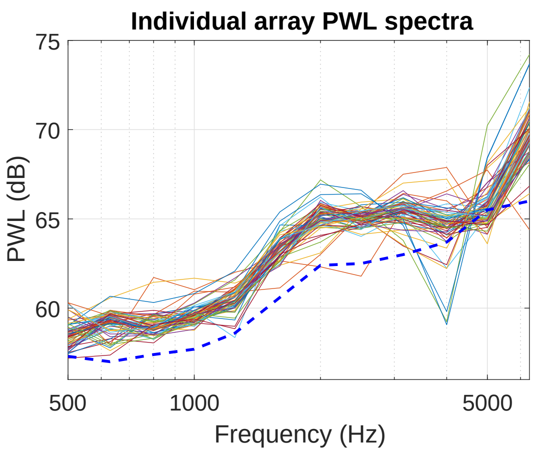

Figure 5.26: Individual microphone spectra - test 2

The blue dashed line represents the calibrated source PWL. Again, an average offset of about 2 dB is obtained, except for a subset of microphones (5 in total) between the 4000 and 6300 Hz center frequencies. To identify a potential cause of this phenomenon, the locations of the microphones exhibiting large offsets (negative and positive) from the mean microphone level were identified and located.

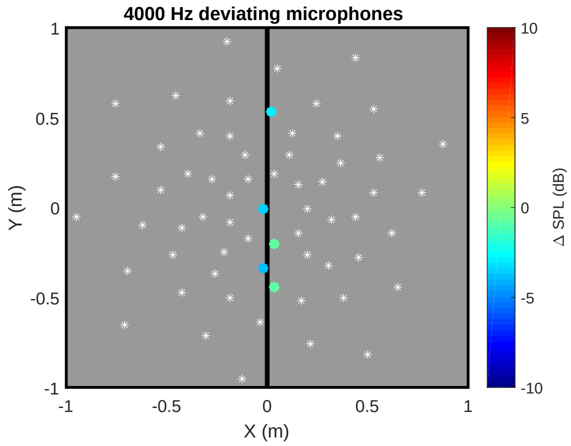

Figure 5.27: Location of microphones with largest deviation - 4000 Hz center frequency

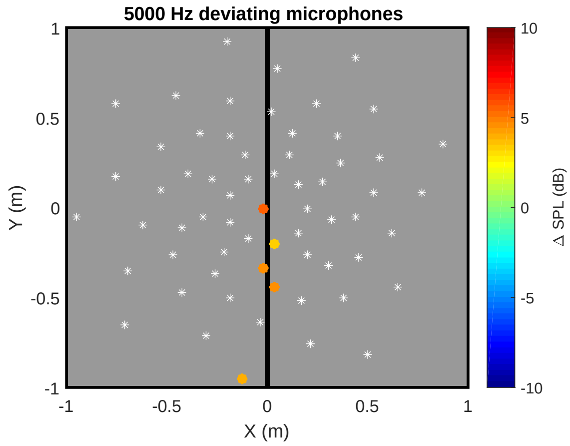

Figure 5.28: Location of microphones with largest deviation - 5000 Hz center frequency

Figures 5.27 through 5.29 seem to indicate that the largest offsets from the mean microphone obtained PWL are found around x = 0, as indicated by the colored dots. The white dots indicate the other microphones in the array. Since the center of the array is where the two plates are joined together, this area features a large strip of non-perforated metal. This could be the cause of excessive reflections, leading to constructive or destructive interference of the reflected and the incident waves. To test this hypothesis, all non-perforated metal on the array was covered with a layer (10 millimeters thickness) of Flamex acoustically absorbent foam[35]. In addition to this, all microphones were surrounded with a square patch of the same foam, to further prevent the reflection of incident waves.

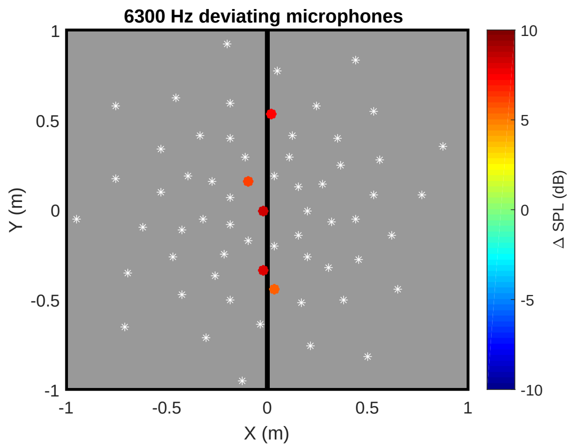

Figure 5.29: Location of microphones with largest deviation - 6300 Hz center frequency

Figure 5.30: Application of Flamex foam to the array

The foam strips were attached to the array with hook-and-loop fasteners, to allow easy removal and replacement when reconfiguring the structure. Having covered the bare metal components of the array as well as the areas immediately surrounding the microphones with sound absorbent foam, the previous tests were repeated to identify if any performance gain was achieved. The results obtained by beamforming are shown in Figures 5.31 and 5.32. The application of the square patches around the microphones proved to have no significant effect whatsoever, but covering the center bar did have a noticeable impact on the obtained results. The foam around the microphones was therefore removed for the remainder of this calibration process.

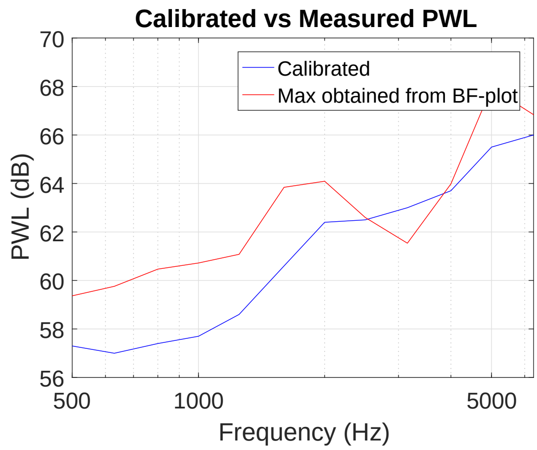

Figure 5.31: Beamform level vs calibration data - test 1
1 foam layer on center bar

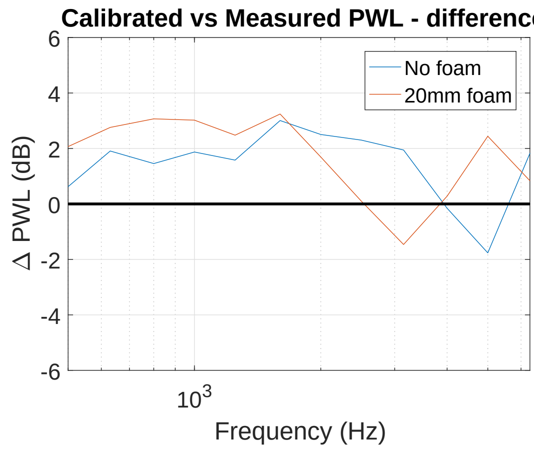

Figure 5.32: Difference measured-calibrated PWL - comparison

The frequencies for which the negative difference appears have shifted down, from the 4000 and 5000 Hz third octave frequency bands to the 2500 and 3150 Hz third octave bands, as shown in Figure 5.32. Additionally, the average deviation from the calibrated values has increased. The application of the foam clearly has some effect, but this improvement did not yield the expected result.

Having covered the beamform result, individual microphone analysis was performed and compared to the previously obtained results. These are given in Figures 5.33 and 5.34,

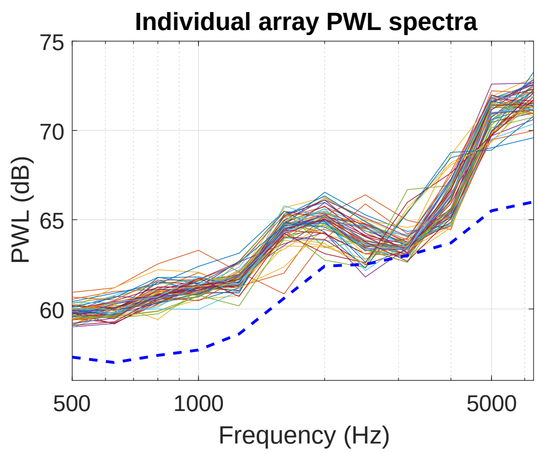

Figure 5.33: Individual microphone spectra - test 1
20mm foam layer on center bar

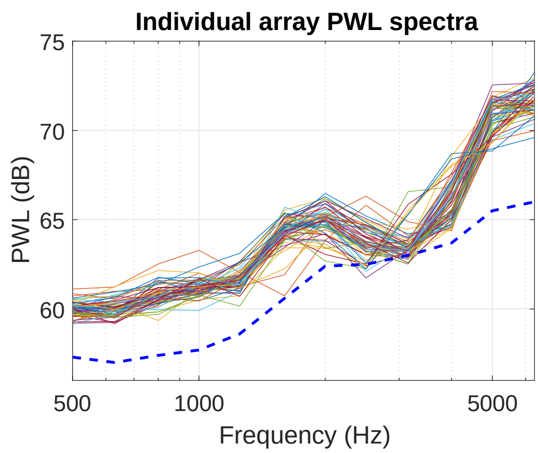

Figure 5.34: Individual microphone spectra - test 2
20mm foam layer on center bar

The peaky behavior shown in Figures 5.25 and 5.26 has disappeared, which seems to indicate that the application of the Flamex acoustic absorbent foam had a positive effect on the obtained results. However, both the beamform results and the individual microphone spectra analysis show that there is still a frequency range in which the measured values differ from the mean measured values; whereas most measured levels exhibit a positive offset between 2 and 3 dB from the calibrated values, the values obtained in this specific range show either a very small or even negative offset. This region seems to have shifted to the third octave bands between the 2000 and 4000 Hz center frequencies. Another layer of foam was applied to the center bar, for a total of 20 millimeters of foam thickness, in an attempt to further decrease the interference caused. The results are shown in Figures 5.35 and 5.36.

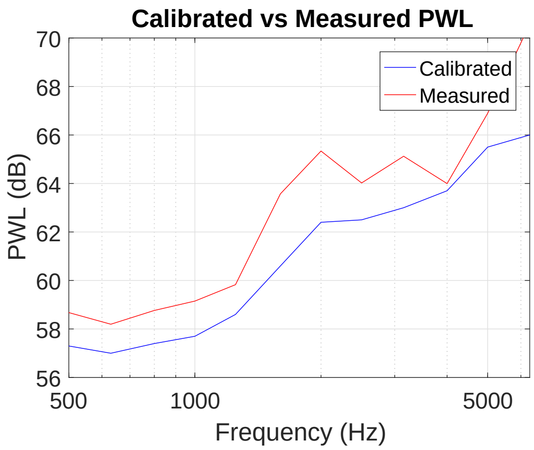

Figure 5.35: Beamform level vs calibration data - test 1 40mm foam on center bar

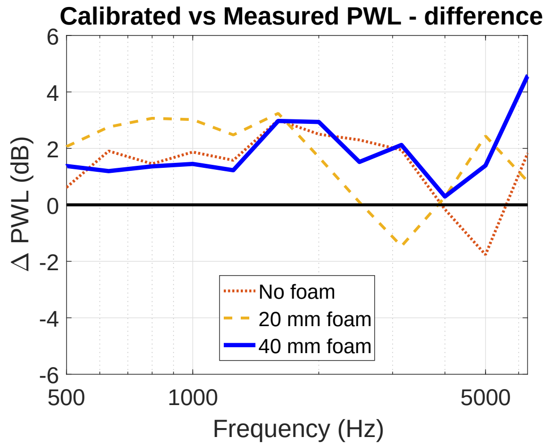

Figure 5.36: Offset measured-calibrated PWL - comparison

Applying two layers of foam seems to have decreased the adverse reflections caused by the center bar such that the difference between measured and emitted power levels is positive for all measured third octave bands, indicating more constant behavior. This positive difference can be attributed to multiple causes, which are:

- Reflections from the array surface,
- Reflections caused by objects within the anechoic room,
- Non-spherical directivity of the sound source, and
- Calibration errors.

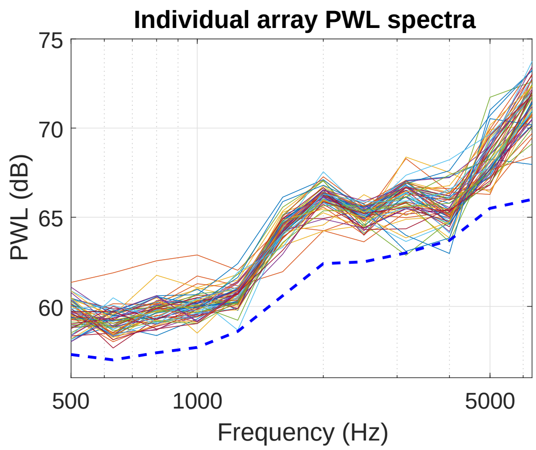

Figure 5.37: Individual microphone spectra - test 1 40mm foam on center bar

The first potential cause can be analyzed by taking a measurement without using the array. Four microphones were set up in a configuration as shown in Figure 5.38, mounted to a vertical pylon, and the average power recorded by these microphones is shown in Figure 5.39 (the magenta line), compared to the power obtained by all microphones in the array (the gray surface, covering the microphone spectra spread of Figure 5.37).

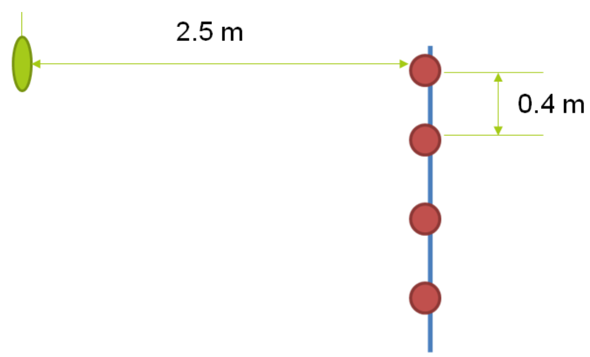

Figure 5.38: Free space measurement setup

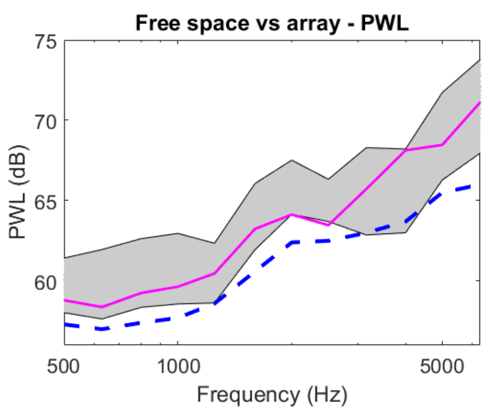

Figure 5.39: Free space average vs array microphone PWL spectra

Since these microphones also show a larger measured power than the calibrated value, the cause must be sought outside the array. The second potential cause is impossible to determine without a second calibrated sound source, and based on the quantification of the anechoic test chamber, no excessive reverberations should be present to cause an increase in perceived level. This leaves the third option.

The calibration tests were performed with the source oriented such that emission along its principal axis was measured. In the conversion from SPL to PWL, the directivity $Q(0,0)$ of the QindW sound source is assumed to be 1 (i.e. $DI(0,0) = 0$ dB, which means perfect spherical sound propagation. The only comment about directivity as provided by the manufacturer is that *"the source shows good omnidirectional behavior"*[64], but considering the shape of the source it is safe to assume that perfect spherical propagation is not achieved with this source.

The directivity factor is an indication of the shape of the propagating sound field with respect to a perfect sphere, in a given emission direction. A factor of 2 would therefore indicate a hemispherical wavefront, a factor of 4 would indicate a quarter sphere et cetera. The estimated correct directivity index for this source is between 1 and 2. Based on the results shown in Figure 5.36, a calculation was performed to obtain the value for $Q(\theta,0)$ for which the average offset between measured and emitted value was minimal. This resulted in a value of 1.4825, which fits the expected range of values between 1 and 2. The result of using this value is shown in Figures 5.40 and 5.41.

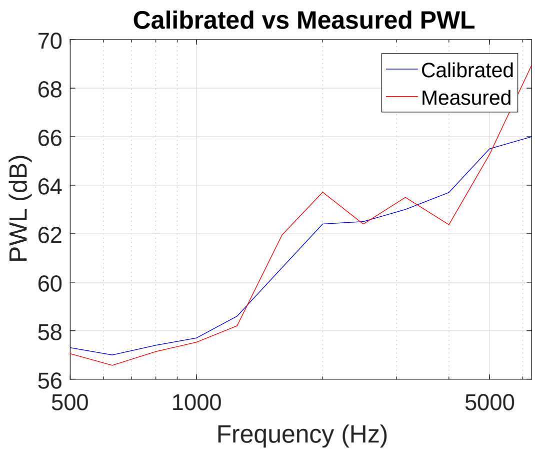

Figure 5.40: Beamform level vs calibration data - test 1
2 foam layers on center bar, $Q(0,0) = 1.4825$, $DI(0,0) = 1.71$ dB

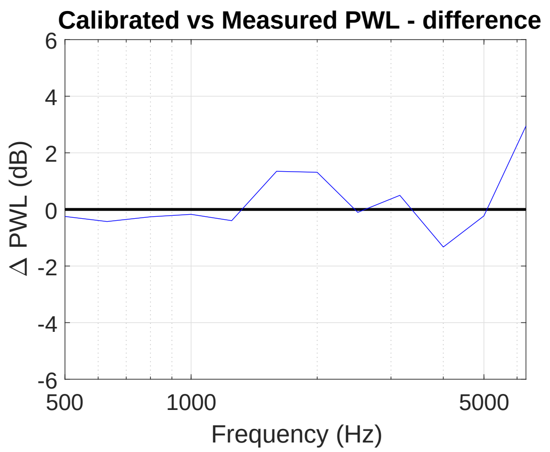

Figure 5.41: Offset measured-calibrated PWL - test 1
2 foam layers on center bar, $Q(0,0) = 1.4825$, $DI(0,0) = 1.71$ dB

Since the second half of the third octave band corresponding to the 6300 Hz center frequency is outside the rated operating regime of the noise source, the resulting accuracy in SPL estimation was assessed within the 500 Hz to 5000 Hz range, as shown in Figure 5.42. Under the assumed optimal directivity index, the resulting accuracy with which the SPL is determined lies within the 1.5 dB limits indicated by the ISO 3745 standard[5] (see Section 5.2).

The calibration experiments with two layers of foam on the center bar were repeated for lower amplifier power settings (all previous tests were performed at the calibration setting of 40), to see if similar results were obtainable (i.e. independent of sound power level). These are shown in Figures 5.43 and 5.44.

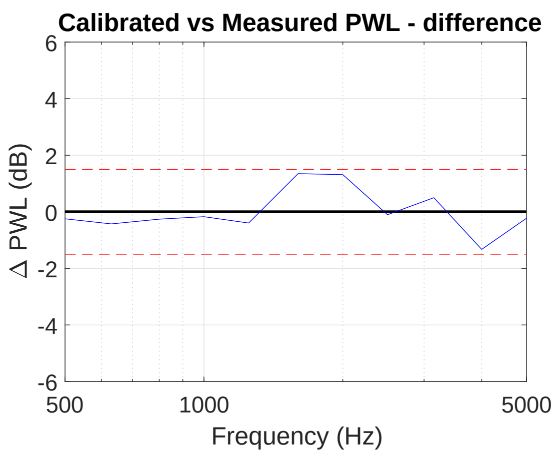

Figure 5.42: Offset measured-calibrated PWL - 500 to 5000 Hz
2 foam layers on center bar, Q = 1.4825, $DI(0,0) = 1.71$ dB

[5]ISO 140 and ISO 3382 can also be used for array calibration, but offer a larger allowed deviation than ISO 3745

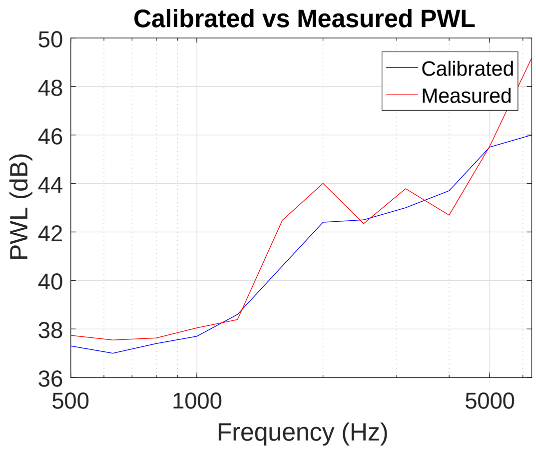

Figure 5.43: Beamform level vs calibration data - amplification level 20, 2 foam layers on center bar, Q = 1.4825, $DI(0,0) = 1.71$ dB

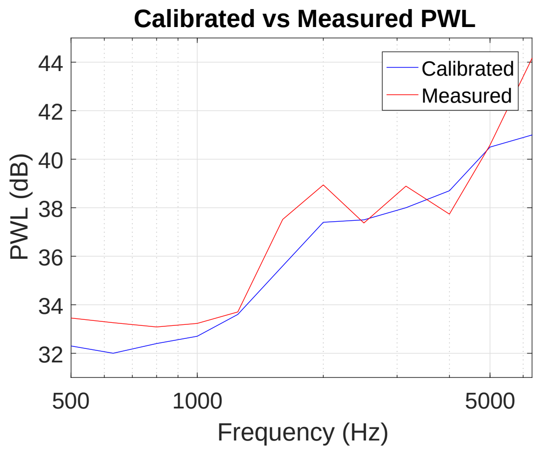

Figure 5.44: Beamform level vs calibration data - amplification level 15, 2 foam layers on center bar, Q = 1.4825, $DI(0,0) = 1.71$ dB

These figures show results similar to Figure 5.40. The increased level difference in the lower frequency range of Figure 5.44 is due to the noise almost reaching background noise values. When the amplifier is set lower than 15, this effect becomes more pronounced.

Additional measurements on the sound source are required to confirm its directivity.

5.3.3. Conclusions

In terms of sound source location estimation, the array performs well for a single source, and further analysis on multiple source configurations is discussed in the following sections. To provide a final conclusion to the array calibration in terms of sound power level estimation, more knowledge on the directivity of the sound source is required. If the calculated directivity factor of $Q(0,0) = 1.4825$ ($DI(0,0) = 1.71$ dB) is close to the actual directivity factor of the source in this direction, then the array provides accurate power level estimations between the 500 and 5000 Hz third octave bands. For these bands, the measured level is within 1.5 dB of the calibrated value. At the center frequency of 6300 Hz, half of which band lies outside the rated operating range of the source, a slightly larger deviation from the calibrated values is noticeable.

5.3.4. Suggestions for future work

Since the array could only be calibrated in third octave bands for a limited frequency range, the main suggestions for future expansion of this calibration lies in the use of a different noise source. The main properties of this other source should be:

- Guaranteed performance over larger frequency range,
- Calibration data in smaller frequency bands, and
- Known source directivity in all directions.

These three factors are the largest shortcomings of the current source, and will allow for a more detailed insight in array performance in terms of sound power level determination.

5.4. Deconvolution method assessment - high signal-to-noise ratio

In Section 2.3.3, the impact on and importance of obtaining a clear and accurate initial PSF before applying CLEAN-SC and specifically CLEAN-PSF was discussed. In this section, that point is explained with actual test data being compared to simulated data, after which the performance of the array is tested for a situation with multiple individual sound sources.

5.4.1. Measured and simulated PSF

The results as obtained for the array calibration discussed in Section 5.3 were assessed further by comparing the beamforming results of the measured data to a PSF based on simulated data. The location and value of the maximum were obtained from the measured data, and used to model a monopole point source. The results are shown in Figures 5.45 through 5.50. The levels range in the plots is set relative to the maximum in each plot.

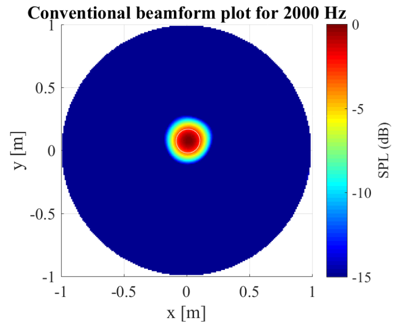

Figure 5.45: Beamform results with calibrated source - 2000 Hz

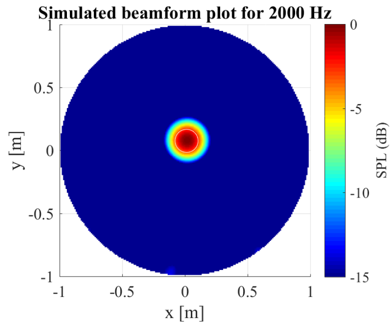

Figure 5.46: PSF of simulated source - 2000 Hz

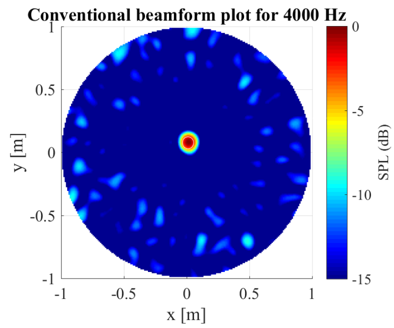

Figure 5.47: Beamform results with calibrated source - 4000 Hz

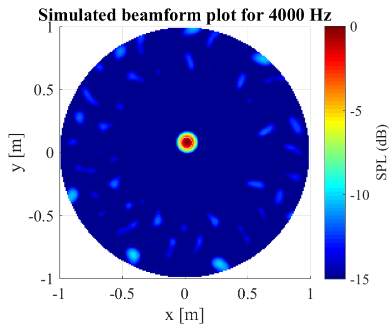

Figure 5.48: PSF of simulated source - 4000 Hz

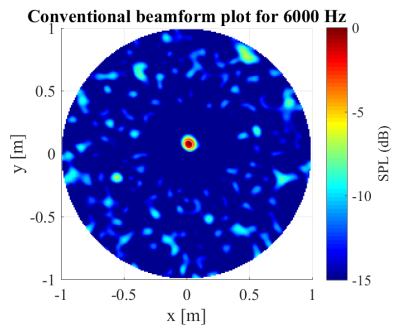

Figure 5.49: Beamform results with calibrated source - 6000 Hz

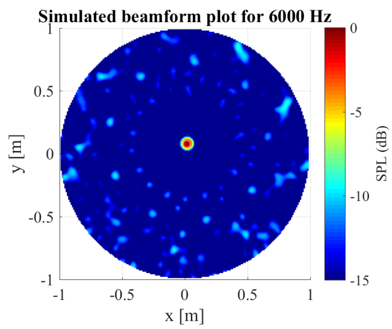

Figure 5.50: PSF of simulated source - 6000 Hz

The microphone distribution used in this experiment is optimized for a circular source map with a radius of 1 meter, and the region of the source map used for this part of performance analysis is corrected correspondingly[6]. At first glance, the measured and simulated PSF's correspond well in terms of main lobe beam width and side lobe distribution. The average side lobe level seems to be higher for the experimental results, which may be explained by the difference between a modeled monopole point source and the actual non-monopole non-point sound source, as well as imperfections in the test setup (e.g. background noise or microphone configuration errors). This is further exemplified in Figures 5.51 through 5.54.

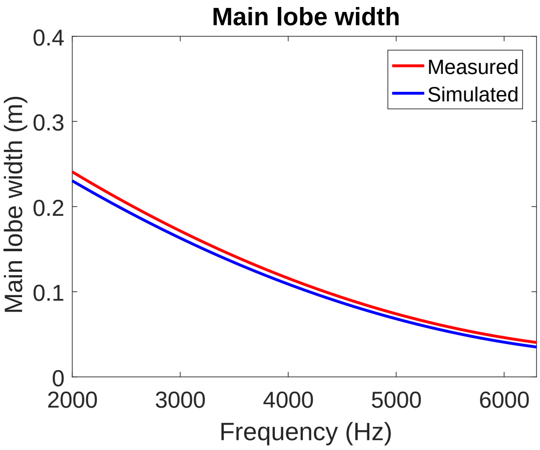

Figure 5.51: Main lobe width - simulation and measurement

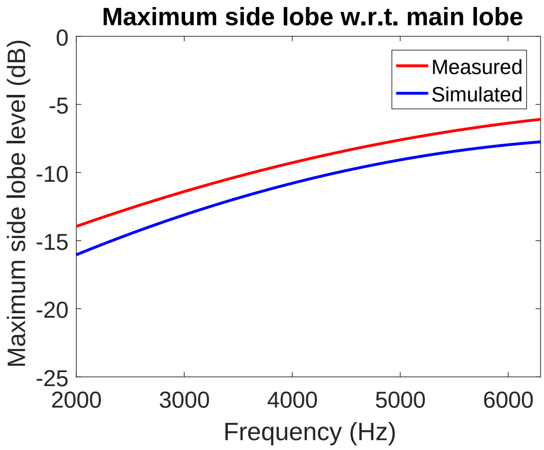

Figure 5.52: Maximum side lobe level - simulation and measurement

The frequency range used for analysis was set between 2000 and 6300 Hz. The upper limit is dictated by the operating capabilities of the sound source, whereas the lower limit is dictated by the ability to identify side lobes within the given source map radius; under 2000 Hz, side lobes were no longer accurately identifiable (the maximum fell below the -17.57 dB limit imposed by the Bessel function approximation, see Section 2.6). Analysis was performed in this range without CSM time averaging (i.e. highest possible frequency resolution and no noise reduction due to averaging) in steps of 20 Hz, and the interpolated results are shown. As can be seen in Figure 5.51, the measured and simulated main lobe width are quite similar. Since the main lobe width depends mainly on the array aperture and beamforming frequency, this similarity is expected. The slightly higher measured main lobe beam width can be explained by the difference between the simulated and the actual source geometry.

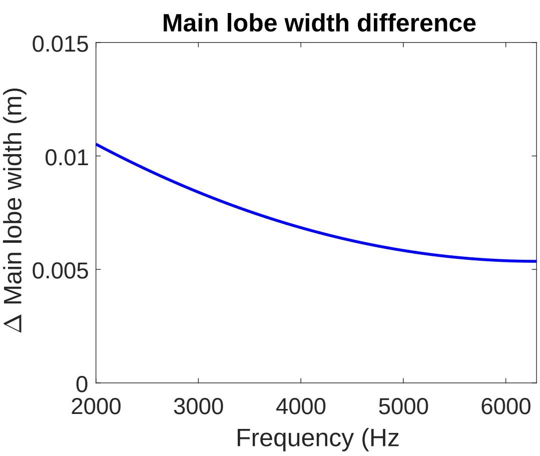

Figure 5.53: Difference in main lobe width between simulation and measurement

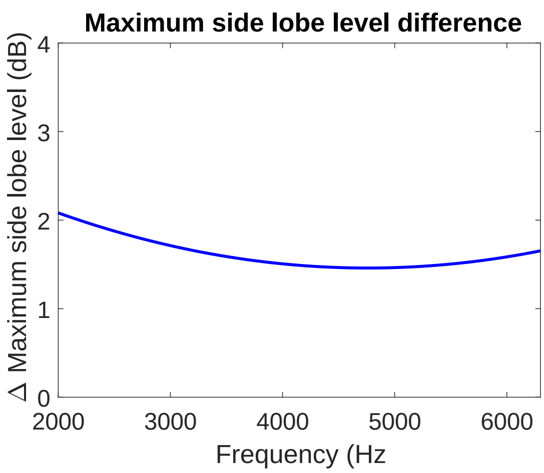

Figure 5.54: Difference in maximum side lobe level between simulation and measurement

[6]More information on the optimization method used to come up with the microphone distribution used can be found in the thesis report by S. Luesutthiviboon[32]

For a higher frequency, a smaller main lobe width is obtained, and the absolute difference between measured and simulated main lobe width decreases accordingly. In terms of side lobe performance, the measured data shows a generally higher side lobe level than the simulated data. This is explained by the fact that the simulation assumes perfect conditions, which do not hold for test scenarios. The highest side lobe level is measured at slightly under -6 dB relative to the main lobe, at the highest frequency in the given range. According to the Random Array Theory by Steinberg (as discussed in Section 2.6), the peak side lobe level is unlikely to exceed the average side lobe level by 10 dB. The theoretical average side lobe level (according to Steinberg) can be calculated as $10\log_{10}\left(\frac{1}{N}\right)+3 \approx -15.06$ dB, using $N = 64$ as used for this array. This would place the peak side lobe level at -5.06 dB, which means that the highest levels obtained during measurements fall within the estimated limits set by Steinberg.

Overall, the measured and simulated data match well in terms of main lobe beam width and maximum side lobe level. This matching between the measured and simulated PSF indicates that good performance of CLEAN-PSF can be expected, as well as for CLEAN-SC. To further assess the performance and benefits of these deconvolution methods with respect to conventional beamforming as well as with respect to each other, a number of experiments with multiple sound sources (to create a more representative test scenario) were performed. The performance of the aforementioned methods (conventional beamforming, CLEAN-PSF and CLEAN-SC) was assessed and compared in terms of the ability to estimate the correct location and SPL of each source.

5.4.2. Test objective(-s), test setup and test conditions

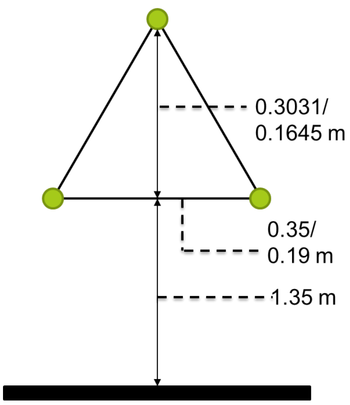

Figure 5.55: Multi source setup - model

As explained in Sections 2.3 and 5.4.1, the CLEAN-SC and CLEAN-PSF deconvolution methods do not only improve the quality of the source map, but also reflect on the performance of the array. This holds specifically for CLEAN-PSF, where deconvolution of the results is entirely based on the theoretical point spread function. The matching between simulated and measured PSF has been discussed for a single source, but a scenario where multiple sound sources are present is more representative for actual potential tests to be performed with the array system. The distribution of the sources is shown in Figure 5.55. Three sources were used in testing, where each source was set to emit a different broadband white noise signal, at a different power level. This experiment was repeated at two source separation distances, as indicated in the figure. The setup was located at a perpendicular distance of 1.5 meters from the array, with the center of the setup aligned with the center of the array.

Three different noise sources were available, two of which were simple speakers. The third speaker was the calibrated noise source, which was positioned in the top position as seen in Figure 5.55.

The actual setup is shown in Figure 5.56. Two of the noise sources were positioned on top of a frame, whereas the calibrated noise source was suspended from the ceiling, as done in previous experiments. This setup was chosen to minimize the potential interference from the mounting structure with the emitted signal. The volume settings were such that the sound source in the lower right emitted at the highest volume, followed by the source in the lower left, and finally the calibrated source at the top. Each source was set to emit broadband white noise. Again, the limited operating range of the calibrated noise source between 315 and 6300 Hz dictated the upper limit for which analysis could be performed.

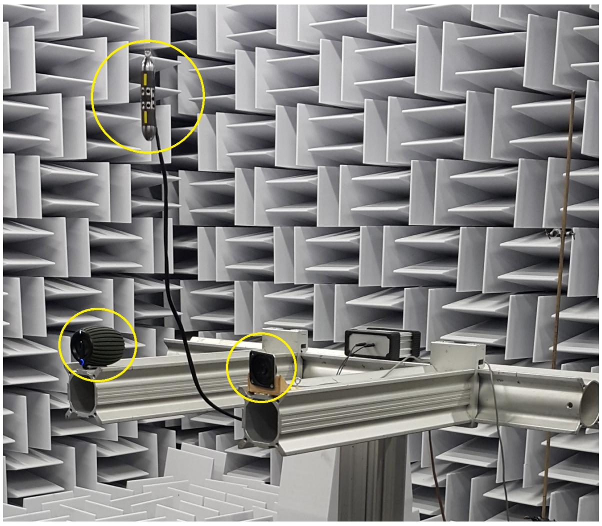

Figure 5.56: Multi source setup - actual

The atmospheric conditions in the wind tunnel at the time of testing are shown in Table 5.3.

Table 5.3: Atmospheric test conditions - calibration

Temperature (°C)	24.1
Pressure (Pa)	101102
Humidity (%)	54.42
Amplification setting (dB)	40 (unless indicated otherwise)

5.4.3. Test results

As established in the previous section, the goal is to assess and compare the performance of conventional beamforming, CLEAN-PSF and CLEAN-SC in terms of estimating the position and power of multiple sources. Since the spacing between the three sources is known (see Figure 5.55) as well as the diameter of the array and the perpendicular distance from the array to the source map, the frequency for which the Rayleigh limit corresponds to the distance between the sources can be calculated with Equation 2.68, by using Equation 2.69 to calculate θ_r. This is shown in Equation 5.3, with the required variables and results thereof displayed in Table 5.4.

$$f_{Rayleigh} = \frac{1.22c}{d\sin\left(\tan^{-1}\left(\Delta l / r\right)\right)} \tag{5.3}$$

Table 5.4: Rayleigh limit determination

Variable	**Value**	**Unit**
Horizontal distance array - source map	1.5	m
Array diameter	1.9	m
Speed of sound (in air)	345	m/s
Rayleigh limit frequency - $\Delta l = 0.19$	1760	Hz
Rayleigh limit frequency - $\Delta l = 0.35$	975	Hz

Given these expected lower limits, the obtained data was analyzed between 500 and 3000 Hz, as to ensure coverage of a sufficiently large frequency range to be able to compare the given methods.

The analysis itself was performed as follows. A search region was defined around each source location in the source map, within which the value and location of the maximum was identified. The height and width of this search region were defined as two-thirds the separation distance between the sources, both horizontally and vertically. The location obtained this way was subsequently compared to the known actual location of the source, and the offset was plotted over the given range of frequencies. The same could not be done with the estimated sound power levels, since the sound power of each source per frequency must be known for this. A solution was found by first recording each sound source separately. The obtained data was then analyzed by means of beamforming, and the maximum value per frequency was stored as the SPL of that source at that frequency. This way, the SPL of each single source could be compared to the SPL estimated when all three sources were emitting simultaneously. This is further exemplified by Figures 5.58 through 5.63.

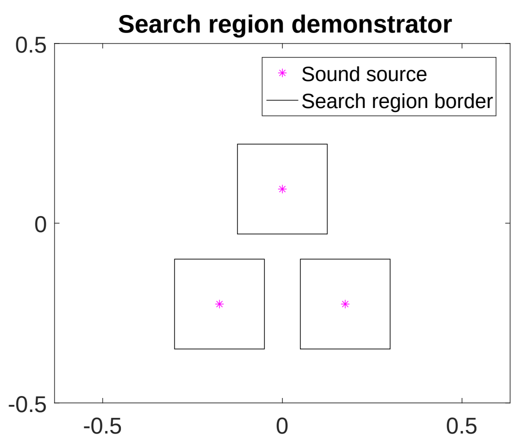

Figure 5.57: Source search regions explained

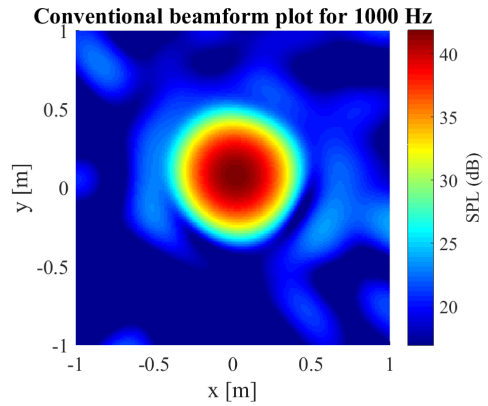

Figure 5.58: Conventional beamforming result - top source, $\Delta l = 0.35$

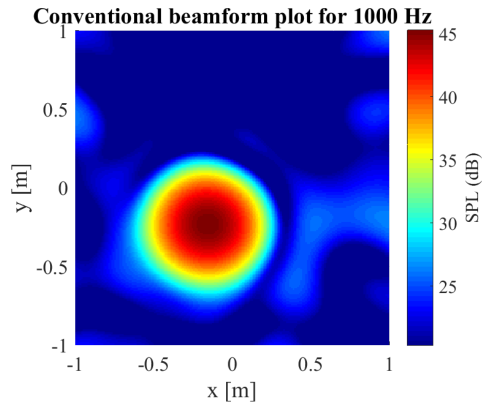

Figure 5.59: Conventional beamforming result - lower left source, $\Delta l = 0.35$

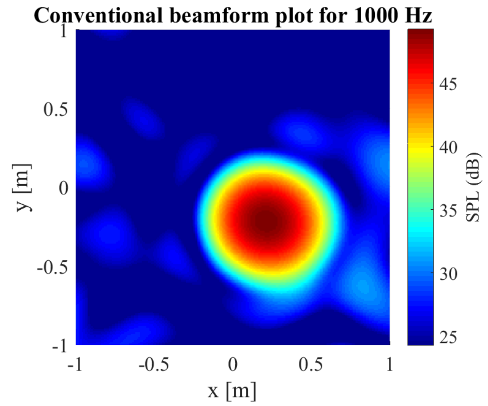

Figure 5.60: Conventional beamform result - lower right source, $\Delta l = 0.35$

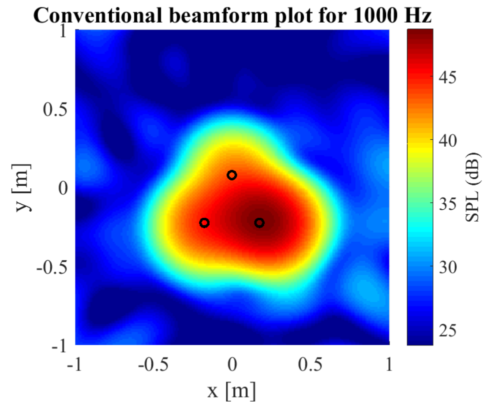

Figure 5.61: Conventional beamform result - all sources, $\Delta l = 0.35$

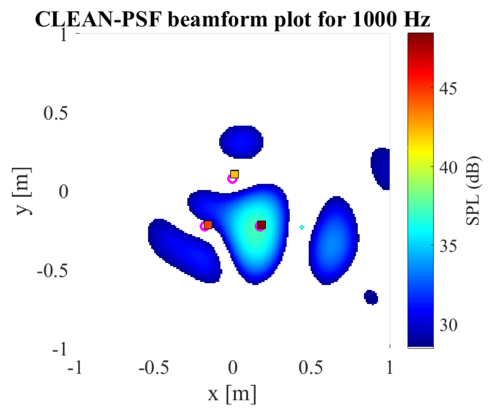

Figure 5.62: CLEAN-PSF beamform result - all sources, $\Delta l = 0.35$

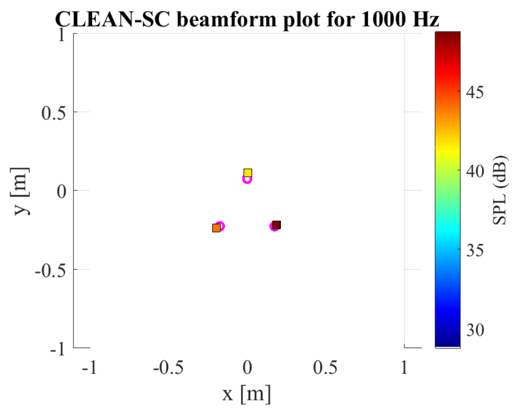

Figure 5.63: CLEAN-SC beamform result - all sources, $\Delta l = 0.35$

As explained in the objective explanation, the three sources are set to emit incoherent broadband white noise, but at different levels. Figures 5.58 through 5.60 indicate the level of each source, the lower right emitting at the highest power and the top source at the lowest.

The resulting differences between actual and measured values for both position and SPL were determined over the given range of frequencies between 500 and 3000 Hz, with a frequency resolution of 20 Hz. The results in terms of source position localization are shown in Figures 5.64 through 5.69.

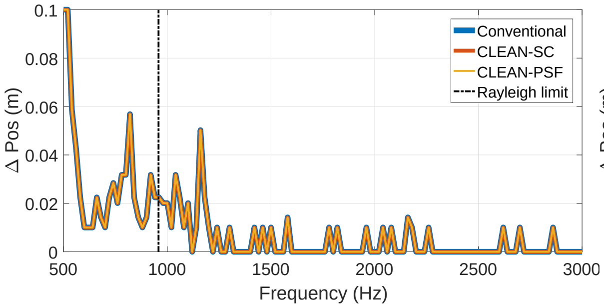

Figure 5.64: Position estimation - lower right source, far spacing

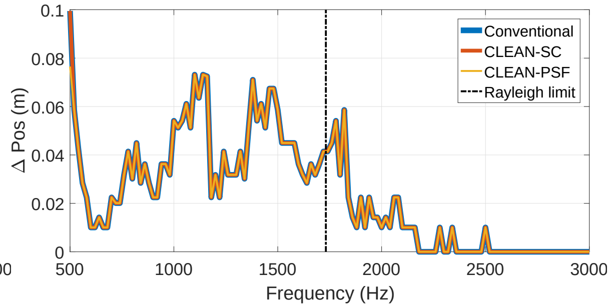

Figure 5.65: Position estimation - lower right source, close spacing

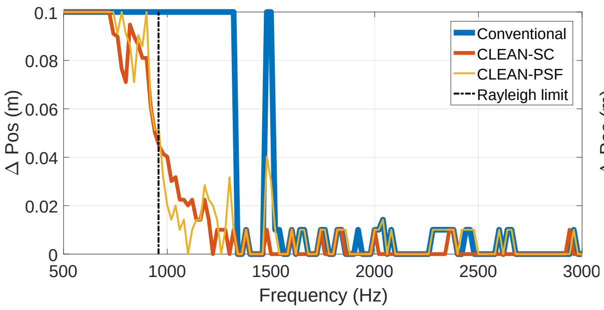

Figure 5.66: Position estimation - lower left source, far spacing

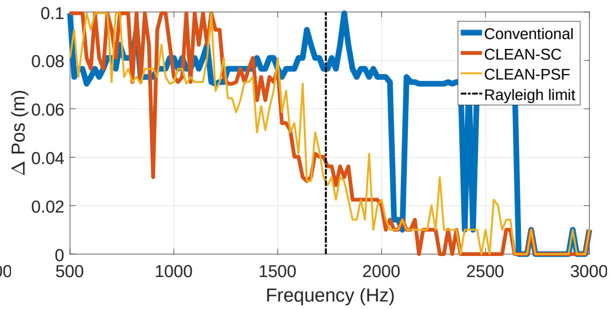

Figure 5.67: Position estimation - lower left source, close spacing

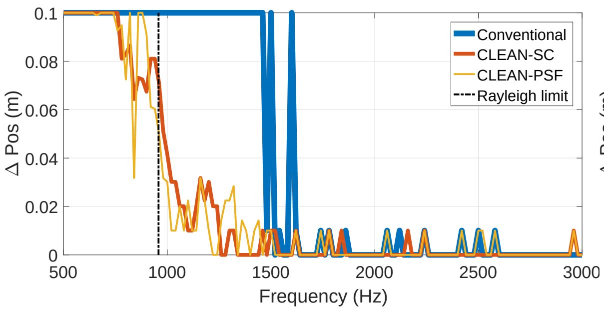

Figure 5.68: Position estimation - top source, far spacing

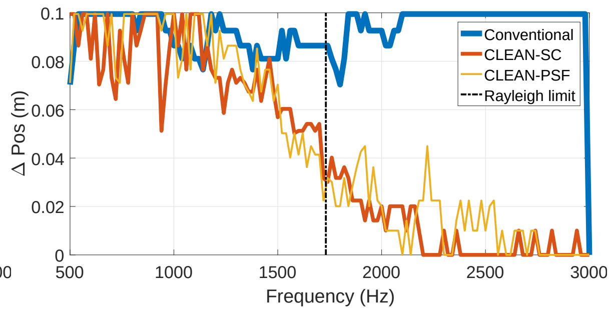

Figure 5.69: Position estimation - top source, close spacing

Sources estimated at locations further away than 10 centimeters from the actual position are regarded as incorrectly identified. This is reflected in the upper limits in Figures 5.65 through 5.69.

The most powerful source is detected with equal accuracy regardless of source spacing or the method used, hence the perfect overlap of all three lines. The sources emitting at lower levels however show a difference in accuracy between methods used. As expected, both CLEAN methods perform better than conventional beamforming in identifying the position of each weaker source. CLEAN-PSF and CLEAN-SC show comparable performance in identifying the positions of the individual sound sources. As discussed before, the good performance of CLEAN-PSF is especially interesting, since this indicates a good match between the theoretical and actual PSF. This signifies good array performance in terms of being able to obtain measurement data clearly and accurately, as well as accurate knowledge on the microphone positions. The source emitting at the lowest power is the hardest to detect in terms of position when placed close to the other two, but this decreases when the distance between sources is enlarged.

The results in terms of sound power level estimation are shown in Figures 5.70 through 5.75.

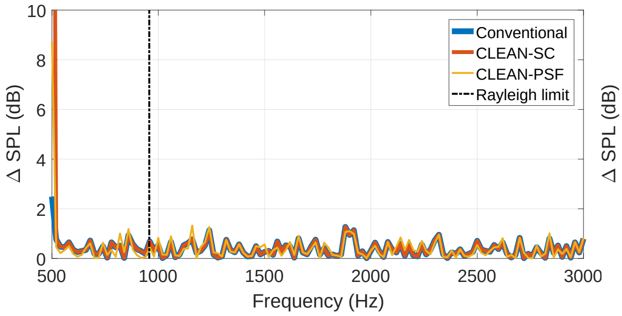

Figure 5.70: SPL estimation - lower right source, far spacing

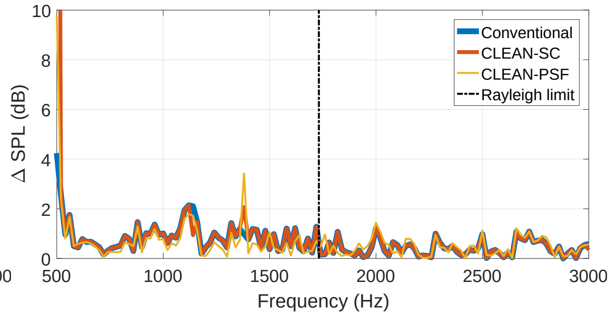

Figure 5.71: SPL estimation - lower right source, close spacing

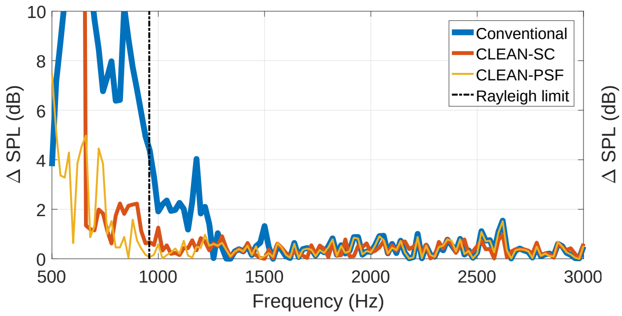

Figure 5.72: SPL estimation - lower left source, far spacing

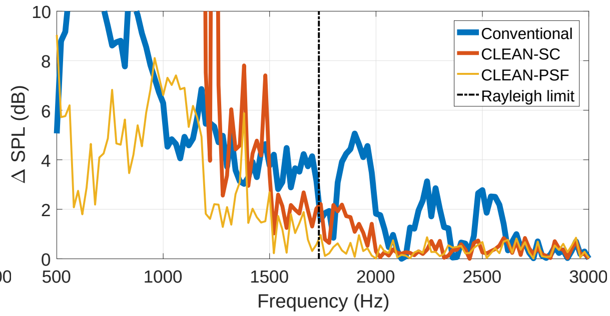

Figure 5.73: SPL estimation - lower left source, close spacing

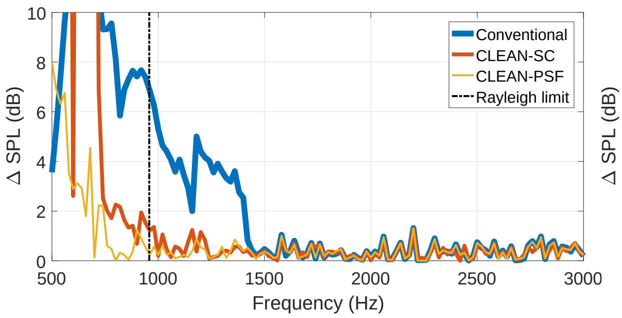

Figure 5.74: SPL estimation - top source, far spacing

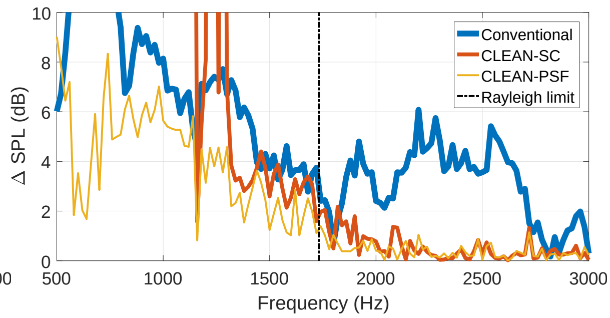

Figure 5.75: SPL estimation - top source, close spacing

Sources estimated at levels deviating more than 10 dB from the actual value are regarded as incorrectly identified. This is reflected in the upper limits in Figures 5.70 through 5.75.

Again, both CLEAN methods outperform conventional beamforming. For close spacing, CLEAN-PSF seems to be slightly more accurate at estimating sound power levels for frequencies close to the calculated Rayleigh limit compared to CLEAN-SC, but the results obtained with both methods are comparable at higher frequencies, for both the close and far source spacing situations.

5.4.4. Conclusion and recommendation

The ability to distinguish multiple point sources is clearly enhanced by using a deconvolution technique such as CLEAN-PSF and CLEAN-SC. Both perform significantly better than the conventional delay-and-sum approach, but additional computation time is required.

Under the given test situations, the accuracy with which the location of a noise source was estimated varies between 6 centimeters from the actual position close to the Rayleigh limit to 2 centimeters from the actual position for frequencies further from this limit. This was possible with both CLEAN-PSF and CLEAN-SC, whereas conventional beamforming proved much less accurate, especially for closely spaced sources. Estimations of the SPL of the source were accurate within 2 dB near the Rayleigh limit, and within 1 dB further away from the limit, again excluding the results obtained with conventional beamforming.

The performance of CLEAN-SC with respect to CLEAN-PSF is discussed further in the next section.

5.5. Deconvolution method assessment - low signal-to-noise ratio

Due to the differences in approach taken to clean the source map, CLEAN-SC is expected to provide a better result than CLEAN-PSF when low signal-to-noise ratios are concerned. This was tested by recording the signal emitted by two sources, separated by a small distance, set to emit at a lower power level than in the previously discussed experiments.

5.5.1. Test objective(-s), test setup and test conditions

The objective of this test series is to assess the performance of conventional beamforming compared to CLEAN-PSF and CLEAN-SC at relatively low signal-to-noise ratios.

Figure 5.76 shows the setup used for this series of experiments. The calibrated noise source (the top source) and a second source (the bottom source) were mounted to a vertical pole, separated at a distance of 0.25 meters. This setup was positioned at a horizontal distance of 2.32 meters from the array, the point between the two speakers aligned with the center of the array both vertically and horizontally. The second source used in this experiment series was the same as used in the previous experiments (the source positioned in the lower right, see Figure 5.56).

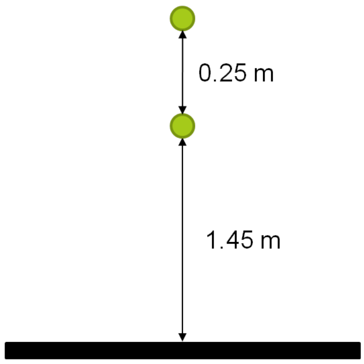

Figure 5.76: Multi source setup - model

The amplification setting of the calibrated noise source was varied over a range between 5 and 40. An amplification power setting of 40 was used in the previous experiment series (Section 5.4), since the QindW source was calibrated at this setting. The second sound source output volume was chosen such that it was close to the calibrated source output level for each of the given settings, to ensure that the difference in SPL between the two was relatively small. However, without accurate calibration data on the secondary source, this could not be matched exactly to the calibrated source.

The atmospheric conditions during this test series are displayed in Table 5.5.

Table 5.5: Atmospheric test conditions - calibration

Temperature (°C)	24.2
Pressure (Pa)	101101
Humidity (%)	55.13

Again, Equation 5.3 was used to determine the minimum separation frequency according to the Rayleigh criterion, using the data from Table 5.6.

Table 5.6: Rayleigh limit determination

Variable	**Value**	**Unit**
Horizontal distance array - source map	2.32	m
Array diameter	1.9	m
Speed of sound (in air)	346	m/s
Rayleigh limit frequency - $\Delta l = 0.25$	2067	Hz

An appropriate frequency range for analysis was determined between 2200 and 4000 Hz, with a frequency resolution of 20 Hz. Different from the previous section, where a search region was defined within which to find the location and value of the maximum, the source maps themselves are analyzed to assess the performance of CLEAN-SC and CLEAN-PSF.

The first source maps to be analyzed were recorded at an amplifier setting of 20, over the entire band between 2200 and 4000 Hz with a resolution of 25 Hz, by first calculating the autopower matrix per individual frequency using conventional beamforming, then applying the appropriate deconvolution method to obtain the deconvoluted autopower matrices per frequency, and subsequently summing these for the given range. These are shown in Figures 5.77 and 5.78 for CLEAN-PSF and CLEAN-SC, respectively. The signal-to-noise ratio per case is calculated by measuring the background noise for each experiment, and subsequently comparing the experiment data to this background noise for the given frequency range.

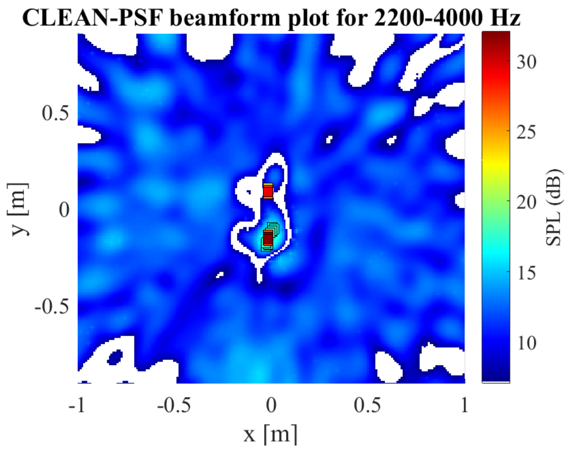

Figure 5.77: Source map - CLEAN-PSF, amplification factor 20, S/N 10.6 dB

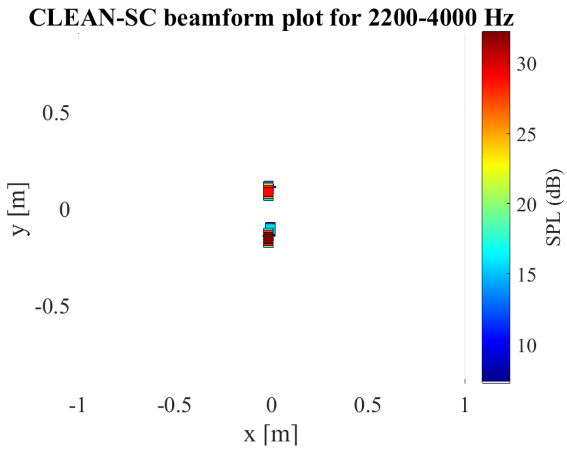

Figure 5.78: Source map - CLEAN-SC, amplification factor 20, S/N 10.6 dB

For clarity, the 15 largest points in the source map are enlarged, as shown by the square blocks in the source maps. For an amplification factor of 20, both methods estimate the location of the sources in the correct location. The main difference between the results is the fact that the remaining noise in the CLEAN-PSF source map is of a higher level than in the CLEAN-SC source map (the dynamic range of the plots is set such that values up to 25 dB lower than the maximum are shown. The white areas indicate points for which the estimated level is below this limit). This is less pronounced when the amplifier is set to 10.

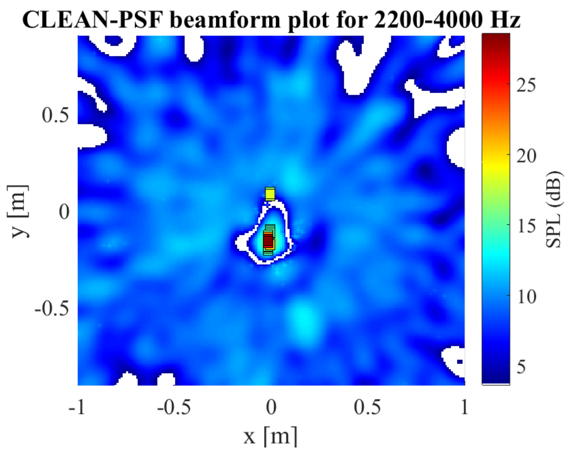

Figure 5.79: Source map - CLEAN-PSF, frequency band, amplification factor 10, S/N 3 dB

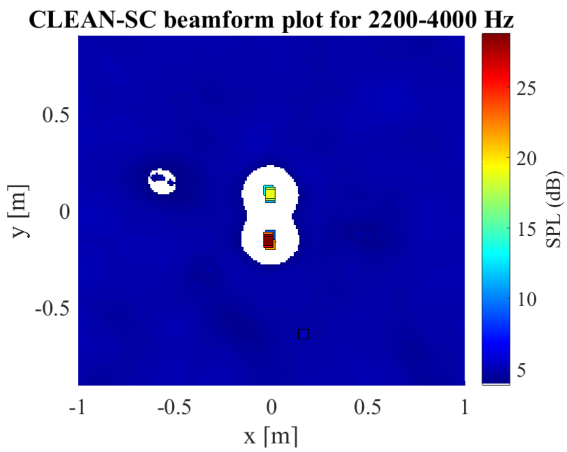

Figure 5.80: Source map - CLEAN-SC, frequency band, amplification factor 10, S/N 3 dB

In Figure 5.80, the remaining noise in the CLEAN-SC map has risen to levels visible within the dynamic range. Still, both methods estimate the position of the noise sources with sufficient accuracy. A large shift is seen when halving the power setting again.

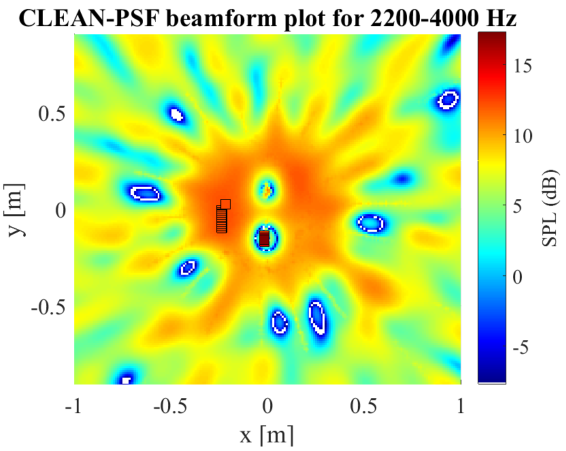

Figure 5.81: Source map - CLEAN-PSF, frequency band, amplification factor 5, S/N 1.7 dB

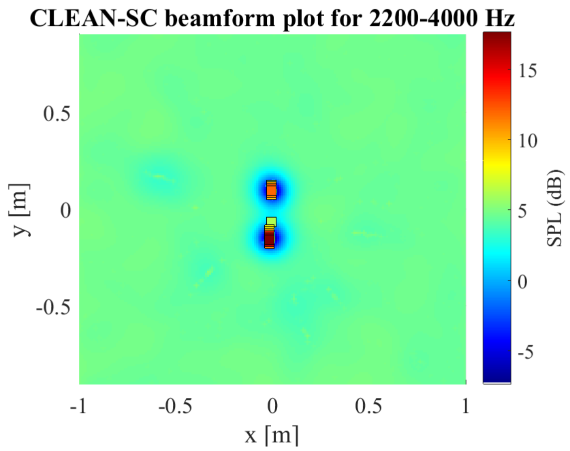

Figure 5.82: Source map - CLEAN-SC, frequency band, amplification factor 5, S/N 1.7 dB

In Figure 5.81, CLEAN-PSF is no longer able to correctly identify the top source, whereas CLEAN-SC still shows the ability to identify and locate two distinct sound sources. When looking at single frequency instances within the given band between 2200 and 4000 Hz, the cause of this effect is more pronounced.

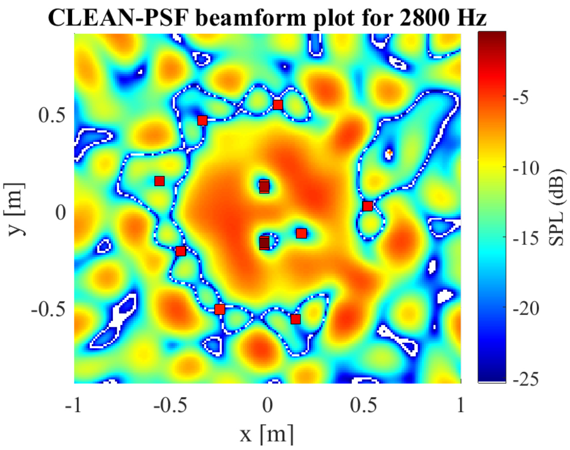

Figure 5.83: Source map - CLEAN-PSF, frequency instance at 2800 Hz, amplification factor 5, S/N 1.7 dB

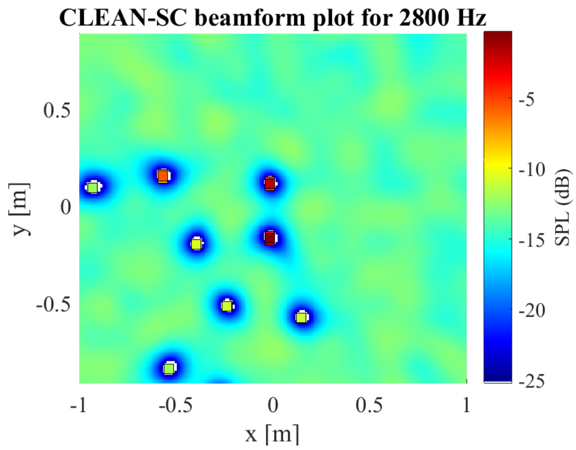

Figure 5.84: Source map - CLEAN-SC, frequency instance at 2800 Hz, amplification factor 5, S/N 1.7 dB

In Figure 5.84, there are clearly two strong sources at the center, whereas the third highest peak is estimated at 7 dB below either of the actual sound sources. In Figure 5.83, the two strongest sources are also located at the center, but these are surrounded by a large number of other potential source locations, all with an estimated SPL well within 5 dB of the source map maximum. This effect is not unique to the single frequency instance at 2800 Hz, but similar patterns are shown throughout the given frequency range. This erroneous identification of additional sound sources is what leads to the erroneous identification of the secondary source's position when a larger frequency band is considered (i.e. Figure 5.81). CLEAN-SC provides a more reliable estimation of actual noise source location and power, since the number and level of erroneously identified sources is lower. When adding these results for a larger range of frequencies, these erroneous sources are filtered out (i.e. Figure 5.82).

Since the actual source distribution is known, the information in Figures 5.83 and 5.84 is still useful; the SPL and location of the two center sources can be extracted from the plot for analysis. However, under regular experimental conditions, the source distribution is part of the research objective, and hence unknown. Therefore, using either CLEAN-PSF or CLEAN-SC under those conditions may lead to erroneous conclusions regarding source distribution and source power when low signal-to-noise ratios are concerned, due to the identification of a large number of strong side lobes as sound sources.

5.5.2. Conclusion and recommendation

At low signal-to-noise ratios, CLEAN-SC provides a cleaner and more reliable result than CLEAN-PSF for the same input data. This was tested and proven by using two point sources in relatively close proximity over a range of output power levels, and subsequently treating the obtained data with both deconvolution methods. This means that the outcome of this experiment is limited to point sources, and for a frequency range beyond the lower limit indicated by the Rayleigh criterion. Sijtsma[58] discusses the fact that CLEAN-SC is not well suited for closely spaced sources, and by extension distributed sources, due to the assumption that the source map is built up of PSF's. Since the added processing time required for CLEAN-SC is relatively small, CLEAN-SC is the suggested approach to data analysis with this array for distributed point sources. A high-resolution improvement to CLEAN-SC (not considered in this thesis) has recently been proposed by Sijtsma[59], which offers even better results.

6

Array evaluation

This chapter contains the evaluation of the array, subdivided into discussions per aspect of the process. The initial considerations of practicality, acoustic performance and flexibility are revisited, as well as the improvements made in the meantime. Finally, several suggested improvements are discussed, which may be applied in the future to further improve the system.

6.1. Practicality

First of all, the practicality of the system as a whole is discussed. Over the course of this project, the array has already been used to perform measurements and experiments. As explained in Section 5.3, this thesis project was performed in conjunction with the thesis work by S. Luesutthiviboon[32], which was focused on testing the performance of different array distributions. Aside from that project, experiments were performed for the analysis of the effect of porous materials in the production of airfoil trailing edge noise[52], and another series of experiments were performed to assess the effect of rotor shrouds on noise production. This proved to be advantageous for the assessment of both practicality and flexibility; the entire array system was used by different people for different purposes, and each measurement campaign resulted in new feedback on the system, analyzing both the strengths of the system and potential improvements. Most improvements were made to the software, which was caught short in some fields, and the small changes required to improve upon this were implemented immediately. The array itself proved to be practical in use, and can be operated without the requirements of additional tools and with a very straightforward and self-explanatory user interface. Data acquisition, storage and conversion to Matlab has all been automated, and is deemed complete. The software was kept concise, such that future improvements and changes can be made with ease.

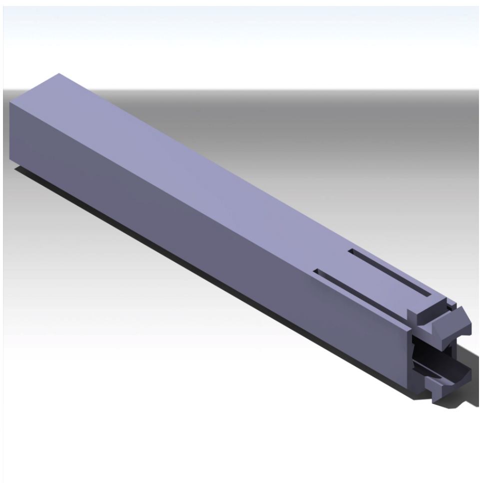

Figure 6.1: Concept microphone holder

Improvements were identified mostly in the process concerning the (re-)configuring of the microphone distribution. This operation is by far the most lengthy part of the array setup, and can be improved upon, mainly by changing the way in which microphone holders are mounted. For now, the holders are clamped to the array plates by means of two simple nuts on either side of the plate. Placing and removing these holders is therefore optimally performed with two people, one on either side of the array. To enable a single person to swap configurations with ease, a new holder placement system was considered, with a different clamping system. A concept design for an improved holder is shown in Figure 6.1, consisting of a square frame with a cylindrical inner compartment for microphone placement. This holder would be fastened to the plate by means of the two flexible clips on either side on the front of the holder.

Fastening this concept holder would be done by simply clicking the holder in place from the back of the array, without the need of an additional person to fasten it at the front. Removing would be equally simple, just by pressing the two sides of the clip together. These holders can be manufactured by means of 3D printing, for which a quote was obtained. Single samples would cost around 6 euros, and larger batches would reduce the price per sample such that 80 holders can be obtained for less than 100 euros (as quoted by Oceanz[44]). Depending on the expected number of reconfigurations during the lifetime of this array, such a small investment may be worth the price for the amount of time and effort it will save.

Another potential point of improvement is the routing of cables from the array to the data acquisition system. Compared to the situation at the start of the project, this has already undergone immense improvements by bundling, numbering and distributing the cables in an orderly fashion. However, to prevent tension on the parts that connect the microphones to the cables, the pull of the cable bundles should be reduced as much as possible. This can be achieved by mounting a tray along the top of the array, through which the cables are routed, thus preventing the pull of gravity from damaging the system. This would improve the lifespan of the array, hence increasing its practicality.

In terms of transportability and storability of the array, the modular design allows the structure to be moved and stored in parts. This also increases the ease with which components can be replaced, either when broken or when better alternatives are available.

6.2. Acoustic Performance

The acoustic performance of the array is discussed elaborately in the chapter dedicated to array testing (Chapter 5). In the end, the array has not been tested for the complete span of the initially indicated frequency range of interest between 500 and 8000 Hz (Section 3.3.2), since the upper frequency region of this range was outside the operating range of the calibration source. According to the Phong and Papamoschou model used for predicting the acoustic performance of perforated plates, this upper frequency region is expected to exhibit a larger reflection coefficient, and therefore is expected to exhibit more interference than the currently evaluated frequency range. The array has been calibrated in third octave bands and shows to provide a very accurate noise source position estimation. As for estimating the sound power level (or power watt level, PWL) of these sources, the system has been proven to provide an estimation of the level in third octave bands within 2 dB of the calibrated value of the source. Since the range of frequencies over which this calibration could be performed was heavily restricted by the rated performance range of the source, as well as by the fact that said source was calibrated in third octave bands, a higher accuracy in terms of frequency resolution and -range could not be obtained. However, the calibration process has resulted in the identification and mitigation of one of the main sources of (both constructive and destructive) interference due to reflections, being the center part of the array. This was solved by covering this component with Flamex standard acoustic foam, which showed a significant improvement.

The choice of beamform method to use when processing data obtained with the array depends on the expected distribution of sources. Conventional beamforming can provide a good initial estimation of the location and level of noise sources, whereas CLEAN-SC shows a large improvement in the identification of individual noise sources, both in terms of position and level. For closely spaced sources and distributed sources, using any PSF-based deconvolution method (e.g. CLEAN-SC and CLEAN-PSF) might result in the misrepresentation of multiple noise sources as one. Both CLEAN-SC and CLEAN-PSF exhibited the ability to detect multiple individual noise sources, emitting at different levels, spaced both far apart and closely together. However, since the processing time required for both methods is comparable, the use of CLEAN-SC is recommended considering the cleaner result it provides. Especially at low signal-to-noise ratios, CLEAN-SC shows a clear improvement over CLEAN-PSF in accuracy and noise reduction.

The aforementioned other experiment campaigns that made use of this array also resulted in accurate and satisfactory results, further affirming the acoustic performance of the system.

6.3. Flexibility

Each plate in the current array allows for 8580 possible microphone positions. The number of possible distributions of 64 microphones is therefore nearly infinite. The position of each microphone is known to the millimeter, which improves the precision with which the steering vectors can be formulated. The maximum aperture of a circular distribution across the array is 1.9 meters due to the maximum height restriction. If an elliptical distribution is used, the maximum width of the distribution is 2.9 meters using the three plate configuration, increasing the resolution in the horizontal direction according to the Rayleigh criterion.

The main test of array flexibility was found in the work by S. Luesutthiviboon[32], on the testing of the performance of different microphone distributions across the array. Since he was able to test multiple configurations with relative ease, and obtain satisfactory results around which to base his research conclusion, the flexibility of the array is proven to be sufficient for the support of multiple research-specific configurations.

6.4. System evaluation

All in all, the array is proven to be effective and accurate within the frequency range for which calibration was possible, and for the multi-configuration support purpose for which it was intended. Accurate and acceptable calibration was obtained after slight modifications to the array, by applying acoustically absorbent foam to a critical component. The system is practical in all facets of its employment, but the placement and reconfiguration of microphone distributions can be improved upon with the suggested change in microphone holders.

A number of weaknesses is still present in the system as a whole, mainly in the data acquisition system. The fan noise generated by the data acquisition system is one of these weaknesses, and requires some form of shielding of the DAS from the array. During this project, this was solved by placing the DAS in a different room than the array. Other weaknesses (as discussed in Section 4.2) lie in the internal hardware of the DAS, as well as the configuration of the storage system. Providing an enclosed rack for the DAS would solve a number is issues, but the internal hardware cannot be changed, and hence solutions had to be found externally, e.g. by controlling the system remotely, and storing data on an external hard drive when the internal storage configuration malfunctions. Although less than ideal, the issues discussed so far were not detrimental to the recorded data.

As discussed previously, two of the three main array objectives are best measured by the use of the array system for ongoing research projects. The fact that execution of the required experiments for such a diversity of research objectives was possible with this newly created array (even while it was still in development), combined with the fact that these experiments yielded adequately accurate data for satisfactory results, should be reflected in determining the overall array performance. Therefore, based on personal experience as well as the employment of the system by these other researches, the conclusion can be drawn that the array fulfills its initial design objectives of practicality, acoustic performance and flexibility, whilst leaving room for improvement in the areas indicated before.

7

Conclusions and Recommendations

This chapter entails the conclusions and recommendations of this thesis project as a whole. This includes all facets of the project, as well as the final outcome. Based on this outcome, a number of recommendations is made for further research in the same field, as well as a number of suggested improvements to the current system.

7.1. Conclusions

The final outcome of this thesis project is a practical and flexible acoustic array system, proven to provide reliable and accurate estimations of source position and sound pressure/power level over for a given third octave band frequency range. The array structure consists of a set of perforated plates, featuring a square perforation pattern to achieve the highest possible plate porosity within the range of industrial standard patterns. These plates are mounted to a frame which provides not only structural support, but also raises the plates such that the center of the array is aligned with the average test section (since the actual height of the test section varies per setup, and is highly dependent on the chosen wind tunnel nozzle, the average height of 1.5 meters was chosen as a design objective). The array can be configured with two or three plates, spanning either 2 by 2 or 3 (horizontal) by 2 (vertical) meters.

The resulting array structure allows for the straightforward and practical placement of any microphone distribution, up to a vertical spacing of 1.9 meters, and a horizontal spacing of up to 2.9 meters. Since most microphone configurations are based on a distribution across a square platform, the 2 by 2 meter configuration was used throughout this project. Microphones can be placed in the array by means of mounting a microphone holder, which provides structural support to the microphone as well as ensuring its perpendicularity to the source map.

The array system was tested by first performing quantification tests on the anechoic test chamber for which the array was designed. The range at which free-field propagation could be assumed was identified, and the reverberation time was measured to be sufficient for the chamber to be regarded as anechoic. The lower frequency bound of the materials and shapes used to provide this anechoic quality was determined at 500 Hz, dictating the lower bound for which analysis could be performed under the anechoic condition assumption.

Following this quantification, the array was calibrated using a QindW sound source, with a stable operating regime between 315 and 6300 Hz. The initial array calibration tests identified one region (the center of the array) specifically as the cause of interference, which was solved by applying Flamex standard acoustically absorbent foam onto that region. This reduced the previously observed interference considerably, and allowed for accurate calibration of the system. Since the actual directivity of the sound source along its principal axis is unknown, the directivity factor was estimated to lie between 1 and 2 based on the shape of the sound source.

This factor was subsequently calculated by minimizing the difference between calibrated and measured sound power levels, and was found to be 1.4825, well within the expected range. With this directivity factor (corresponding to a directivity index of 1.71 dB), the array was determined to provide sound power estimations with an accuracy of 1.5 dB for the third octave bands within the rated operating regime of the sound source (500-5000 Hz third octave bands). The location of the source was accurately estimated within 1 centimeter of its actual position in these tests.

In order to verify the assumed directionality of the sound source along its principal axis, additional tests on the sound source will have to be performed. For other products of the sound source manufacturer, the directivity index of said product is determined in third octave bands, but this was not done yet for the QindW source. This will be necessary in order to accept the conclusions on accuracy of the array.

Once the array was known to provide accurate results (under the assumed source directionality), the optimal approach to post-processing was identified by testing conventional (delay-and-sum) beamforming, as well as deconvolution methods CLEAN-PSF and CLEAN-SC. These methods were chosen based on their performance compared to other deconvolution techniques[11]. Additionally, since both methods are based on the initially measured PSF, their performance is a direct indication of the quality with which the array can obtain data, as well as the accuracy with which the microphone positions are known (this holds especially for CLEAN-PSF). The optimal method was chosen based on the accuracy with which the power and location of a sound source could be determined when multiple sound sources were concerned. Whereas CLEAN-PSF and CLEAN-SC both provide a clear improvement over conventional beamforming, CLEAN-SC was found to grant much better results for lower signal-to-noise ratios than the CLEAN-PSF counterpart. CLEAN-SC is therefore the suggested method when multiple individual incoherent sources are considered. For distributed or closely spaced sources, this method is less reliable, and an alternative must be used. The accuracy with which the location of a sound source can be estimated in a multi-source scenario depends on the relative power of that source, but with the use of deconvolution methods CLEAN-PSF and CLEAN-SC, an accuracy of 2 centimeters can be achieved for a multi-source setup for frequencies sufficiently beyond the Rayleigh limit. Closer to the Rayleigh limit, this accuracy may decrease to within 6 centimeters of the actual source position. The emitted power of the source was estimated within 2 dB of the actual value.

The array system has been used for other means than this project alone over the course of this thesis work, which enabled the gathering of feedback from different users on the system. Based on this feedback, the control software was tailored and extended to be as complete and accurate as possible, whilst also remaining concise. No changes were made to the array, apart from improvements to enhance acoustic performance.

7.2. Recommendations

Based on the feedback received from other users of the array, the main point of improvement would be the microphone placement method. A new concept design was made for the microphone holders, as shown in Figure 6.1, to improve on this point. A secondary point of improvement is to construct the array out of a non-corroding material, or coating the current structure. The current array consists of steel perforated plates, which already show slight traces of corrosion. These plates were chosen mainly for their rapid availability. Using stainless steel or coating the current plates might help in solving this issue, but the thickness of the coating must be such that the microphone holders still fit within the perforations in the plate. Apart from these points, no immediate shortcomings of the array were identified. The data acquisition system, on the other hand, does have a number of unresolved issues.

First and foremost, the noise generated by the system has been discussed in previous chapters. The suggested approach to solving this issue is to mount the system into an enclosed rack. As long as the chosen rack features sufficient space and cooling capabilities, as well as an opening to feed the microphone connector cables through, this is by far the simplest and most straightforward solution. However, construction plans for the wind tunnel show the placement of a small office in the anechoic test chamber, as shown in Figure 7.1. If this is built, it would be perfect for housing the DAS.

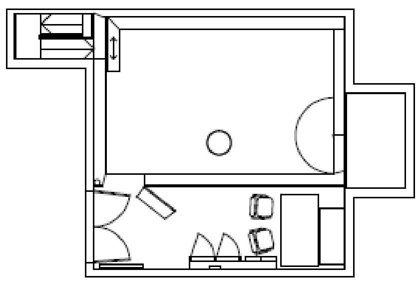

Figure 7.1: Anechoic test chamber floor plan with office space

At the time of writing, the DAS also shows a calibration offset. Multiple channels record a nonzero average voltage, even when nothing is connected to said channel. The exact cause of the issue is unknown, and a solution is being sought after in cooperation with National Instruments™. The offset takes a short while (15 to 20 minutes, on average) to stabilize, at which point measurements can be taken and subsequently corrected in post-processing. This means that the system is still usable, but the situation is less than ideal, and must be solved.

Since the controller has a number of downsides, for example in RAID configuration method, graphics processing capability and the aforementioned noise, it might be wise to build a different controller. The required PCIe card for communication with the PXI chassis was included with the purchase of the system, and can be built into a less noise and more capable computer to serve as a controller. If this computer comes equipped with sufficiently fast and large storage capability (preferably with SSD's instead of HDD's), and a graphics processor capable of handling LabVIEW, these issues may be resolved.

The final layout and configuration of the wind tunnel has not been applied during this project. The tunnel is nearing this point though, and when it does, the quantification tests should be re-executed for the final configuration. Since one of the upcoming changes in test chamber configuration involves raising the floor by a small amount, the alignment of the center of the array with the height of the average test section may no longer apply.

Finally, the sound source used for calibrating the array only provided reliable performance in a relatively small frequency range, and was calibrated in third octave bands. Additionally, the directivity of the source is unknown. To perform a more accurate calibration over a wider frequency range, a different sound source is required, preferably calibrated in smaller frequency bands. Additionally, although the current sound source does allow for external input (e.g. by using a function generator), the output power of external signals is not stable, and seems to vary more as the amplifier becomes warmer. Having a source that supports this feature in a stable manner would expand the application region of said source. If such as sound source becomes available, the applicability of the Phong and Papamoschou perforated plate reflection model can also be tested.

A

Appendix A - Wave equation

A.1. Wave equation - basic principles

The derivation of the wave equation in this section is based on the derivation obtained from course material at the Delft University of Technology [60]. The wave equation can be derived from three basic principles in physics:

- Conservation of mass
- Conservation of momentum
- Conservation of energy

A.1.1. Conservation of mass

The conservation of mass stipulates that the change of mass in a given volume must be the sum of the inflow and the outflow of mass of that volume. This can be expressed as shown in Equation A.1. Remember that x_1 corresponds to the x-direction, x_2 corresponds to the y-direction and x_3 corresponds to the z-direction.

$$\frac{\partial \rho}{\partial t} + \frac{\partial}{\partial x_1}(\rho v_1) + \frac{\partial}{\partial x_2}(\rho v_2) + \frac{\partial}{\partial x_3}(\rho v_3) = 0 \tag{A.1}$$

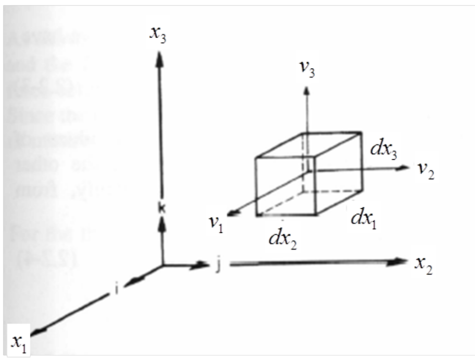

Figure A.1: Conservation of mass

Figure A.1 further illustrates the conservation of mass for a given volume. Having established this first equation, consider very small values for v_1, v_2 and v_3. Additionally, consider the small variation of density ρ', which can be expressed as $\rho = \rho_\infty + \rho'$. Combining these two factors allows to rewrite Equation A.2, as shown in Equation A.2.

$$\begin{aligned}
0 &= \frac{\partial \rho}{\partial t} + \frac{\partial}{\partial x_1}(\rho v_1) + \frac{\partial}{\partial x_2}(\rho v_2) + \frac{\partial}{\partial x_3}(\rho v_3) \\
&= \frac{\partial(\rho_\infty + \rho')}{\partial t} + \frac{\partial}{\partial x_1}((\rho_\infty + \rho')v_1) + \frac{\partial}{\partial x_2}((\rho_\infty + \rho')v_2) + \frac{\partial}{\partial x_3}((\rho_\infty + \rho')v_3) \\
&= \cancel{\frac{\partial \rho_\infty}{\partial t}} + \frac{\partial \rho'}{\partial t} + \frac{\partial}{\partial_{x_1}}(\rho_\infty v_1 + \cancel{\rho' v_1}) + \frac{\partial}{\partial_{x_2}}(\rho_\infty v_2 + \cancel{\rho' v_2}) + \frac{\partial}{\partial_{x_3}}(\rho_\infty v_3 + \cancel{\rho' v_3}) \\
&= \frac{\partial \rho'}{\partial t} + \frac{\partial}{\partial x_1}(\rho_\infty v_1) + \frac{\partial}{\partial x_2}(\rho_\infty v_2) + \frac{\partial}{\partial x_3}(\rho_\infty v_3) \\
&= \frac{\partial \rho'}{\partial t} + \rho_\infty \nabla \vec{v}
\end{aligned} \tag{A.2}$$

Important assumptions in this derivation are that $\frac{\partial \rho_\infty}{\partial t} = 0$, since ρ_∞ is constant. Additionally, since both ρ' and v are small, the product of the two can be considered negligible, i.e. $\rho' v \approx 0$.

A.1.2. Conservation of momentum

The conservation of momentum dictates that the sum of forces between two interacting particles must be zero, and is based on Newton's third law. Based on the Euler equations, the required form of the momentum conservation equation can be derived.

$$-\frac{1}{\rho}\frac{\partial p}{\partial x_i} = \frac{dv_i}{dt} = \frac{\partial v_i}{\partial t} + \frac{\partial v_i}{\partial x_1}v_1 + \frac{\partial v_i}{\partial x_2}v_2 + \frac{\partial v_i}{\partial x_3}v_3 \tag{A.3}$$

Again, considering a small v_i, small p' (expressed as $p = p_\infty + p'$) and small ρ' (expressed as $\rho = \rho_\infty + \rho'$), this equation can be adapted.

$$\begin{aligned}
i &= 1,2,3 \\
-\frac{1}{\rho}\frac{\partial p}{\partial x_i} &= \frac{dv_i}{dt} \\
-\frac{1}{\rho_\infty + \rho'}\frac{\partial(p_\infty + p')}{\partial x_i} &= \frac{dv_i}{dt} \\
-\cancel{\frac{\partial p_\infty}{\partial x_i}} - \frac{\partial p'}{\partial x_i} &= \rho_\infty \frac{dv_i}{dt} + \cancel{\rho' \frac{dv_i}{dt}} \\
\rho_\infty \frac{dv_i}{dt} + \frac{\partial p'}{\partial x_i} &= 0 \\
\rho_\infty \frac{d\vec{v}}{dt} + \nabla p' &= 0
\end{aligned} \tag{A.4}$$

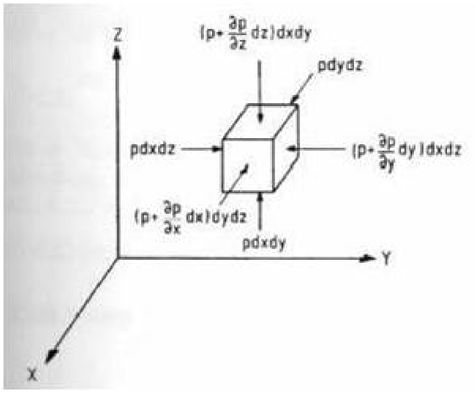

Figure A.2: Conservation of momentum

The basis on which parts of Equation A.4 are struck off are the same as mentioned in Section A.1.1.

A.1.3. Conservation of energy

For the conservation of energy, the isentropic flow property as shown in Equation A.5 must be used.

$$\frac{p}{\rho^{\gamma}} = constant \tag{A.5}$$

Again, considering a small p' (expressed as $p = p_{\infty} + p'$) and small ρ' (expressed as $\rho = \rho_{\infty} + \rho'$), this equation can be adapted.

$$\begin{aligned} \frac{p}{\rho^{\gamma}} &= \frac{p_{\infty}}{\rho_{\infty}^{\gamma}} \\ \frac{p_{\infty} + p'}{(\rho_{\infty} + \rho')^{\gamma}} &= \frac{p_{\infty}}{\rho_{\infty}^{\gamma}} \\ 1 + \frac{p'}{p_{\infty}} &= \left[1 + \frac{\rho'}{\rho_{\infty}}\right]^{\gamma} \end{aligned} \tag{A.6}$$

The final result can be linearized, as shown in Equation A.7.

$$\begin{aligned} 1 + \frac{p'}{p_{\infty}} &= \left[1 + \frac{\rho'}{\rho_{\infty}}\right]^{\gamma} \\ 1 + \frac{p'}{p_{\infty}} &= 1 + \frac{\gamma\rho'}{\rho_{\infty}} + \cancel{\frac{\rho'^2(\gamma-1)\gamma}{2\rho_{\infty}^2} + \ldots} \\ p' &= \gamma\frac{p_{\infty}}{\rho_{\infty}}\rho' \end{aligned} \tag{A.7}$$

Since ρ' was assumed to be very small, all higher powers of ρ' can be considered to be equal to zero, which is why all higher powers of the linearization can be struck off. When considering an ideal gas, the speed of sound is expressed as shown in Equation A.8.

$$c^2 = \gamma\frac{p_{\infty}}{\rho_{\infty}} = \gamma RT \tag{A.8}$$

This can be put into the result of the derivation shown in Equation A.7.

$$p' = c^2\rho' \tag{A.9}$$

Due to the nature of the assumptions made, this only holds for isentropic processes and ideal gasses.

A.2. Wave equation derivation

The equations obtained so far are:

$$\frac{\partial \rho'}{\partial t} + \rho_\infty \nabla \vec{v} = 0 \tag{A.10}$$

$$\rho_\infty \frac{d\vec{v}}{dt} + \nabla p' = 0 \tag{A.11}$$

$$p' = c^2 \rho' \tag{A.12}$$

These can be combined to form the wave equation, as shown in Equation A.13.

$$\begin{aligned}
\frac{\partial \rho'}{\partial t} + \rho_\infty \nabla \vec{v} &= 0 \\
-\nabla p' \left(\frac{d\vec{v}}{dt}\right)^{-1} &= \rho_\infty \\
\frac{\partial \rho'}{\partial t} - \nabla p' \left(\frac{d\vec{v}}{dt}\right)^{-1} \nabla \vec{v} &= 0 \\
\frac{\partial^2 \rho'}{\partial t^2} - \nabla^2 p' &= 0 \\
\frac{p'}{c^2} &= \rho' \\
\nabla^2 p' - \frac{1}{c^2} \frac{\partial^2 p'}{\partial t^2} &= 0 \\
\nabla^2 \rho' - \frac{1}{c^2} \frac{\partial^2 \rho'}{\partial t^2} &= 0
\end{aligned} \tag{A.13}$$

Q.E.D.

B

Appendix B - Reflection Coefficient Derivation

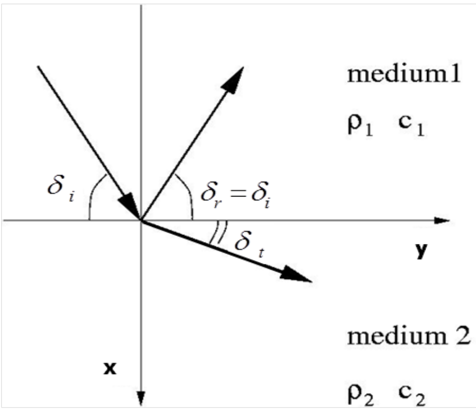

Figure B.1: Snell's Law[60]

The amplitudes A, C and B of the plane wave Equations 2.59 through 2.61 are unknown, but the laws of energy conservation stipulate that the total pressure difference on either side of the incidence plane must be equal.

$$p'_i + p'_r = p'_t \tag{B.1}$$

On this plane, as shown in Figure B.1, the value for x is zero. Additionally, all terms in Equation B.1 have the common value $e^{i\omega t}$. This means that Equations 2.59 through 2.61 can be inserted into Equation B.1, granting the following.

$$\begin{aligned}
Ae^{i\left(\cancel{\omega t - xsin(\delta_i)\omega/c_1} - ycos(\delta_i)\omega/c_1\right)} + Ce^{i\left(\cancel{\omega t + xsin(\delta_r)\omega/c_1} - ycos(\delta_r)\omega/c_1\right)} &= Be^{i\left(\cancel{\omega t - xsin(\delta_t)\omega/c_2} - ycos(\delta_t)\omega/c_2\right)} \\
Ae^{i\left(-ycos(\delta_i)\omega/c_1\right)} + Ce^{i\left(-ycos(\delta_r)\omega/c_1\right)} &= Be^{i\left(-ycos(\delta_t)\omega/c_2\right)} \\
(A+C)e^{i\left(-ycos(\delta_i)\omega/c_1\right)} &= Be^{i\left(-ycos(\delta_t)\omega/c_2\right)} \\
A+C &= Be^{i\left(y\omega(cos(\delta_i)/c_1 - cos(\delta_t)/c_2)\right)} \\
\text{According to Snell's law } cos(\delta_i)/c_1 - cos(\delta_t)/c_2 &= 0 \\
\text{Therefore } A+C &= B
\end{aligned} \tag{B.2}$$

To be able to use Equations 2.59 through 2.61, more relations between A, B and C are necessary. This can be obtained from the continuity relation between the normal components of particle velocity on the incidence plane, as shown in Equation B.3.

$$(v_x)_i + (v_x)_r = (v_x)_t \tag{B.3}$$

Euler's force equation, a representation for conservation of momentum as shown in Equation B.4 (also used inA.3), can be used to obtain a representation of v_x for Equation B.3.

$$v_x = -\frac{1}{\rho}\int \frac{\partial p'}{\partial x} dt \tag{B.4}$$

When inserting Equations 2.59 through 2.61 into Equation B.4, the following can be obtained.

$$\begin{aligned}
(v_x)_i &= -\frac{1}{\rho}\int \frac{\partial p_i'}{\partial x} dt \\
&= -\frac{1}{\rho}\int \frac{\partial A e^{i\left(\omega t - x sin(\delta_i)\omega/c_1 - y cos(\delta_i)\omega/c_1\right)}}{\partial x} dt \\
&= \frac{1}{\rho}\left(\frac{i \cdot A \cdot sin(\delta_i) \cdot \omega \cdot e^{i\left(\omega t - x sin(\delta_i)\omega/c_1 - y cos(\delta_i)\omega/c_1\right)}}{i \cdot \omega \cdot c_1}\right) \\
(v_x)_i &= \frac{1}{\rho_1}\left(\frac{A \cdot sin(\delta_i) \cdot e^{i\left(\omega t - x sin(\delta_i)\omega/c_1 - y cos(\delta_i)\omega/c_1\right)}}{c_1}\right) && \text{(B.5)} \\
(v_x)_r &= -\frac{1}{\rho_1}\left(\frac{C \cdot sin(\delta_r) \cdot e^{i\left(\omega t + x sin(\delta_r)\omega/c_1 - y cos(\delta_r)\omega/c_1\right)}}{c_1}\right) && \text{(B.6)} \\
(v_x)_t &= \frac{1}{\rho_2}\left(\frac{C \cdot sin(\delta_t) \cdot e^{i\left(\omega t + x sin(\delta_t)\omega/c_2 - y cos(\delta_t)\omega/c_1\right)}}{c_2}\right) && \text{(B.7)}
\end{aligned}$$

Using the same steps as used in Equation B.2, the following can be determined based on Equation B.3.

$$\begin{aligned}
\frac{1}{\rho_1}\left(\frac{(A-C)\cdot sin(\delta_i)}{c_1}\right)\cdot e^{i(-y cos(\delta_i)\omega/c_1)} &= \frac{1}{\rho_2}\frac{B \cdot sin(\delta_t)}{c_2}\cdot e^{i(-y cos(\delta_t)\omega/c_2)} \\
\frac{1}{\rho_1}\left(\frac{(A-C)\cdot sin(\delta_i)}{c_1}\right) &= \frac{1}{\rho_2}\frac{B \cdot sin(\delta_t)}{c_2}\cdot \cancel{e^{i(y cos(\delta_i)\omega/c_1 - y cos(\delta_t)\omega/c_2)}} \\
A - C &= B\frac{\rho_1 c_1 sin(\delta_t)}{\rho_2 c_2 sin(\delta_i)} && \text{(B.8)}
\end{aligned}$$

This final solution, combined with the result of Equation B.2, solves the system of equations necessary to model reflection and refraction on the boundary between two media. Further coefficients can be named to describe the transmission and reflection as a ratio of the incoming wave. These are given in Equation B.9 through B.12.

$$\begin{aligned}
Z_1 &= \frac{\rho_1 c_1}{sin(\delta_i)} && \text{(B.9)} \\
Z_2 &= \frac{\rho_2 c_2}{sin(\delta_t)} && \text{(B.10)} \\
R = \frac{C}{A} &= \frac{Z_2 - Z_1}{Z_2 + Z_1} && \text{(B.11)} \\
T = \frac{B}{A} &= \frac{2 Z_2}{Z_2 + Z_1} && \text{(B.12)}
\end{aligned}$$

C

Appendix C - Cross-spectral matrix

The derivation of the cross-spectral function treated in this appendix is based on a report by Sijtsma [57]. The cross-correlation function of the signals from two microphones, n and m, is defined as follows.

$$R_{mn}(t) = \lim_{T_0 \to \infty} \frac{1}{T_0} \int_{-T_0/2}^{T_0/2} \chi_m(\tilde{t}) \chi_n(\tilde{t} + t) d\tilde{t} \tag{C.1}$$

The cross-spectral density function is defined as the Fourier transform of the cross-correlation function, as given in Equation C.1.

$$\hat{G}_{mn}(f) = \int_{-\infty}^{\infty} R_{mn}(t) e^{-2\pi i f t} dt = \lim_{T_0 \to \infty} \frac{1}{T_0} \left(\int_{-T_0/2}^{T_0/2} \chi_m(t) e^{2\pi i f t} dt \right)^* \left(\int_{-T_0/2}^{T_0/2} \chi_n(t) e^{2\pi i f t} dt \right) \tag{C.2}$$

Sampling a signal over an infinite amount of time T is not possible, so the assumption is made that there is some periodicity in signal $\chi_n(t)$ with period T. This allows to express Equation C.2 as follows.

$$\hat{G}_{mn}(f) = \sum_{j=-\infty}^{\infty} \frac{1}{T} \int_0^T R_{mn}(t) e^{-2\pi i f t} dt \times \delta(f - j/T) \tag{C.3}$$

In Equation C.3, δ is the Dirac delta function. The following relation holds for $\hat{p}_n(f)$.

$$\hat{p}_n(f) = \frac{1}{T} \int_0^T \chi_n(t) e^{-2\pi i f t} dt \tag{C.4}$$

Using this, Equation C.1 can be rewritten, and placed into Equation C.3, as shown in Equation C.5

$$\hat{G}_{mn}(f) = \sum_{j=-\infty}^{\infty} \hat{p}_m^*(f) \hat{p}_n(f) \delta(f - j/T) \tag{C.5}$$

Since this is valid for both positive and negative frequencies, the single sided cross-correlation function is given in C.6

$$G_{mn}(f) = 2\hat{G}_{mn}(f), \text{ where } f > 0 \tag{C.6}$$

D

Appendix D - Calibrated noise source

The sound source system consists of a few components:

- The sound source
- An QAM power amplifier
- A surge protector
- A remote control

Figure D.1: Sound source

The sound source itself is an oblong shape with a total length of about 11 centimeters, and a diameter of about 2 centimeters. The sound emitting part of the source is located at the center of the object, and has a total length of 3 centimeters. The source features two M4 threaded mounting points at the top and bottom, allowing for simple and straightforward longitudinal fixing of the device. The sound source is connected to a surge protector by means of two wires.

The surge protector has the dual function of limiting the total power output of the amplifier to protect the source from overheating, as well as protecting the sound source from power spikes. It features a red LED on the rear, which will start to flicker when approaching unsafe power levels. If it burns a constant red, a safety cut-off kicks in and the power settings of the amplifier must be reduced to safe levels. The surge protector is connected to the amplifier by means of a 2 pole speakon cable.

Figure D.2: Surge Protector

Figure D.3: Amplifier

The amplifier allows the user to set the type of signal emitted, as well as the sound power level and the duration of the signal (20 seconds pulsating mode, or continuous). Out of the box, the amplifier can generate white and pink noise between 315 and 6300Hz, but also features a BNC socket for external input signals.

The source is calibrated in third octave bands, of which the power watt levels are given in Table D.1

Table D.1: Noise source calibration data - Third octave band analysis

Level indication on amplifier	40	40	40	40	40
Signal type	**pink L**	**pink A**	**pink E**	**white A**	**white E**
Frequency	**Pink Noise 2000-6300**	**Pink Noise 500-6300**	**Pink Noise 315-6300**	**White Noise 500-6300**	**White Noise 315-6300**
125 Hz	-	10.3	28.2	0.1	17.7
160 Hz	-	12.2	36.5	4.4	25.5
200 Hz	-1.2	24.2	48.9	17.5	41.8
250 Hz	0.9	39.9	57.3	34.9	51.7
315 Hz	-0.5	51.9	61.0	47.1	56.4
400 Hz	15.4	59.9	62.0	55.9	57.7
500 Hz	21.7	62.2	60.8	58.6	57.3
630 Hz	29.2	61.4	59.7	58.6	57.0
800 Hz	36.8	60.7	59.1	58.9	57.4
1 kHz	44.8	60.3	58.7	59.3	57.7
1.25 kHz	53.7	60.1	58.6	60.1	58.6
1.6 kHz	62.9	61.3	59.7	62.2	60.6
2 kHz	66.9	62.0	60.3	63.9	62.4
2.5 kHz	66.4	61.2	59.6	64.1	62.5
3.15 kHz	65.9	60.8	59.3	64.6	63.0
4 kHz	65.4	60.5	58.9	65.3	63.7
5 kHz	66.1	61.4	59.8	67.2	65.5
6.3 kHz	65.6	61.0	59.4	67.6	66.0
8 kHz	56.5	51.9	50.4	59.7	58.4
10 kHz	42.8	38.1	36.5	46.6	45.2
12.5 kHz	37.7	30.0	28.0	35.4	33.6
16 kHz	27.7	21.4	18.8	25.0	22.7

E

Appendix E - Optimized microphone distribution

Table E.1: Optimized configuration microphone coordinates [(0,0) defined at the center of the array]

#	X	Y	#	X	Y
1	0,2	0	33	-0,02	0
2	0,155	0,135	34	-0,095	0,165
3	0,035	0,195	35	-0,185	0,075
4	0,155	-0,135	36	-0,185	-0,075
5	0,32	-0,06	37	-0,095	-0,165
6	0,275	0,15	38	-0,275	0,165
7	0,11	0,3	39	-0,32	-0,045
8	0,365	0,255	40	-0,215	-0,24
9	-0,395	0,195	41	0,125	0,42
10	-0,425	-0,105	42	0,35	0,405
11	-0,53	0,105	43	0,02	0,54
12	-0,47	-0,255	44	0,245	0,585
13	-0,62	-0,09	45	0,53	0,555
14	-0,755	0,18	46	0,05	0,78
15	-0,695	-0,345	47	0,44	0,84
16	-0,95	-0,045	48	0,875	0,36
17	-0,26	-0,36	49	0,44	-0,045
18	-0,185	-0,495	50	0,53	0,09
19	-0,425	-0,465	51	0,455	-0,27
20	-0,035	-0,63	52	0,56	0,285
21	-0,305	-0,705	53	0,62	-0,135
22	-0,71	-0,645	54	0,65	-0,435
23	-0,125	-0,945	55	0,77	0,09
24	0,5	-0,81	56	0,905	-0,285
25	-0,11	0,3	57	0,035	-0,195
26	-0,185	0,405	58	-0,02	-0,33
27	-0,335	0,42	59	0,2	-0,255
28	-0,185	0,6	60	0,035	-0,435
29	-0,53	0,345	61	0,305	-0,315
30	-0,455	0,63	62	0,17	-0,51
31	-0,2	0,93	63	0,38	-0,495
32	-0,755	0,585	64	0,215	-0,75

F

Appendix F - Research sub-questions

The research objective for this thesis project was formulated as:

...To obtain a practical method of performing accurate sound measurements in the anechoic vertical wind tunnel at the Delft University of Technology by designing, creating, testing and evaluating a reconfigurable acoustic array using state-of-the-art techniques and equipment.

The leading research question to aid in achieving this objective was formulated as:

What design of an acoustic array for the anechoic vertical wind tunnel at the Delft University of Technology should be used to obtain optimal acoustic analysis results in terms of accuracy in level and location estimation of sound sources, spatial resolution and side- and grating lobe presence?

The research sub-questions were formulated as:

1. What is the best structural configuration in terms of practicality, flexibility and cost?
   (a) What are the structural requirements and restrictions imposed on the array, and how can these be fulfilled?
   (b) How can the (acoustic) performance of materials and structures be defined, quantified and determined?
   (c) How can practicality of the design be defined, quantified and determined?
   (d) How should reconfigurability of the array microphones be incorporated and implemented?
2. How should the array be created?
   (a) What possible techniques are available for manufacturing the array with the given choice of materials?
   (b) How can the array be transported, placed and stored in the wind tunnel?
   (c) How can the operation lifetime of the array be optimized?
3. How accurate is the array in determining the SPL and location of noise sources?
   (a) What microphone distribution(-s) should be used to test and evaluate array performance?
   (b) What soft- and hardware are necessary to be able to calibrate, test and evaluate array performance?
   (c) Which interfering phenomena are likely to occur with the given array structure, and how should these be modeled and diminished?
   (d) Within which range of test conditions is the accuracy of results deemed acceptable?

4. Which method(-s) of noise source identification should be applied to assess array performance?
   (a) Which methods of noise source identification exist and are available?
   (b) How should the level of applicability of a noise source identification method be defined, quantified and determined?
   (c) Which deconvolution methods exist and are usable?
   (d) How should the level applicability of a deconvolution method be defined, quantified and determined?
5. Which test setup(-s) and analysis methods should be used to assess array performance?
   (a) Which test conditions and source distributions can be encountered in wind tunnel testing?
   (b) Which result analysis methods should be used, and what is the expected performance of this method under the given test conditions?
   (c) How should array performance be defined, quantified and determined?

Bibliography

[1] Christopher S. Allen, William K. Blake, Robert P. Doughterty, Denis Lynch, Paul T. Soderman, and James R. Underbrink. *Aeroacoustic Measurements*. Springer-Verlag Berlin Heidelberg, 2002.

[2] Larry C. Andrews. *Special Functions of Mathematics for Engineers*. Oxford University Press, 1998.

[3] Mingsian R. Bai, Jeong-Guon Ih, and Jacob Benetsy. *Acoustic Array Systems - Theory, Implementation and Application*. John Wiley & Sons Singapore Pte. Ltd., 2013.

[4] V B Biesel and K A Cunefare. A test system for free-field qualification of anechoic chambers. *Sound and Vibration*, 57(5), 2003.

[5] M.A. Breazeale and O. Leroy. *Physical Acoustics*. Springer Science & Business Media, 2012.

[6] Thomas F. Brooks and William M. Humphreys. A deconvolution approach for the mapping of acoustic sources (DAMAS) determined from phased microphone arrays. *Journal of Sound and Vibration*, 294(4), 2006.

[7] Brüel&Kjaer. Acoustical arrays. `https://www.bksv.com/en/products/transducers/acoustic/acoustical-arrays`, Year Unknown, accessed 22-02-2017.

[8] S Buck, J Roadman, P Moriarty, and S Palo. Acoustic array development for wind turbine noise characterization. Technical report, National Renewable Energy Laboratory, 2013.

[9] Kuo-Tsai Chen. Study on the acoustic transmission loss of a rigid perforated screen. *Applied Acoustics*, 47(4), 1996.

[10] Taehwan Cho, Cheolwan Kim, and Duckjoo Lee. Acoustic measurement for 12turbine by using beamforming. *Current Applied Physics*, 2010.

[11] Zhigang Chu and Yang Yang. Comparison of deconvolution methods for the visualization of acoustic sources based on cross-spectral imaging function beamforming. *Mechanical Systems and Signal Processing*, 48, 2014.

[12] Robert P Doughterty. Functional Beamforming. In *5th Berlin Beamforming Conference*, 2014.

[13] Robert P Doughterty. Functional Beamforming for Aeroacoustic Source Distributions. In *20th AIAA/CEAS Aeroacoustics Conference*, 2014.

[14] Jeoffrey Fischer, Con Doolan, and Branko Zajamsek. Aeroacoustic beamforming of a model wind-turbine in anechoic and reverberant environments. In *Proceedings of ACOUSTICS 2016*, 2016.

[15] V.A. Fok. Theoretical study of the conductance of a circular hole, in a partition across a tube. *Doklady Akademii Nauk SSSR*, 31(9), 1941.

[16] International Organization for Standardization. Acoustics - measurement of room acoustic parameters. ISO 3382:2012, Reviewed 2017.

[17] International Organization for Standardization. Acoustics — determination of sound power levels and sound energy levels of noise sources using sound pressure — precision methods for anechoic rooms and hemi-anechoic rooms. ISO 3745:2012, Reviewed 2017.

[18] gfai tech. Microphone arrays. `https://www.acoustic-camera.com/en/products/microphone-arrays.html`, Year Unknown, accessed 22-02-2017.

[19] Kevin Bernard Ginn and Karim Haddad. Noise source identification techniques: simple to advanced applications. In *Proceedings of the Acoustics 2012 Nantes Conference*, 2012.

[20] G.R.A.S. http://www.gras.dk/40ph.html, 2017.

[21] G.R.A.S. http://www.gras.dk/42aa.html, 2017.

[22] Donald E. Hall. *Musical Acoustics.* Brooks/Cole Publishing, 2 edition, 1991.

[23] Xun Huang, Long Bai, Igor Vinogradov, and Edward Peers. Adaptive beamforming for array signal processing in aeroacoustic measurements. *The Journal of the Acoustical Society of America*, 131(3), 2012.

[24] National Instruments. Trigger ai acquisition. LabVIEW Core 1 course, 2017.

[25] National Instruments. The ni tdms file format. http://www.ni.com/white-paper/3727/en/, 2017.

[26] International Air Transport Association. *Demand for Air Travel in 2015 Surges to Strongest Result in Five Years*. http://www.iata.org/pressroom/pr/Pages/2016-02-04-01.aspx, 2016, accessed 02-12-2016.

[27] Baron Rayleigh John William Strutt. *The Theory of Sound.* Macmillan, 1877.

[28] Paul M. Kendig and Roland E. Mueser. A simplified method for determining transducer directivity index. *The Journal of the Acoustical Society of America*, 19(691), 1947.

[29] V Kopiev, V Palchikovskiy, BY Bersenev, S Makashov, I Belyaev, I Korin, E Sorokin, I Khramtsov, and O Kustov. Design and quantification of an anechoic facility in pnrpu. *Procedia Engineering*, 176, 2017.

[30] Jeroen Lanslots, Filip Deblauwe, and Karl Janssens. Selecting Sound Source Localization Techniques for Industrial Applications. *Sound and Vibration*, 44(6), 2010.

[31] Andreas Lauterbach, Klaus Ehrenfried, Lars Koop, and Sigfried Loose. Procedure for the accurate phase calibration of a microphone array. In *15th AIAA/CEAS Aeroacoustics Conference*, 2009.

[32] Salil Luesutthiviboon. Design of an optimized acoustic array for aero-acoustic research in an open-jet anechoic wind tunnel. Master's thesis, Delft University of Technology, 2017.

[33] Anwar Malgoezar, Mirjam Snellen, Pieter Sijtsma, and Dick Simons. Improving beamforming by optimization of acoustic array microphone positions. In *5th Berlin Beamforming Conference*, 2016.

[34] N.W. McLachlan. *Bessel Functions for Engineers.* Oxford University Press, 1955.

[35] Merford. Flamex basic. Technical report, Merford Acoustic Materials, 2017.

[36] Roberto Merino-Martinez, Pieter Sijtsma, Mirjam Snellen, T. Ahlefeldt, J. Antoni, C.J. Bahr, D. Blacodon, D. Ernst, A. Finez, S. Funke, T.F. Geyer, S. Haxter, G. Herold, X. Huang, W.M. Humphreys, Q. Leclere, A. Malgoezar, U. Michel, T. Padois, A. Pereira, C. Picard, E. Sarradj, H. Siller, D.G. Simons, and C. Spehr. A review of acoustic imaging methods using phased microphone arrays. *CEAS Aeronautical Journal*, 2017.

[37] P Migliore and S Oerlemans. Wind tunnel aeroacoustic tests of six airfoils for use on small wind turbines. Technical report, National Renewable Energy Laboratory, 2003.

[38] C.T. Molloy. Calculation of the directivity index for various types of radiators. *The Journal of the Acoustical Society of America*, 20, 1948.

[39] National Instruments. Pxie-1085. http://www.ni.com/nl-nl/support/model.pxie-1085.html, 2017.

[40] National Instruments. Pxie-4499. http://www.ni.com/nl-nl/support/model.pxie-4499.html, 2017.

[41] National Instruments. Rmc-8354. http://www.ni.com/nl-nl/support/model.rmc-8354.html, 2017.

[42] National Instruments. Pxie-8370. http://www.ni.com/nl-nl/support/model.pxie-8370.html, 2017.

[43] National Instruments. Shb4x-8bnc. `http://sine.ni.com/nips/cds/view/p/lang/nl/nid/204002`, 2017.

[44] Oceanz. Oceanz - 3d printing professional. `http://oceanz.eu/`, 2017.

[45] Vincent Phong and Dimitri Papamoschou. Acoustic transmission loss of perforated plates. In *18th AIAA/CEAS Aeroacoustics Conference*, 2012.

[46] Vincent Phong and Dimitri Papamoschou. High frequency acoustic transmission loss of perforated plates at normal incidence. *Journal of the Acoustical Society of America*, 134(2), 2013.

[47] Zebb Prime and Con Doolan. A comparison of popular beamforming arrays. In *Acoustics 2013 - Victor Harbor*, 2013.

[48] Qsources. Qsources bvba. `https://www.qsources.be/`, 2017.

[49] R. Nave. Inverse Square Law, General, Year Unknown, accessed 20-02-2017.

[50] S.W. Rienstra and A. Hirschberg. An introduction to acoustics. Eindhoven University of Technology, 2017.

[51] Simao S. Rodrigues and Andre C. Marta. On adressing noise constraints in the design of wind turbine blades. *Structural and Multidisciplinary Optimization*, 50(3), 2014.

[52] Alejandro Rubio Carpio, Roberto Merino-Martinez, Francesco Avallone, Daniele Ragni, Mirjam Snellen, and Sybrand van der Zwaag. Broadband trailing edge noise reduction using permeable metal foams. In *Internoise 2017*, 2017.

[53] Ennes Sarradj. Three-dimensional acoustic source mapping with different beamforming steering vector formulations. *Advances in Acoustics and Vibration*, 2012, 2012.

[54] Ennes Sarradj. A generic approach to synthesize optimal array microphone arrangements. In *6th Berlin Beamforming Conference*, 2016.

[55] Ennes Sarradj, Gert Herold, Pieter Sijtsma, Roberto Merino-Martinez, Anwar Malgoezar, Mirjam Snellen, Thomas F. Geyer, Christopher J. Bahr, Ric Porteous, Danielle J. Moreau, and Con J. Doolan. A microphone array method benchmarking exercise using synthesized input data. In *23rd AIAA/CEAS Aeroacoustics Conference*, 2017.

[56] Theodore J. Schultz. *Acoustical uses for perforated metals - Principles and Applications*. Industrial Perforators Association, Inc, 1986.

[57] P. Sijtsma. Acoustic beamforming for the ranking of aircraft noise. Technical report, NLR, 2012.

[58] Pieter Sijtsma. CLEAN based on spatial source coherence. In *AIAA/CEAS Aeroacoustics Conference*, 2007.

[59] Pieter Sijtsma, Roberto Merino-Martinez, Anwar M. N. Malgoezar, and Mirjam Snellen. High-resolution clean-sc:theory and experimental validation. *International Journal of Aeroacoustics*, 16, 2017.

[60] Dick Simons. *Introduction to Aircraft Noise*. Course at Delft University of Technology, 2015-2016.

[61] Allan O Steinhardt and Barry D Van Veen. Adaptive Beamforming. *International journal of adaptive control and signal processing*, 3, 1989.

[62] Li Tan. *Digital Signal Processing - Fundamentals and Applications*. Elsevier, 2008.

[63] Sart Tilman. Sound power level characterization of a miniature sound source type qindw. Technical report, University of Liege, 2017.

[64] P.J.G. van der Linden. User instruction miniature sound source, type qindw. Technical report, INFRA-QSOURCES, 2017.

[65] Michael Vorländer. *Auralization - Fundamentals of Acoustics, Modelling, Simulation, Algorithms and Acoustic Virtual Reality*. Springer Berlin Heidelberg, 2008.

Notes and To-Do's